Sensorless control of a PMSM with parameters uncertainties

Marcello D'Alessio
MCE4-1021

BREAKING NEW GROUND
AALBORG UNIVERSITY

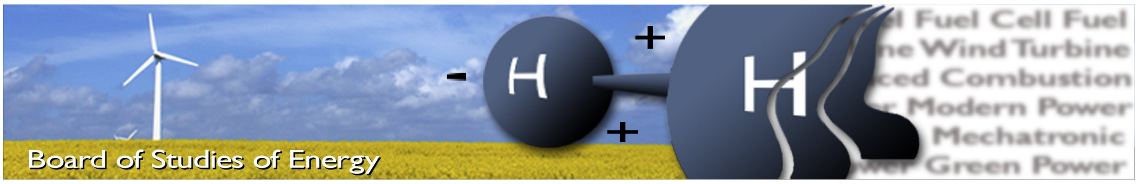

Title:	Sensorless control of PMSM with parameters uncertainties
Semester:	10th
Semester theme:	Master Thesis
Project period:	05.01.16 to 05.04.16
ECTS:	30
Supervisor:	Michael Bech Møller
Project group:	MCE04-1021

Marcello D'Alessio

Copies:	3
Pages, total:	79
Appendices:	2
Supplements:	1 CD-ROM

ABSTRACT:

This thesis studies the class of sensorless control methods for a Permanent Magnet Synchronous Machine (PMSM) which are based on the estimation of the back-EMF components using the fundamental frequency model. The problem is approached from a theoretical point of view, so first the models of the elements in a generic PMSM drive system are outlined together with the problem statement. Field Oriented Control for a PMSM is then introduced along with the motivation for sensorless control. The principle of back-EMF based sensorless control estimation is described. Matsui Second method and an extension of this proposed by Nahid-Mobarakeh are described and evaluated analytically and numerically. Considerations are made on the effects of parameters uncertainties on the proposed algorithm. A model based online parameter estimation technique is described and evaluated through simulations. The sensorless algorithm is implemented on a test platform and evaluated experimentally.

By signing this document, each member of the group confirms that all group members have participated in the project work, and thereby all members are collectively liable for the contents of the report. Furthermore, all group members confirm that the report does not include plagiarism.

Preface

This thesis has been written at Aalborg University, in the autumn of 2015 by the undersigned, Marcello D'Alessio, 10th semester student group MCE04-1021. The experimental activity reported has been conducted at the Flexible Drive System Laboratory of the Energy Technology Department at Aalborg University.

I would like to thank my supervisor Michael who supported and encouraged me beyond the context of this thesis. I would like to thank Hernan and Lucian from Danfoss Drives for their suggestions which gave me a further insight in what it means to be a professional in this field.

The references in the report are shown in Harvard referencing style. The references are marked with the last name of the author, as well as the year of publication, enclosed by squared brackets [ ]. The bibliography is found at the back of the report and is sorted alphabetically by author name. References to the origin of figures are stated in the figure caption.

In the equations vectors are notated in bold, while scalars and Units have regular typeset.

Figures, equations and tables are referenced to with two numbers. The first number indicates the chapter and the second indicates the number of the equation, figure or table.

The following software is used in the project:

- LaTeX - for report writing
- MATLAB - for data processing and calculation of numerical solutions to non-linear equations
- pplane8 MATLAB script - for graphical representation of non linear systems trajectories on the phase plane
- MATLAB Simulink - for simulations of dynamic models and implementation on dSPACE environment
- PLECS and PLECS Simulink toolbox - for simulations of power electronics
- dSPACE Controldesk - for the management and control of the experiments

Enclosed in the back of the report there is a CD containing the developed Simulink/PLECS models, Controldesk applications, experimental data, selection of used sources, and a PDF copy of this thesis.

“Aequam memento servare mentem”

Nomenclature

α, β, b	Sensorless estimator parameters
$\bar{\psi}_{\mathrm{pm}}$	Ratio between the rotor flux linkage used in the estimator and the actual one
δ	Torque angle
η	Stator Resistance estimation gain
$\frac{d}{dt}$	Differential operator or Heaviside operator
$\hat{\omega}_{\mathrm{b}}$	Auxiliary speed for estimation
$\hat{\omega}_{\mathrm{rf}}$	Digitally filtered estimated speed used in the speed control loop
$\hat{\omega}_{\mathrm{r}}$	Speed of the estimated reference frame
$\hat{\theta}_{\mathrm{r}}$	Estimated rotor position
$\hat{R}_{\mathrm{se}}$	Estimated Stator Resistance
$\hat{R}_{\mathrm{s}}$	Constant Stator Resistance parameter used in the estimator
$\hat{}$	Estimated quantities or parameters used in the estimator
$\mathbf{i}_{\mathrm{abc}}$	Machine's line currents
$\mathbf{v}_{\mathrm{abc}}$	Machine's line-to-neutral voltages
$\mathbf{v}_{\mathrm{s}}$	Stator space vector
ψ_{pm}	Rotor's permanent flux linkage
τ	Digital Filter time constant
θ_{m}	Mechanical Rotor position
θ_{r}	Electrical Rotor position
$\tilde{\theta}_{\mathrm{r}}$	Rotor position Error
$\tilde{}$	Error quantities or differences between the parameters used in the estimator and the actual ones
ζ	Variable structure estimation law parameter
d	Duty cycle
$e_{\mathrm{d}}, e_{\mathrm{q}}$	Back-EMF components in the rotor ref. frame
e_{α}, e_{β}	Back-EMF components in the stationary ref. frame
e_{δ}, e_{γ}	Back-EMF components in the estimated ref. frame
f_{v}	Viscous friction coefficient

J_{m} Motor-Load joint moment of inertia

K_{a} Anti wind-up coefficient of PI controller

K_{dq} Park transformation matrix

K_{i} Integral coefficient of PI controller

K_{p} Proportional coefficient of PI controller

K_{T} Torque Constant

$K_{\alpha\beta}$ Clarke transformation matrix

k_{α}, k_{β} Estimator coefficients

L_{d} d-axis inductance

L_{q} q-axis inductance

L_{s} Field Inductance

p Number of pole pairs

R_{s} Stator Resistance

s Laplace transform variable

S_{j} Switch state for gate j-th in the VSI

t_{AD} Time taken by the microcontroller for the Analog to Digital conversion

t_{d} Dead time in the VSI

T_{e} Electromagnetic torque

t_{f} Turn Off time of the IGBT device in the VSI

T_{L} Load torque

t_{r} Turn On time of the IGBT device in the VSI

T_{s} Sampling Time

t_{VC} Time taken by the microcontroller for executing the control task

$v_{\mathrm{aN}}, v_{\mathrm{bN}}, v_{\mathrm{cN}}$ VSI Leg voltages

V_{dc} DC Link Voltage

V_{d} Forward voltage of the free-wheeling diode in the VSI

V_{igbt} Forward voltage of the IGBT device in the VSI

x_{e} Equilibrium state

z Zeta transform variable

* Reference value

List of abbreviations and acronyms

AC Alternated Current

A/D Analog/Digital

Back-EMF Back-ElectroMotive Force

DC Direct Current

EKF Extended Kalman Filter

FOC Field Oriented Control

IGBT Insulated-Gate Bipolar Transistor

IM Induction Machine

IPMSM Interior magnets Permanent Magnet Synchronous Machine

MRAS Model Reference Adaptive System

PI Proportional Integral controller

PLL Phase Locked Loop

PMSM Permanent Magnet Synchronous Machine

PWM Pulse Width Modulation

RLS Recursive Least Square

SPMSM Surface mounted Permanent Magnet Synchronous Machine

SVM Space Vector Modulation

VSI Voltage Source Inverter

ZOH Zero Order Holder

Contents

Introduction 1

1.1 Background

The evolution of AC electrical motor drives has been always conditioned by the application and the design of the several types of AC electrical machines. Drive systems have seen through the years a continuous evolution of methods and techniques in order to achieve same or better performances, by using more economically convenient or robust types of machines [Sen et al., 1996]. Permanent Magnet Synchronous Machines have seen a growing interest by researchers and industry due to their high power density and efficiency. The decreasing trend in permanent magnets prices, enhanced the range of application for this kind of motor. A significant path of research and development for motor drive systems has always been the purpose of sparing mechanical sensors for torque, speed and position. Indeed many of the high performance control methods such as field oriented drive schemes, required originally mechanical sensors for measuring the speed and the position of the machine's rotor. In most cases these sensors revealed themselves to be relatively expensive and subject to additional costs with regards to maintenance and operational robustness. [University of Newcastle, 2014] is an example of cost analysis of the integration of drive systems which can avoid the use of mechanical sensors for a specific application. In the examined case the original investment is amortised in less than three years.

The evolution of power electronic components, micro-controllers and electrical sensors made it possible to devise control schemes which could avoid the use of mechanical sensors. This class of drives is nowadays commonly referred as "speed and position sensorless drives" or more simply *sensorless drives*, meaning that there are no physical sensors for rotor speed and/or position. Several basic open-loop control schemes (such as V/f control), are normally not included in this definition, since it is intended that this class of drives features closed-loop control schemes, with the difference that the output feedback is not provided by a physical sensor, but rather by a flux/speed observer. The information provided by a mechanical sensor is substituted by an estimation performed on the basis of the sensed currents and voltages. In the most settings only the DC Link voltage is sensed and the voltage signal is obtained from the control signal, output of the current controller.

1.2 PMSM sensorless control problem

A common classification for sensorless speed estimation techniques is the one depicted in Fig. 1.1. Two examples for each category are mentioned in the figure.

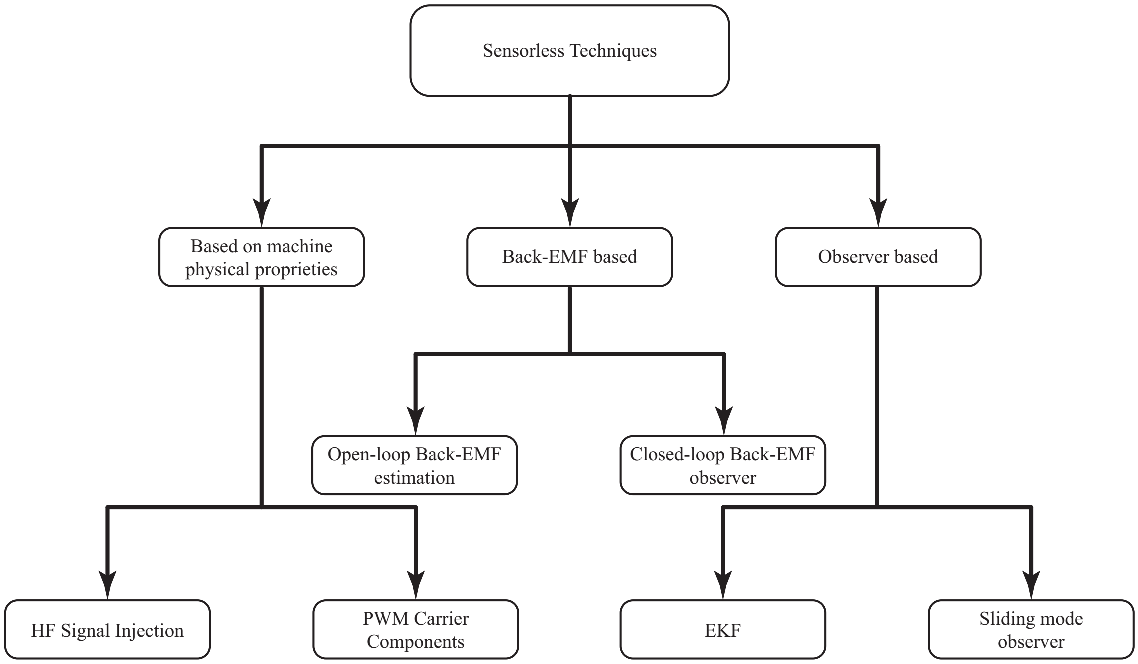

Figure 1.1: Classification of sensorless rotor position estimation techniques

The three main categories are classified by the different approach used for estimating the rotor position and speed:

- The signal injection methods harvest the physical configuration of the machine, and has the substantial advantage of being the most reliable at very low speeds and stand-still.
- The back-emf methods estimate the speed from the back-emf components that are calculated from the machine's electrical variables. They have broad application in the medium-high speed range due to their simplicity.
- The state observer methods are based on the machine seen as a nonlinear state-space system and its observability. Non linear observers such as the Extended Kalman Filter (EKF) or the Sliding mode observer belong to this category. They have shown good performances but also few drawbacks such as relevant calculation times and complexity of the initial tuning.

Concerning the Back-EMF based methods, there are several ways for calculating machine flux components and thus estimating rotor flux's speed and position. Commonly there is a distinction between "open-loop" and "closed-loop" flux estimators in AC machines. Both kinds feature a calculation of flux components from integration of machine's model equations, the "closed-loop" kind includes a feedback correction control resembling the classical appearance of a model based *observer*, while the "open-loop" type is simply a real-time simulation based on the machine's model [Vas, 1998].

In [Jansen and Lorenz, 1994] the accuracy due to parameters uncertainty is discussed for different kinds of flux observers for induction machines. The analysis of several observer schemes concludes that in the range of operation from zero to rated speed, the presented observers are most sensitive to stator resistance. Similar conclusions are drawn for synchronous AC machines flux estimators in [Nahid-Mobarakeh et al., 2001]. For PMSMs the stator resistance is the parameter most subject to variation in all the operating range due to its dependency on the temperature [Underwood, 2006]. The magnetization of the permanent magnet is subjected to variations sensibly in the high speed range, this might affect the high speed performances also for sensored drive systems [Krishnan, 2010]. This leads to an ongoing research in the field of online parameters identification and estimation/adaptation techniques for sensorless PMSM drives.

1.3 Literature Review

Parameters identification and online estimation in AC machines is a well known topic of research utilizing standard systems identification tools. For the reasons discussed in the previous section, one of the prominent motivations for online parameter estimation is the application in position estimators for sensorless operation.

Most of the examples found in the literature for online parameter estimation in PMSMs with standard identification tools make use of speed feedback information from a physical sensor [Underwood and Husain, 2010] [Basar et al., 2014], so that the estimation can relay on more accurate regression models for recursive estimations. In [Abjadi et al., 2005] a Sensorless control law combining a Sliding mode observer and an RLS estimation for parameters, is proposed, its closed-loop stability is proven analytically and its performances are evaluated through simulations.

Another approach to the problem is to augment a position/speed observer with additional states for the parameters in the hypothesis that these vary slowly with regard to the machine's electrical subsystem. This approach is seen for a number of position/speed nonlinear observers such as EKF or Kalman-like filters [Glumineau and de Leon Morales, 2015]. The state addition increases the complexity further of tuning the initial covariance matrices for ensuring the convergence of the observer. A solution in between has been proposed in [Hinkkanen et al., 2012] and [Nahid-Mobarakeh et al., 2004]. A stator resistance observer is integrated in a Back-EMF based position estimation method, so that low speed operation can be improved while still keeping the position estimator relatively simple in terms of tuning and computational burden. In both the reported solutions, the stability of the augmented observer is proven analytically and in [Hinkkanen et al., 2012] is validated experimentally at speeds as low as 45 rpm.

1.4 Objective

The objective of the thesis is to design and implement a back-EMF model-based sensorless position estimator for PMSM which could estimate changes in the stator resistance, in order to improve performances in the lower speeds range. The purpose is to find a method which could constitute a good compromise between the desire of having an online estimation of a relevant machine parameter and the requirement of running in sensorless operation. The performances of the algorithm are evaluated in a Field Oriented Control (FOC) scheme with PI controllers for the axes currents and speed control. The objective implies the overcoming of typical problems for this kind of drives such as compensation of inverter non-linearities and system delays.

1.5 Problem Statement

The preliminary discussion and the objective definition lead to the following problem statement:

How is a back-EMF model based mechanical sensorless drive system for PMSMs devised and implemented, how its performances depend on the variation of machine's parameters and how can it be made robust towards changes in the stator resistance through an online estimation tool?

1.6 Thesis Outline

The electrical and mechanical dynamical models of a generic PMSM system are introduced, together with the model of a Voltage Source Inverter and the description of the modulation strategy in chap. 2. In chap. 3 the principle of Field Oriented Control is introduced along with motivation for Sensorless position estimation. The design and the tuning of current and speed control loops is described and evaluated. In chap. 4 the back-EMF model-based estimation principle is presented. The sensorless algorithm is presented and evaluated through simulations. In chap. 5 the robustness and the effects of parameters uncertainties is analysed and discussed, then the concept of the model based online estimation of parameters is presented and evaluated through simulations. In chap. 6 a compensation technique for the Voltage Source Inverter non linearities is presented in order to improve performances of the sensorless algorithm. In chap. 7, the experimental setup is described and the experimental results are presented. Finally conclusions on the whole project are drawn, together with possible directions and suggestions for future works.

1.7 Limitations and assumptions

The following assumptions are made for the simulation models.

For what concerns the **PMSM Model** the following simplifying assumption are taken into account:

- The PMSM is supposed to be a balanced three-phase system. So the voltages applied to the machine are balanced.
- The losses in the rotor core due to parasite conduction currents are neglected.
- In the derivation of the simulation model the Stator Resistance is supposed to be constant and isotropic, this assumption is lifted for the Resistance in the two axes model and simulation are performed for changing values of resistance, in order to test the online estimation algorithm.
- Magnetic saturation effects are neglected.
- All the electrical variables' harmonics of higher order than the fundamental frequency are neglected and the machine has sinusoidal back-EMF waveform.

For what concerns the **Voltage Source Inverter**:

- The switching frequency is 5kHz.
- The dead-time used in simulation is $2.5\mu s$
- The inverter is controlled through single update control iterations. This means that the frequency of the current sampling and of the control sequence is the same of the PWM.

Modelling of the PMSM drive system 2

2.1 PMSM model

The modelled Permanent Magnet Synchronous Machine is assumed to be a symmetrical three-phase system. The assumption makes it possible to describe the behaviour of the machine by means of a two-axes system through the Clark and Park transformations [Krause et al., 2013]. The concentration of the stator windings characterizes the back-emf waveform of the machine [Underwood, 2006]. In the following, the machine taken into account for the modelling has sinusoidal waveform back-emf.

Depending on the machine's rotor configuration there exist several kinds of PMSMs. The most common are the Surface mounted (SPMSM) and Interior magnets (IPMSM) machines as shown in Fig. 2.1.

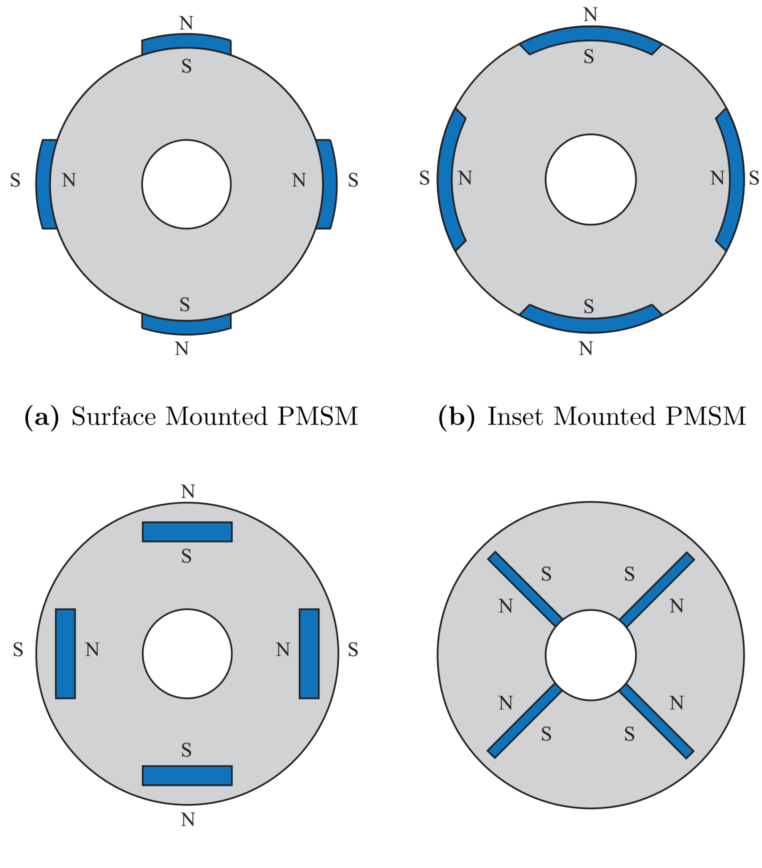

(a) Surface Mounted PMSM (b) Inset Mounted PMSM

(c) Interior Mounted PMSM (d) Flux Concentrating

Figure 2.1: Different typologies of PMSM [Glumineau and de Leon Morales, 2015]

The disposition of magnets in the rotor affects the shape of the air-gap which in turn defines the saliency of the machine. The common approach for control design for AC machines is to derive a rotating reference frame dynamical model from the stationary three phase windings equations. The implementation of the dynamical model in the rotational reference frame is easier and allows to see the machine's variables as DC quantities.

The three-phase PMSM system circuit reduced to one pole pair is represented in Fig. 2.2, together with the reference frame axes representation that will be now introduced. The three-phase PMSM system equations are

$$\mathbf{v}_{\mathrm{abc}} = R_{\mathrm{s}}\mathbf{i}_{\mathrm{abc}} + \frac{d\boldsymbol{\psi}_{\mathrm{abc}}}{dt} \tag{2.1}$$

$$\boldsymbol{\psi}_{\mathrm{abc}} = \mathbf{L}_{\mathrm{s}}\mathbf{i}_{\mathrm{abc}} + \boldsymbol{\psi}_{\mathrm{pmabc}} \tag{2.2}$$

$$\boldsymbol{\psi}_{\mathrm{pmabc}} = \begin{bmatrix} \psi_{\mathrm{pm}}\cos(\theta_{\mathrm{r}}) \\ \psi_{\mathrm{pm}}\cos(\theta_{\mathrm{r}} - 2\pi/3) \\ \psi_{\mathrm{pm}}\cos(\theta_{\mathrm{r}} + 2\pi/3) \end{bmatrix} \tag{2.3}$$

Where θ_{r} is the electrical rotor position defined as $p\theta_{\mathrm{m}}$, in which θ_{m} is the mechanical rotor angle and p is number of machine's pole pairs. $\mathbf{v}_{\mathrm{abc}}$ and $\mathbf{i}_{\mathrm{abc}}$ are machine's line to neutral voltages and line currents respectively, ψ_{pm} is rotor's permanent magnet flux linkage. The inductance matrix $\mathbf{L}_{\mathrm{s}}$ is the combination of the constant self and mutual phases inductances matrix, and an inductance which depends on the rotor position [Krause et al., 2013]. Putting the equations together and expanding the inductance matrix yields

$$\mathbf{v}_{\mathrm{abc}} = R_{\mathrm{s}}\mathbf{i}_{\mathrm{abc}} + \frac{d}{dt}(\mathbf{L}_{\mathrm{s}}\mathbf{i}_{\mathrm{abc}} + \boldsymbol{\psi}_{\mathrm{pmabc}}) \tag{2.4}$$

$$\mathbf{L}_{\mathrm{s}} = \mathbf{L}_{\mathrm{sm}} + \mathbf{L}_{\mathrm{sr}} \tag{2.5}$$

$$\mathbf{L}_{\mathrm{sm}} = \begin{bmatrix} L_{\mathrm{aa}} & M_{\mathrm{ab}} & M_{\mathrm{ac}} \\ M_{\mathrm{ba}} & L_{\mathrm{bb}} & M_{\mathrm{bc}} \\ M_{\mathrm{ca}} & M_{\mathrm{cb}} & L_{\mathrm{cc}} \end{bmatrix} \tag{2.6}$$

$$\mathbf{L}_{\mathrm{sr}} = L_{\mathrm{sr}} \begin{bmatrix} \cos(2\theta_{\mathrm{r}}) & \cos(2\theta_{\mathrm{r}} - 2\pi/3) & \cos(2\theta_{\mathrm{r}} + 2\pi/3) \\ \cos(2\theta_{\mathrm{r}} - 2\pi/3) & \cos(2\theta_{\mathrm{r}} + 2\pi/3) & \cos(2\theta_{\mathrm{r}}) \\ \cos(2\theta_{\mathrm{r}} + 2\pi/3) & \cos(2\theta_{\mathrm{r}}) & \cos(2\theta_{\mathrm{r}} - 2\pi/3) \end{bmatrix} \tag{2.7}$$

By using the hypothesis that the motor is a balanced three phase system, it is possible to transform the three phase model in a stationary two-phase machine model through the Clarke reference frame transformation Eq. 2.8. Both sides of the equation are multiplied by the Clarke transformation, the inductances matrix is also transformed in the stationary reference frame. The transformations yields the following stationary 2 phase machine model:

$$K_{\alpha\beta} = \frac{2}{3}\begin{bmatrix} 1 & -\frac{1}{2} & -\frac{1}{2} \\ 0 & \frac{\sqrt{3}}{2} & -\frac{\sqrt{3}}{2} \end{bmatrix} \tag{2.8}$$

$$\mathbf{v}_{\alpha\beta} = R_{\mathrm{s}}\mathbf{i}_{\alpha\beta} + \frac{d\mathbf{L}_{\mathrm{s}\alpha\beta}}{dt}\mathbf{i}_{\alpha\beta} + \mathbf{L}_{\mathrm{s}\alpha\beta}\frac{d\mathbf{i}_{\alpha\beta}}{dt} + \frac{d\boldsymbol{\psi}_{\mathrm{pm}\alpha\beta}}{dt} \tag{2.9}$$

$$\mathbf{L}_{\mathrm{s}\alpha\beta} = K_{\alpha\beta}\mathbf{L}_{\mathrm{s}}K_{\alpha\beta}^{-1} \tag{2.10}$$

The model's inductances are expressed in Eq. 2.11 as function of the equivalent axis inductances (L_{d} and L_{q}) which in turn depends on the geometry of the machine's rotor. The calculation of the impedances matrices suggests an important consequence of the saliency of the machine. The smallest is the difference between the two axes' inductances, the least the model's inductance depends on the rotor position. In the ideal case of a completely non-salient SPMSM, the machine inductances are equal, the inductance term dependent on the rotor position is cancelled out.

$$\begin{bmatrix} v_\alpha \\ v_\beta \end{bmatrix} = \begin{bmatrix} R_\mathrm{s} + \frac{d}{dt}(L_\mathrm{A} + L_\mathrm{B}\cos(2\theta_\mathrm{r})) & \frac{d}{dt}L_\mathrm{B}\sin(2\theta_\mathrm{r}) \\ \frac{d}{dt}L_\mathrm{B}\sin(2\theta_\mathrm{r}) & R_\mathrm{s} + \frac{d}{dt}(L_\mathrm{A} - L_\mathrm{B}\cos(2\theta_\mathrm{r})) \end{bmatrix} \begin{bmatrix} i_\alpha \\ i_\beta \end{bmatrix} + \omega_\mathrm{r}\psi_\mathrm{pm} \begin{bmatrix} -\sin\theta_\mathrm{r} \\ \cos\theta_\mathrm{r} \end{bmatrix}$$
$$L_\mathrm{A} = \frac{L_\mathrm{d} + L_\mathrm{q}}{2} \quad L_\mathrm{B} = \frac{L_\mathrm{d} - L_\mathrm{q}}{2} \tag{2.11}$$

The model of the PMSM in the rotating reference frame is in turn obtained by multiplying the differential equations by the Stationary to Rotational Reference Frame transformation Eq. 2.12, also known as Park transformation.

$$K_\mathrm{dq} = \begin{bmatrix} \cos\theta_\mathrm{r} & \sin\theta_\mathrm{r} \\ -\sin\theta_\mathrm{r} & \cos\theta_\mathrm{r} \end{bmatrix} \tag{2.12}$$

The direct axis of the reference frame is aligned to the rotor (permanent magnet) flux position θ_r. The model's inductance do not depend any more on the rotor position.

$$\mathbf{v}_\mathrm{dqs} = R_\mathrm{s}\mathbf{i}_\mathrm{dqs} + \mathbf{J}\omega_\mathrm{r}\boldsymbol{\psi}_\mathrm{dqs} + \frac{d\boldsymbol{\psi}_\mathrm{dqs}}{dt} \tag{2.13}$$
$$\boldsymbol{\psi}_\mathrm{dqs} = \mathbf{L}_\mathrm{s}\mathbf{i}_\mathrm{dqs} + \boldsymbol{\psi}_\mathrm{pm} \tag{2.14}$$
$$\boldsymbol{\psi}_\mathrm{pm} = \begin{bmatrix} \psi_\mathrm{pm} \\ 0 \end{bmatrix} \qquad \mathbf{L}_\mathrm{s} = \begin{bmatrix} L_\mathrm{d} & 0 \\ 0 & L_\mathrm{q} \end{bmatrix} \qquad \mathbf{J} = \begin{bmatrix} 0 & 1 \\ -1 & 0 \end{bmatrix} \tag{2.15}$$

Given these assumptions and premises, the motor model applies for both salient and non-salient PMSMs, with the difference that in the rotor reference frame the resulting axes inductances will be equal for the non salient SPMSM $L_\mathrm{d} = L_\mathrm{q}$ and different for the salient IPMSM $L_\mathrm{d} \neq L_\mathrm{q}$. By substituting Eq. 2.14 into 2.13, and expanding the equation in the two axes, Eq. 2.16 - 2.17 are yielded

$$v_\mathrm{ds} = R_\mathrm{s}i_\mathrm{ds} + L_\mathrm{d}\frac{di_\mathrm{ds}}{dt} - \omega_\mathrm{r}L_\mathrm{q}i_\mathrm{qs} \tag{2.16}$$
$$v_\mathrm{qs} = R_\mathrm{s}i_\mathrm{qs} + L_\mathrm{q}\frac{di_\mathrm{qs}}{dt} + \omega_\mathrm{r}L_\mathrm{d}i_\mathrm{ds} + \omega_\mathrm{r}\psi_\mathrm{pm} \tag{2.17}$$

Fig. 2.2 shows the different reference frames and the physical current axes.

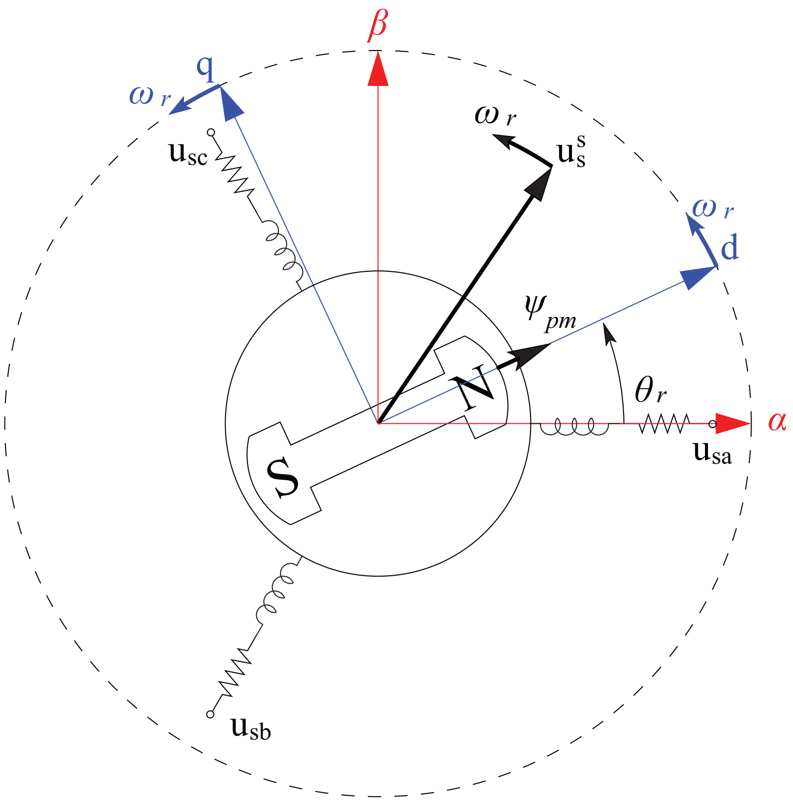

Figure 2.2: Wye-Connected 3 phase PMSM diagram with the stationary and the rotor reference frames

The equations describe the equivalent circuits for the two new axes as shown in Fig. 2.3.

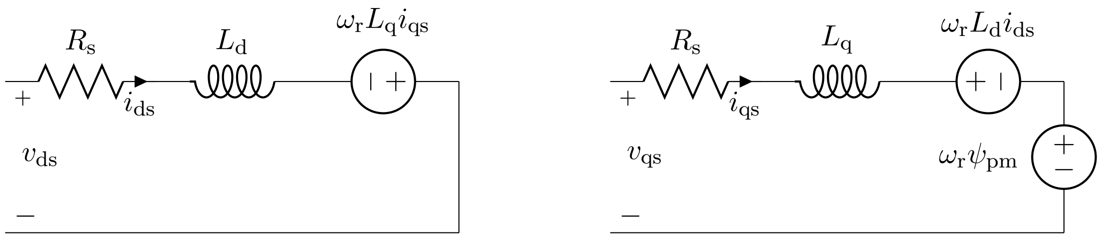

Figure 2.3: Rotor reference frame Equivalent Circuits

The instantaneous electrical torque T_e produced by the machine is expressed as function of the dq quantities as in Eq. 2.18, in which T_L is the mechanical load torque.

$$T_e = \frac{3}{2} p \left[\psi_{pm} i_{qs} + (L_d - L_q) i_{ds} i_{qs} \right] \tag{2.18}$$

The rotor speed is calculated through the shaft mechanical equation 2.19 in which J_m and f_v are respectively the motor-load joint moment of inertia and the shaft viscous friction.

$$T_e - T_L = \frac{J_m}{p} \frac{d\omega_r}{dt} + \frac{f_v}{p} \omega_r \tag{2.19}$$

2.2 Voltage Source Inverter

The typical schematics for a IGBT Volage Source Inverter is represented in Fig. 2.4

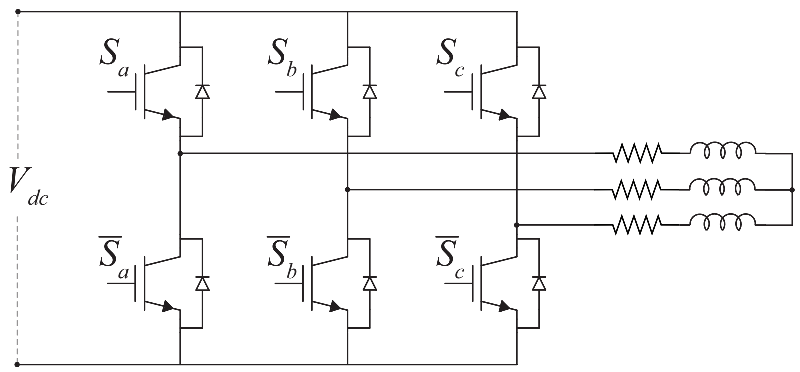

Figure 2.4: Circuit diagram of a 2-level full bridge IGBT Voltage Source Inverter with an RL load

The most concerning issue in a power converter is the current level in the switching devices in this case the IGBT semiconductors. In order to avoid the worst condition possible, namely the short circuit of the two switching device on the same leg to the supply voltage, the commands of the switching devices on the same leg are commanded with inverted logic commands. Nevertheless as additional precaution, a dead time is applied when a commutation occurs, ensuring that both switching devices are disconnected, before changing the logic of the gate command. This safety measure affect the voltage applied to the load terminals and it has to be compensated in order to enhance the drive performances, as it will be shown in chap. 6.

The terminal line-to-line voltages applied to the machine depend on the state of the switches and dc-link voltage (Eq. 2.20).

$$\begin{bmatrix} v_{\mathrm{ab}} \\ v_{\mathrm{bc}} \\ v_{\mathrm{ca}} \end{bmatrix} = V_{\mathrm{dc}} \begin{bmatrix} 1 & -1 & 0 \\ 0 & 1 & -1 \\ -1 & 0 & 1 \end{bmatrix} \begin{bmatrix} S_{\mathrm{a}} \\ S_{\mathrm{b}} \\ S_{\mathrm{c}} \end{bmatrix} \tag{2.20}$$

With the hypothesis that the wye-connected PMSM is a balanced 3-phase system, it is possible to write an expression for the line-to-neutral voltages applied to the machine as function of the switching states (Eq. 2.21).

$$\begin{bmatrix} v_{\mathrm{an}} \\ v_{\mathrm{bn}} \\ v_{\mathrm{cn}} \end{bmatrix} = \frac{V_{\mathrm{dc}}}{3} \begin{bmatrix} 2 & -1 & -1 \\ -1 & 2 & -1 \\ -1 & -1 & 2 \end{bmatrix} \begin{bmatrix} S_{\mathrm{a}} \\ S_{\mathrm{b}} \\ S_{\mathrm{c}} \end{bmatrix} \tag{2.21}$$

Modulation Technique

The inverter is to be controlled through a modulation technique in order to control properly the switches and apply to the machine's terminals the desired voltages. There are many possible methods for Pulse Width Modulation of a Voltage inverter. The method utilized in this thesis is the Space Vector Modulation. SVM is well known for its advantages in DC-Link exploitation, lower current harmonic production and ease of digital implementation. It has had a determinant impact in motor drive industry, with the significant contribute to change the standard for controlling the three phase bridge with a single modulation strategy instead of using a separate PWM for the control of each phase [Krishnan, 2010].

The principle of SVM is indeed to consider the space vector representation of the line-to-neutral voltages to be applied to the machine's terminals. The space vector is a spatial representation of the voltages in the physical magnetic-axes space. The idea is to modulate the voltages using the polar coordinates information of the desired voltage space vector. The possible configurations of the voltages applied to the machine correspond to the number of possible different combinations of the switches states. As previously mentioned the switches on the same leg are controlled by signals with inverted logic. This means that being the inverter states a 3 bits binary array, the possible combinations are $2^3 = 8$. These are the stationary space vectors which can be instantaneously applied through the switches. The 6 active space vectors and the 2 inactive (when the switches are all open) divide the voltage state space in 6 sectors, as it is possible to see in Fig. 2.5. It is not possible to apply different vectors than the ones given by the switches states, but it is possible to apply for a fraction of the switching period a sequence of 2 active vectors so that in average the desired line-to-neutral voltage vector is applied to the machine's terminals during the switching period.

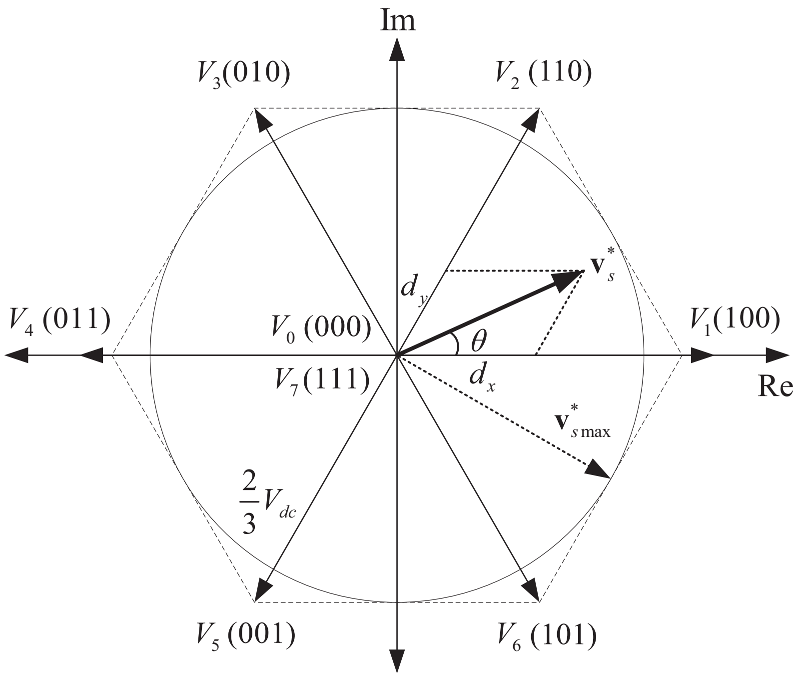

Figure 2.5: Space vector representation in the line-to-neutral machine coordinates of the Voltage Source Inverter

The maximum line-to-neutral voltage which is possible to apply to the machine's terminals is $2/3V_{\mathrm{dc}}$, this means that the maximum voltage reference applicable without any overmodulation technique is $\sqrt{3}/3V_{\mathrm{dc}}$ represented in the figure as the inner circle of the hexagon defined by the sectors. The two zero vectors are in the origin of the diagram since they are the equivalent to applying no voltage to the machine.

The reference voltage space-vector is expressed as a combination of the two adjacent active space vectors (V_{x} and V_{y}) applied for fractions of the switching period (d_{x} and d_{y}), and the two zero vectors which are applied for the residual fraction of the switching period (d_0)

$$\mathbf{v}_{\mathrm{s}}{}^{*} = d_{\mathrm{x}}\mathbf{V}_{\mathrm{x}} + d_{\mathrm{y}}\mathbf{V}_{\mathrm{y}} + d_0\mathbf{V}_0 \tag{2.22}$$

$$|\mathbf{v}_{\mathrm{s}}{}^{*}| \begin{bmatrix}\cos\theta \\ \sin\theta\end{bmatrix} = d_{\mathrm{x}}\frac{2}{3}V_{\mathrm{dc}}\begin{bmatrix}1 \\ 0\end{bmatrix} + d_{\mathrm{y}}\frac{2}{3}V_{\mathrm{dc}}\begin{bmatrix}\cos(\pi/3) \\ \sin(\pi/3)\end{bmatrix} + d_0\mathbf{V}_0 \tag{2.23}$$

The sum of the fractions of the switching period has to be equal to one.

$$d_{\mathrm{x}} + d_{\mathrm{y}} + d_0 = 1 \tag{2.24}$$

From Eq. 2.22-2.24 it is possible to calculate the duty cycles for the active and the zero vectors, as derived in Eq. 2.25-2.27. It is necessary to calculate the magnitude ($|\mathbf{v}_\mathrm{s}{}^*|$) and the argument ($\theta = \angle\mathbf{v}_\mathrm{s}{}^*$) of the voltage vector so that the duty cycles which give the desired voltage in average can be found.

$$d_\mathrm{x} = \frac{|\mathbf{v}_\mathrm{s}{}^*|\sqrt{3}}{V_\mathrm{dc}} \sin(\frac{n}{3}\pi - \theta) \tag{2.25}$$

$$d_\mathrm{y} = \frac{|\mathbf{v}_\mathrm{s}{}^*|\sqrt{3}}{V_\mathrm{dc}} \sin(\theta - \frac{n-1}{3}\pi) \tag{2.26}$$

$$d_\mathrm{z} = 1 - d_\mathrm{x} - d_\mathrm{y} \tag{2.27}$$

Field Oriented Control of PMSM 3

As stated in the introduction, the purpose of sensorless drive systems is to replace the information about the position coming from a physical sensor with the information from the machine's electrical variables. Normally sensorless drives are using the position estimation in a Field Oriented drive scheme. The classical Field Oriented Control for PMSM is presented in this chapter. This control method is based on the knowledge of the spatial position of the machine's magnetic fluxes. Therefore the original need for the knowledge of the physical rotor position.

3.1 Principle

Field Oriented Control is a well known technique and has constituted in the years the standard for speed and torque control of AC motors [Sen et al., 1996]. The main idea or inspiration that drove to its conception was to find an abstraction that allowed for decoupled control of torque and flux in AC machines, as much as it was normally possible for DC motors in which the armature brushes and permanent magnet flux axis were orthogonal by construction. The theory of reference frame transformations in AC machines reported in chap. 1 is the instrument which makes this abstraction possible. By aligning the reference frame to the rotor permanent magnet flux position it is possible to consider the voltages and the currents in the machine as rotating complex vectors and evaluate dynamically their component lying on the machine's physical flux axis which is rotating together with the rotor. Placing the current vector instantaneously orthogonal to the machine's flux will achieve fully decoupled control recreating the configuration of a DC machine with orthogonal magnetic physical axes, represented in Fig. 3.1. It is also possible to reduce the angle between the current vector and the machine's flux axis, operating in the field weakening region, as it is normally done in DC drives for higher speeds operation.

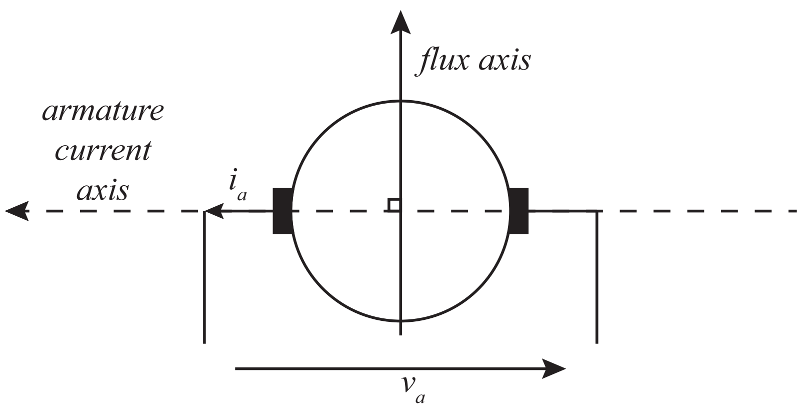

Figure 3.1: Orthogonal Flux and Armature Current axes in a DC machine [Wilamowski and Irwin, 2011]

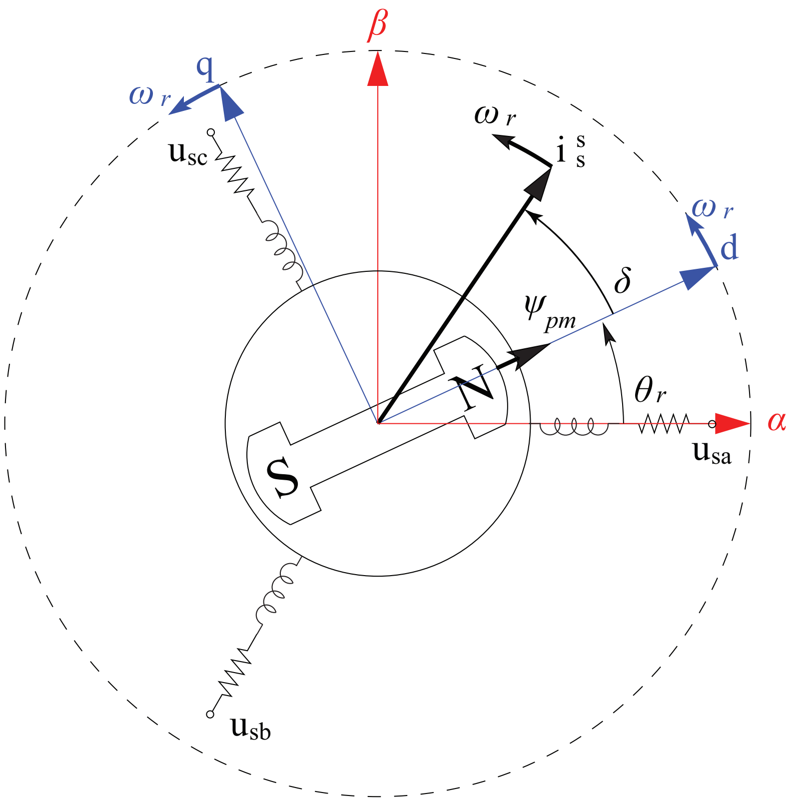

Figure 3.2: Space vector diagram with the rotor and the stationary reference frame

Fig. 3.2 shows the angle δ between the current vector and the machine's permanent flux axis. The angle is also called the torque angle, since it controls the torque/flux coupling. The current components in the rotor reference frame are:

$$\begin{bmatrix} i_{\mathrm{ds}} \\ i_{\mathrm{qs}} \end{bmatrix} = \mathbf{i}_{\mathrm{s}} \begin{bmatrix} \cos\delta \\ \sin\delta \end{bmatrix} \tag{3.1}$$

The torque is controlled by placing the current vector in a position relative to the rotor position. As said choosing as torque angle $\delta = 90°$ gives the maximum possible torque per current unit and decoupled control of torque and flux. This translates in setting the d-axis current to zero. In this thesis this approach for Field Oriented Control will be used in the first place. The current is controlled by applying the control voltages to the machine through the inverter. With proper control of the inverter through modulation it is possible to control the currents by means of a linear controller, in most cases a PI controller is used. In this thesis the reference value for the q-axis current will be generated by a closed loop speed controller which is using the speed measured by the sensor or estimated by the sensorless algorithm when the full sensorless scheme is applied. This is resumed in Fig. 3.3 which represents a typical scheme for sensorless Field Oriented Control with the two orthogonal axes current loops and the speed loop in cascade.

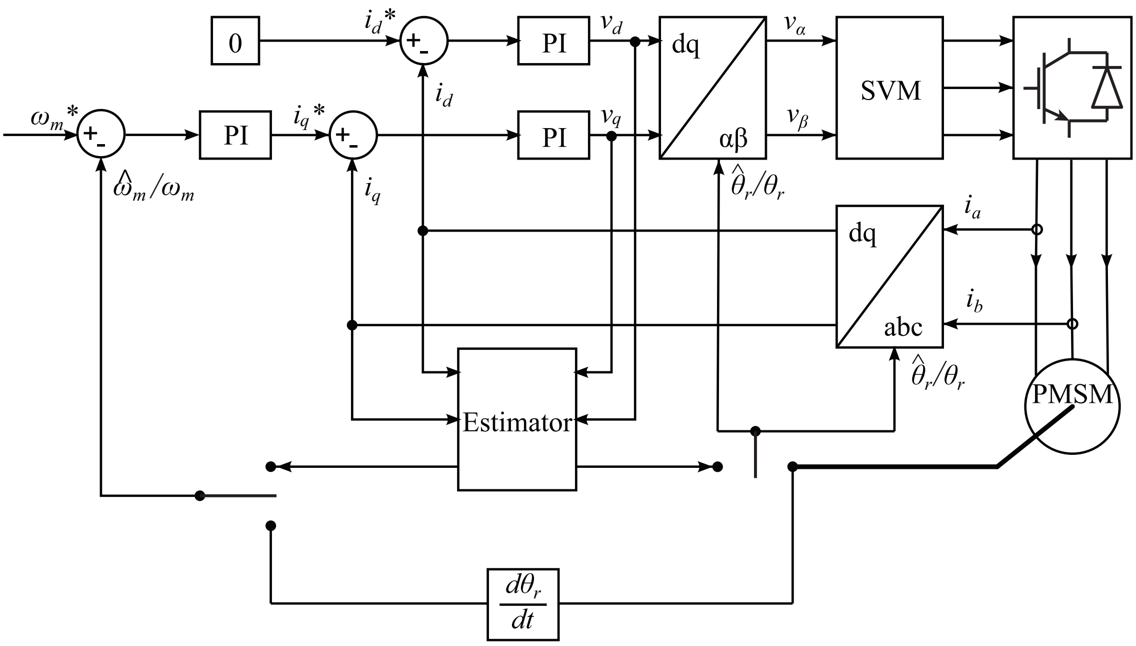

Figure 3.3: Block diagram for the applied FOC scheme

The design procedure is given in general for any kind of machine. The results of the design for the experimental test system used in this thesis are reported.

3.2 Current Control Design

The current controllers are required in order to control the currents in the machine through the Voltage Source Inverter. There is one current control loop for each of the two axes in the rotor dq reference frame.

The requirements for the current control loop are defined as:

- The bandwidth of the current loop should be ten times bigger than the sampling frequency. This requirement is equivalent to consider a rise time lower than 10 sampling periods (2 ms)
- The current response should have low or no overshoot, with a tolerance of maximum 5%

The transfer function for the equivalent dq machine circuits in Fig. 2.3 is obtained from the machine's equation in the dq reference frame (Eq. 2.16 - 2.17). It is possible to derive a linear transfer function between the corresponding axis voltage and current if the back-EMF coupling between the two axes is seen as a disturbance on the voltage control signal. The coupling can either be compensated by the integral term of the PI controller itself, or through a decoupling strategy. The model differential equations are transformed in their Laplace equivalent with the hypothesis of zero inital conditions.

$$v_{\mathrm{ds}}(s) = R_{\mathrm{s}} i_{\mathrm{ds}}(s) + sL_{\mathrm{d}} i_{\mathrm{ds}}(s) - \underbrace{\omega_{\mathrm{r}} L_{\mathrm{q}} i_{\mathrm{qs}}}_{e_{\mathrm{d}} = \text{distrubance}} \tag{3.2}$$

$$v_{\mathrm{qs}}(s) = R_{\mathrm{s}} i_{\mathrm{qs}}(s) + sL_{\mathrm{q}} i_{\mathrm{qs}}(s) + \underbrace{\omega_{\mathrm{r}} L_{\mathrm{d}} i_{\mathrm{ds}} + \omega_{\mathrm{r}} \psi_{\mathrm{pm}}}_{e_{\mathrm{q}} = \text{disturbance}} \tag{3.3}$$

By using the hypothesis of decoupled system or rejected back-EMF disturbance, the following axes transfer functions are yielded:

$$\frac{i_{\mathrm{ds}}(s)}{v_{\mathrm{ds}}(s)} = \frac{1}{sL_{\mathrm{d}} + R_{\mathrm{s}}} \tag{3.4}$$

$$\frac{i_{\mathrm{qs}}(s)}{v_{\mathrm{qs}}(s)} = \frac{1}{sL_{\mathrm{q}} + R_{\mathrm{s}}} \tag{3.5}$$

There are many possibilities to design the controller on the basis of the implementation technique. A common approach is to design the controller in the continuous Laplace domain and then discretize it using a discrete integration method for approximating the continuous integrator. Another possibility is to discretize the electrical system transfer function, and take into account the discretization effects already during the design of the controller. This approach is preferred since it allows to determine directly the stability conditions in the zeta domain, and to take into account the system's discrete delays. The electrical transfer function is discretized through a Zero Order Holder.

The delay between the voltage command and the current response depends on the experimental system configuration. Considering exclusively single update modulation strategy with fixed switching frequency, in many systems the voltage command applied is the one calculated in the previous iteration. These delay added to the switching period is considered equivalent to a fixed delay of 1.5 times the switching/control period, which the controller has to compensate for. In other applications, the PWM register is loaded in the same switching period in which the current sampling and the algorithm calculations occur, in this case a system delay of one switching period can be considered. These two kinds of inverter control delay are resumed in Fig. 3.4. The current sampling and A/D conversion occur in the time t_{AD}, the calculations for the control algorithm take place in the time t_{VC}.

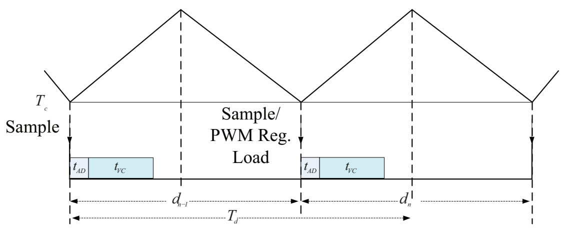

(a) Next period PWM updating

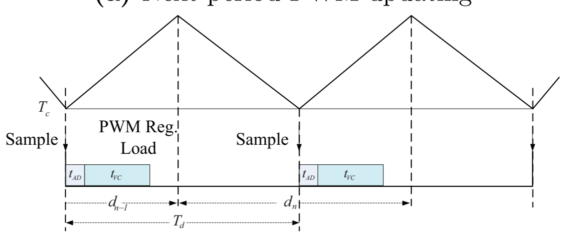

(b) Same period PWM updating

Figure 3.4: Source of delay in PWM [Guangzhen et al., 2013]

The system's discrete pulse transfer function is yielded by considering the sampled system and the unit delay.

$$G(z) = \frac{1}{z}\mathcal{Z}\left\{\frac{1-e^{-T_{\mathrm{s}}s}}{s}G(s)\right\} \tag{3.6}$$

$$
\begin{aligned}
&\Downarrow \quad z = e^{T_\mathrm{s} s} \\
G(z) &= \frac{1}{z}\left(1 - z^{-1}\right) \mathcal{Z}\left\{\frac{G(s)}{s}\right\} && (3.7) \\
&= \frac{1}{z}\left(1 - z^{-1}\right) \mathcal{Z}\left\{\frac{1}{s\left[R_\mathrm{s} + sL_\mathrm{s}\right]}\right\} && (3.8) \\
&= \frac{1}{z}\left(1 - z^{-1}\right) \frac{1}{R_\mathrm{s}} \mathcal{Z}\left\{\frac{\frac{R_\mathrm{s}}{L_\mathrm{s}}}{s\left(s + \frac{R_\mathrm{s}}{L_\mathrm{s}}\right)}\right\} && (3.9)
\end{aligned}
$$

Transforming the continuous transfer function to discrete yields the following pulse transfer function

$$
\begin{aligned}
G(z) &= \frac{1}{z}\left(1 - z^{-1}\right) \frac{1}{R_\mathrm{s}} \frac{z\left(1 - e^{-\frac{R_\mathrm{s}}{L_\mathrm{s}}T_\mathrm{s}}\right)}{(z-1)\left(z - e^{-\frac{R_\mathrm{s}}{L_\mathrm{s}}T_\mathrm{s}}\right)} && (3.10) \\
&= \frac{1 - e^{-\frac{R_\mathrm{s}}{L_\mathrm{s}}T_\mathrm{s}}}{R_\mathrm{s}\left(z - e^{-\frac{R_\mathrm{s}}{L_\mathrm{s}}T_\mathrm{s}}\right) z} && (3.11)
\end{aligned}
$$

As previously mentioned the chosen kind of controller is a PI. The RL circuit itself is stable in open-loop but the integral compensation is necessary in order to improve the dynamics and ensure null steady state error in case of non perfect decoupling between the two current axes. The chosen discrete PI features a Forward Euler integrator, therefore its discrete transfer function is

$$
G_\mathrm{PI}(z) = \frac{K_\mathrm{i}\, T_\mathrm{s} + K_\mathrm{p}(z-1)}{z-1} \qquad (3.12)
$$

The current control loop for a generic axis is represented in Fig. 3.5.

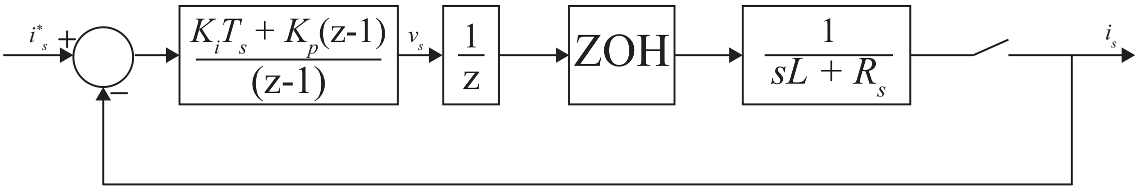

Figure 3.5: Discrete current control loop for each axis

The controller can be written in the zero-pole-gain form in order to assist the design.

$$
G_\mathrm{PI}(z) = \frac{K_\mathrm{i}\, T_\mathrm{s} + K_\mathrm{p}(z-1)}{z-1} = K_\mathrm{ol}\frac{z - z_0}{z-1} \qquad (3.13)
$$

$$
K_\mathrm{ol} = K_\mathrm{p} \quad , \quad z_0 = \frac{K_\mathrm{p} - K_\mathrm{i}\, T_\mathrm{s}}{K_\mathrm{p}}
$$

The open loop transfer function is then equal to

$$
G_\mathrm{ol}(z) = G_\mathrm{PI}(z)\, G(z) = \frac{K_\mathrm{ol}(z - z_0)}{z-1}\, G(z) \qquad (3.14)
$$

It is now possible to place arbitrarily the controller zero and then draw the root locus of the open loop transfer function G_ol. This makes it possible to place the closed loop poles according to the desired dynamics and requirements.

The design procedure is carried out for the experimental system described in ch: 7. The machine is nonsalient, so the design for one controller loop axis is valid for both the axes. The plant transfer function with the actual parameters is reported in Eq. 3.15.

$$G(z) = \frac{0.09017}{z(z - 0.9838)} \tag{3.15}$$

The controller zero is placed so that the slow plant pole is clamped. This is necessary in order to make the response dynamics faster.

$$z_0 = 0.9838 \tag{3.16}$$

The root locus for the open loop transfer function with the clamped slow pole is shown in Fig. 3.6-3.7

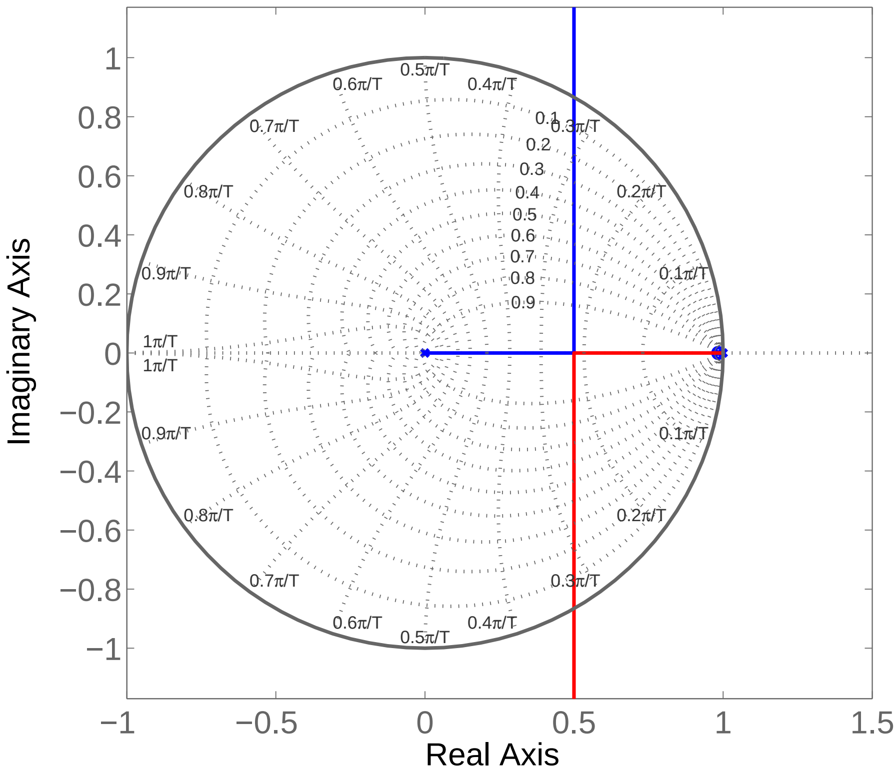

Figure 3.6: Root Locus of the current control open loop transfer function

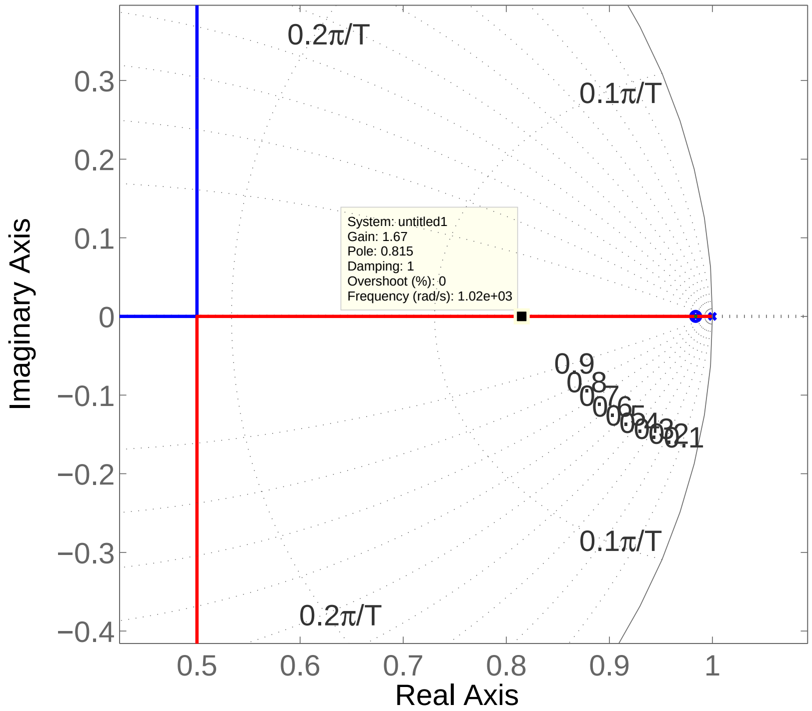

Figure 3.7: Root Locus of the current control open loop transfer function - detail

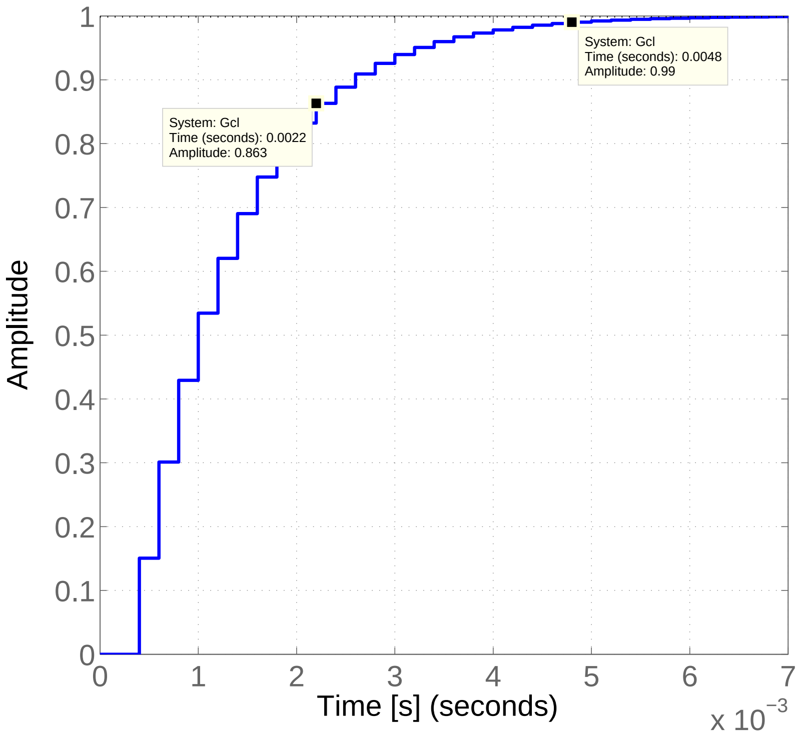

Figure 3.8: Step Response of the current control closed loop transfer function

The pole highlighted in Fig. 3.7 is the slowest for the indicated open-loop gain and thus characterizes the system's dynamics. This is used as first design for the current controller loop. The design will be tuned during the experiments in order to satisfy the given requirements.

The performance of the controller is first evaluated at standstill, injecting a DC current in the machine's phase windings. A double step is given so that the response of the current controller can be evaluated without considering the effects on the dynamics due to the charging of passive components in the inverter. The experimental controller response is shown in Fig. 3.9-3.10.

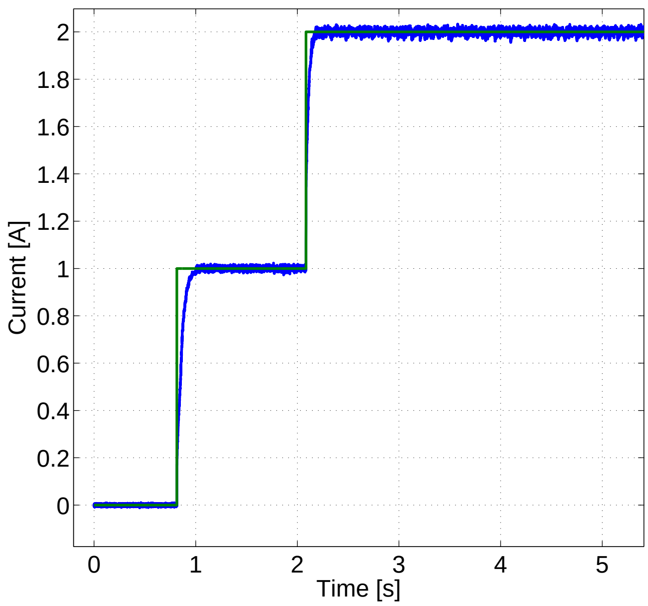

Figure 3.9: Experimental Step response of the current control loop

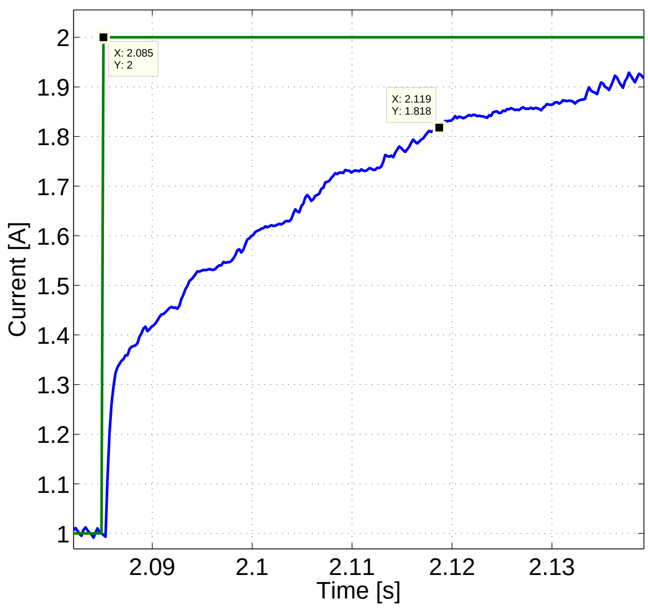

Figure 3.10: Experimental Step response of the current control loop - detail

As it is possible to see in Fig. 3.10 despite the initial appearance of the current response may suggest that the response has the desired fast dynamics and low rise-time, but the response slows down after the first 2ms. This is due to the low frequency slow pole which the controller should clamp but due to some imprecision in the parameters for controller design, the slow dynamics related to the open-loop pole survive in the closed-loop response. As it is possible to see in Fig. 3.6-3.7 and in the Uncompensated Open Loop Bode Plot in Fig. 3.11, there is a significant margin for increasing the gain without risking instability or overshoot outside the requirements. The PI gains are increased by a factor of 1.5 in order to achieve a faster response and to move the surviving low-frequency pole towards the controller zero.

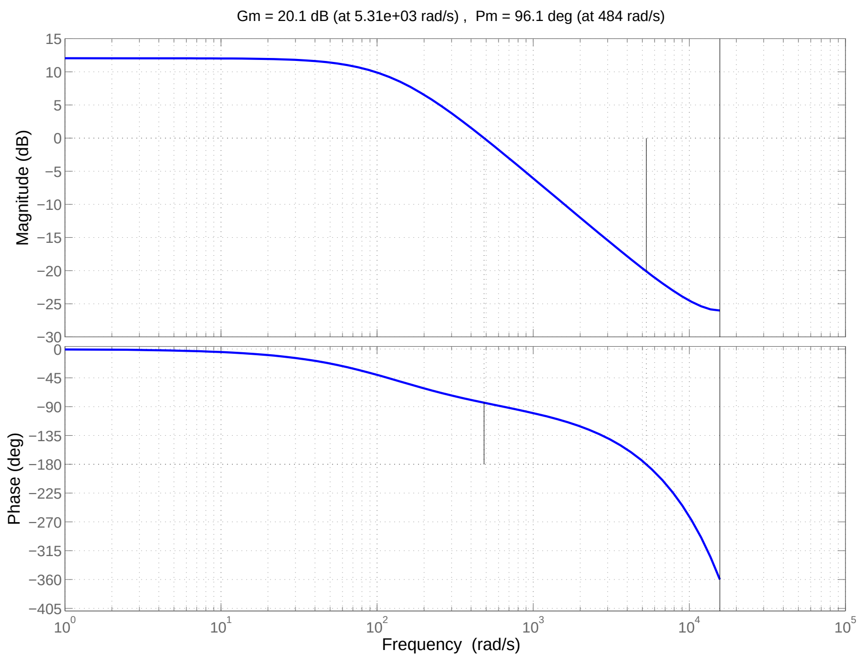

Figure 3.11: Bode Plot for the uncompensated plant sampled data system

The current controller response with the adjusted loop gain is shown in Fig. 3.12. The requirements on the rise time are respected. Experiments have shown that further increasing the open loop gain achieves a full compensation of the slow dynamics but implies the underdamping of the complex poles which in turn causes excessive overshoot.

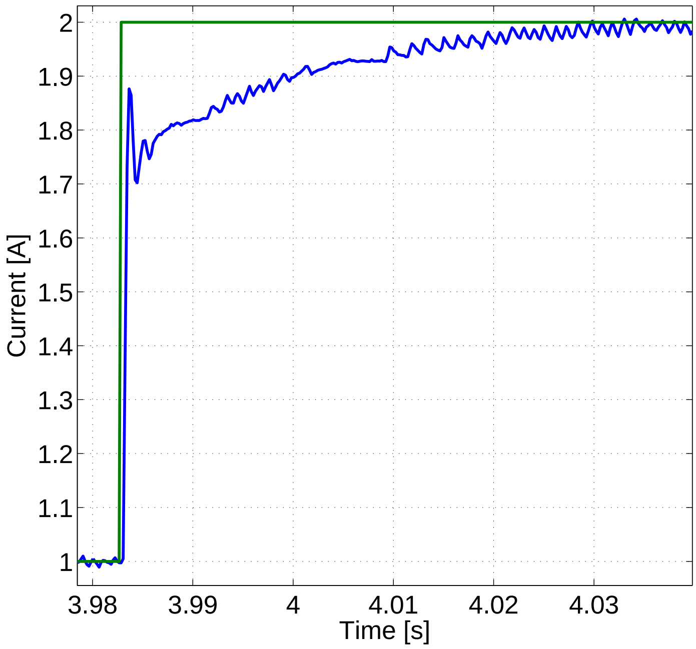

Figure 3.12: Experimental Step response of the current control loop with augmented open loop gain - detail

3.3 Speed Control Design

As mentioned the speed is controlled through an outer PI control loop. The bandwidth of the speed controller is smaller than the inner current control loop. This control scheme is commonly called cascade control. This consideration leads to the control requirements, here listed:

- The bandwidth (rise time) of the speed control loop should be between 5-10 times slower (higher), so that the inner loop dynamics do not affect the outer loop behaviour. The required rise time should be between 10 and 20 ms
- The speed controller has to be able to compensate for torque variations
- The overshoot should be as low as possible, not exceeding 25%

The transfer function for the speed control loop is obtained from the mechanical equation of the PMSM system and the expression for the electrical torque produced by the machine (Eq. 2.18 and 2.19). The mechanical equation and the electrical torque equation are transformed in their Laplace domain equivalent and then combined. The transfer function from q-axis current to mechanical speed is so yielded.

$$T_{\mathrm{e}}(s) = K_{\mathrm{T}} i_{\mathrm{qs}}(s) = \frac{3}{2} p \psi_{\mathrm{pm}} i_{\mathrm{qs}}(s) \tag{3.17}$$

$$T_{\mathrm{e}} = f_{\mathrm{v}} \omega_{\mathrm{m}}(s) + J_{\mathrm{m}}\ s\ \omega_{\mathrm{m}}(s) + \underbrace{T_{\mathrm{L}}}_{\text{disturbance}} \tag{3.18}$$

$$\frac{\omega_{\mathrm{m}}(s)}{i_{\mathrm{qs}}(s)} = \frac{K_{\mathrm{t}}}{J_{\mathrm{m}}\ s + f_{\mathrm{v}}} \tag{3.19}$$

The load torque is considered as a disturbance for the control variable, namely the torque/q-axis current. Also in this case it is preferred to consider the control loop as a sampled data system. So the control design is conducted directly in discrete.

The closed loop transfer function of the current control loop is considered in the design of the controller. In order to simplify the analysis, it is assumed that the slow pole of the electrical inner system is fully compensated by the controller zero. The result achieved in the current response rise-time allows for this consideration. The block diagram for the speed control loop is represented in Fig. 3.13.

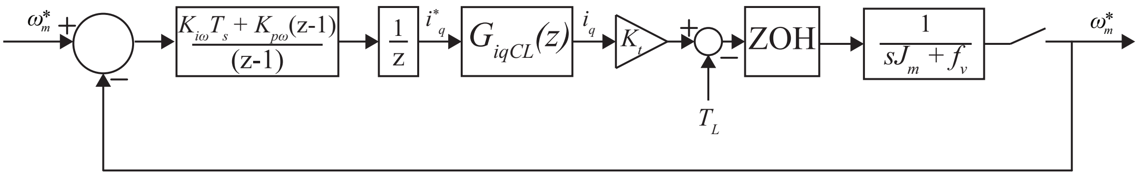

Figure 3.13: Block diagram for the speed control loop

A delay of one sample is considered in order to account for all the system's delays. Using the same approach as for the current loop design, the pulse transfer function of the sampled data mechanical system is obtained.

$$G_{\mathrm{mech}}(z) = \frac{1 - e^{-\frac{f_{\mathrm{v}}}{J_{\mathrm{m}}} T_{\mathrm{s}}}}{f_{\mathrm{v}} \left(z - e^{-\frac{f_{\mathrm{v}}}{J_{\mathrm{m}}} T_{\mathrm{s}}} \right)} \tag{3.20}$$

The system itself is stable and has only small steady state error if regulated in negative feedback. However the PI controller is necessary in order to improve the response dynamics and to effectively compensate the torque disturbances in the control loop. The chosen controller is of the same typology as in the current loop. The open loop includes the transfer function of the current control loop $G_{\mathrm{iqCL}}(z)$. The overall open-loop transfer function is shown in Eq. 3.21.

$$G_{\mathrm{mechOL}}(z) = \frac{K_{\mathrm{i}\omega}\, T_{\mathrm{s}} + K_{\mathrm{p}\omega}(z-1)}{z-1}\, \frac{1}{z}\, G_{\mathrm{iqCL}}(z)\, G_{\mathrm{mech}}(z) \tag{3.21}$$

The transfer functions relative to the mechanical system of the experimental setup described in chap. 7 is reported in Eq. 3.22 together with the current control loop transfer function in Eq. 3.23, as designed in section 3.2. Since the viscous friction is small with regards to the moment of inertia, the mechanical pole corresponds to an integrator pole in $z = 1$.

$$G_{\mathrm{mech}}(z) = \frac{0.01007}{z-1} \tag{3.22}$$

$$G_{\mathrm{iqCL}}(z) = \frac{0.3259}{z^2 - z + 0.3259} \tag{3.23}$$

Again it is possible to place the controller zero arbitrarily in order to accelerate the slow mechanical dynamics, and then adjust the open-loop gain through root locus analysis, so that the closed loop poles can be set as required.

The zero is placed close to the integrator so that it can compensate the phase delay at the low frequencies.

$$z_0 = 0.995 \tag{3.24}$$

The root locus plot for the overall open loop transfer function is shown in Fig. 3.14

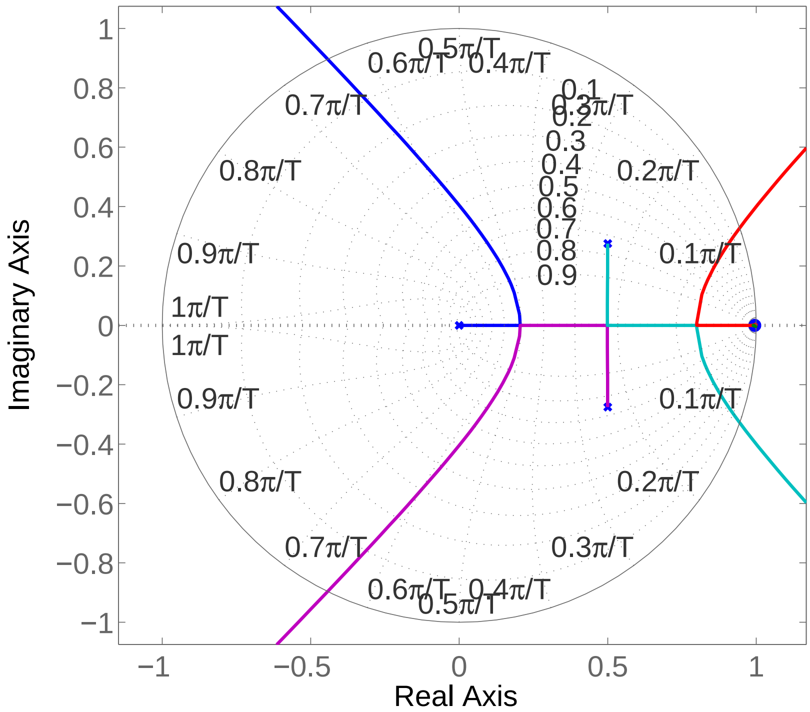

Figure 3.14: Root locus for the speed control open-loop transfer function

A conservative choice of a small gain can satisfy all the requirements.

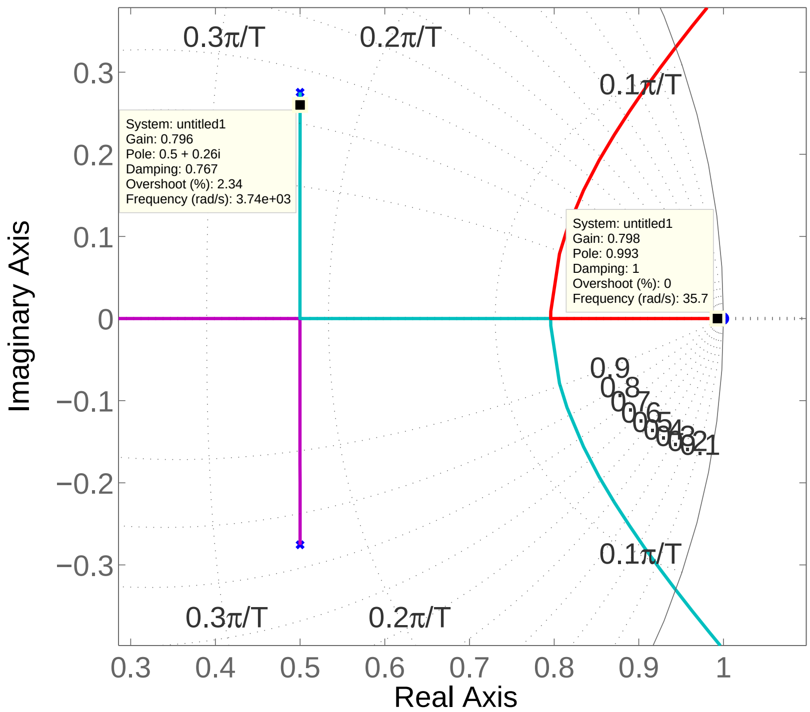

Figure 3.15: Root locus for the speed control open-loop transfer function - detail

The PI gains are calculated from the chosen open loop gain, as it was done for the current control loop. The designed controller leads to the following step response for the speed control loop which is shown to meet the design requirements in Fig. 3.16.

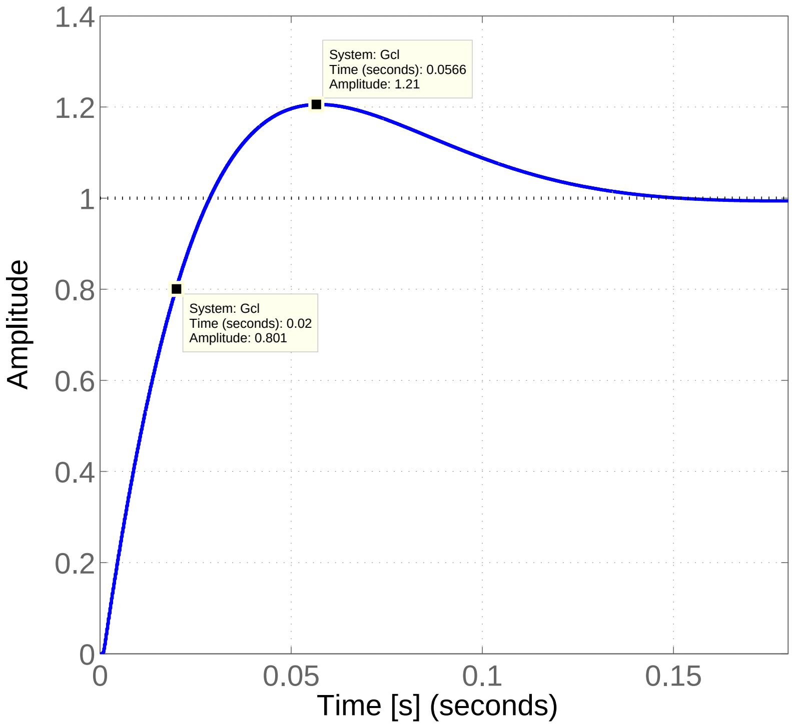

Figure 3.16: Step Response of the speed control closed loop transfer function

3.4 Anti Integral Wind-up

Due to the modulation limit in the power converter, described in chap. 2, the control variable commanded in the current control loop may be subjected to physical limits. Other than this the control should always respect the particular hardware limitations for each application. In order to avoid any possible issue, the controller outputs are limited within a prefixed saturation limit. When the control variable goes beyond these saturation limits, the well known phenomenon of Integral Wind-up occurs. During the time in which the control variable remains within the saturation limits, the integral term continues to grow until the error changes sign. At the time this happens the integral term is still very high and this will lead to an oscillatory response until it ´´discharges" fully. The solution is to reset or compensate the integral term while the control variable is within saturation limits.

The Integral Wind-up compensation scheme in Fig. 3.17 is used both in the speed and in the currents loops. The solution is based on the back-calculation of the integral term compensation from the saturated control variable [Zakladu, 2005].

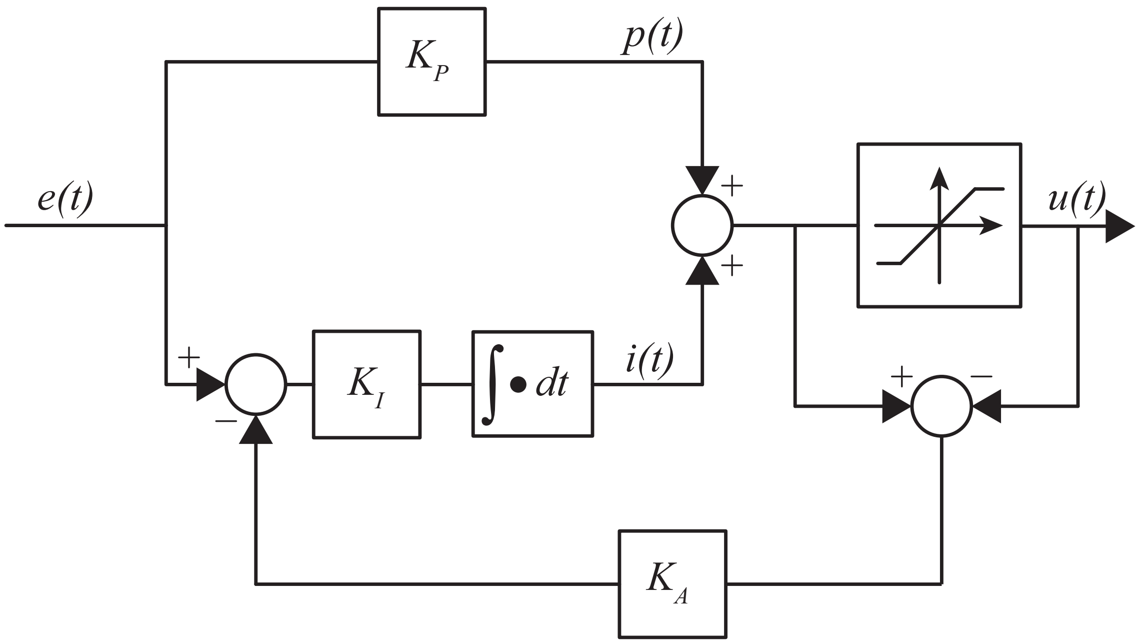

Figure 3.17: Back-calculation tracking anti-windup scheme

The anti wind-up gain K_a needs to be higher than the Integral gain K_i, so that it can effectively compensate the integrator charge when the control variable is saturated. In this thesis it is chosen for every control loop an anti wind-up gain equal to twice the Integral gain $K_\text{a} = 2\ K_\text{i}$.

Back-EMF based Sensorless Control of PMSM 4

In this chapter the concept of back-EMF based sensorless control for PMSM is presented. Then two different methods are presented and explained along with an analytical analysis of stability and robustness. Finally performances are evaluated through simulations and experiments.

4.1 Principle

As seen in chap. 3, the Field Oriented Control scheme needs a precise information about the rotor position. The standard solution is to get the mechanical position of the rotor from a sensor. A sensorless strategy should be able to get an information about the position of the rotor from the electrical variables. As seen in Eq. 2.11 - 2.17 the model equations of PMSM both in the stationary and the rotating reference frame show that the back-EMF is the only electrical variable that instantaneously depends on the rotor's electrical speed and position. By using the information coming from current sensors and the voltage commands calculated in the Field Oriented Control scheme, it is possible to estimate the back-EMF components on the basis of the machine's equations calculation. Rotor position and speed are then estimated from the back-EMF components. The estimation strategy is represented in a simplified way in Fig. 4.1.

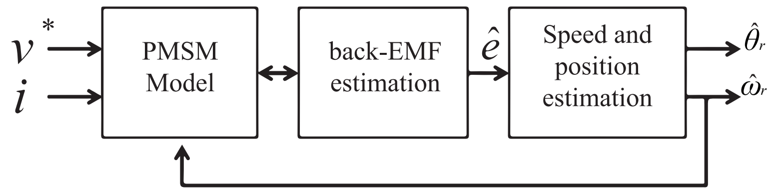

Figure 4.1: Simplified Block Diagram representation of back-EMF based sensorless estimation

For the stationary reference frame case, by estimating the components of the back-emf, reported in Eq. 4.1, it is possible to get an information about the speed and the rotor position.

$$\begin{bmatrix} e_\alpha \\ e_\beta \end{bmatrix} = \omega_\mathrm{r}\psi_\mathrm{pm} \begin{bmatrix} -\sin\theta_\mathrm{r} \\ \cos\theta_\mathrm{r} \end{bmatrix} \tag{4.1}$$

This kind of estimators commonly calculates the position and the speed of the rotor by evaluating the argument and the module of the estimated back-EMF vector in polar coordinates [Vas, 1998]. If the rotating reference frame model is considered, it is possible to estimate the position and the speed by means of an *estimated* reference frame rotating at the estimated speed and in which the back-EMF components are function of the position error between the estimated rotor angle and the actual one. From the $\alpha\beta$ stationary frame machine model, it is possible to derive the model of the machine in the estimated reference frame expressed as function of the dq reference frame inductances [Morimoto et al., 2002].

$$\begin{bmatrix} v_\delta \\ v_\gamma \end{bmatrix} = \begin{bmatrix} R_\mathrm{s} + \frac{d}{dt}L_\mathrm{d} & -\omega_\mathrm{r} L_\mathrm{q} \\ \omega_\mathrm{r} L_\mathrm{d} & R_\mathrm{s} + \frac{d}{dt}L_\mathrm{q} \end{bmatrix} \begin{bmatrix} i_\delta \\ i_\gamma \end{bmatrix} + \begin{bmatrix} e_\delta \\ e_\gamma \end{bmatrix} \tag{4.2}$$

$$\begin{bmatrix} e_\delta \\ e_\gamma \end{bmatrix} = \omega_\mathrm{r}\psi_\mathrm{pm} \begin{bmatrix} -\sin\tilde{\theta}_\mathrm{r} \\ \cos\tilde{\theta}_\mathrm{r} \end{bmatrix} + \mathbf{L}_\mathrm{a}\frac{d}{dt}\begin{bmatrix} i_\delta \\ i_\gamma \end{bmatrix} + \omega_\mathrm{r}\mathbf{L}_\mathrm{b}\begin{bmatrix} i_\delta \\ i_\gamma \end{bmatrix} + (\hat{\omega}_\mathrm{r} - \omega_\mathrm{r})\mathbf{L}_\mathrm{c}\begin{bmatrix} i_\delta \\ i_\gamma \end{bmatrix} \tag{4.3}$$

The variables vectors in the stationary coordinates are rotated by the estimated rotor angle expressed as function of the position error, $\hat{\theta}_\mathrm{r} = \theta_\mathrm{r} + \tilde{\theta}_\mathrm{r}$. The $\delta\gamma$ components of the back-EMF in the estimated reference frame are function of the estimated speed $\hat{\omega}_\mathrm{r}$ and the position error $\tilde{\theta}_\mathrm{r}$. The three additional inductances matrix are derived from the vector rotation of the axes inductances in the estimated reference frame

$$\begin{aligned} \mathbf{L}_\mathrm{a} &= \begin{bmatrix} -(L_\mathrm{d} - L_\mathrm{q})\sin^2\tilde{\theta}_\mathrm{r} & (L_\mathrm{d} - L_\mathrm{q})\sin\tilde{\theta}_\mathrm{r}\cdot\cos\tilde{\theta}_\mathrm{r} \\ (L_\mathrm{d} - L_\mathrm{q})\sin\tilde{\theta}_\mathrm{r}\cdot\cos\tilde{\theta}_\mathrm{r} & (L_\mathrm{d} - L_\mathrm{q})\sin^2\tilde{\theta}_\mathrm{r} \end{bmatrix} \\ \mathbf{L}_\mathrm{b} &= \begin{bmatrix} -(L_\mathrm{d} - L_\mathrm{q})\sin\tilde{\theta}_\mathrm{r}\cdot\cos\tilde{\theta}_\mathrm{r} & -(L_\mathrm{d} - L_\mathrm{q})\sin^2\tilde{\theta}_\mathrm{r} \\ -(L_\mathrm{d} - L_\mathrm{q})\sin^2\tilde{\theta}_\mathrm{r} & (L_\mathrm{d} - L_\mathrm{q})\sin\tilde{\theta}_\mathrm{r}\cdot\cos\tilde{\theta}_\mathrm{r} \end{bmatrix} \\ \mathbf{L}_\mathrm{c} &= \begin{bmatrix} (L_\mathrm{d} - L_\mathrm{q})\sin\tilde{\theta}_\mathrm{r}\cdot\cos\tilde{\theta}_\mathrm{r} & -L_\mathrm{d}\cos^2\tilde{\theta}_\mathrm{r} - L_\mathrm{q}\sin^2\tilde{\theta}_\mathrm{r} \\ L_\mathrm{d}\sin^2\tilde{\theta}_\mathrm{r} + L_\mathrm{q}\cos^2\tilde{\theta}_\mathrm{r} & -(L_\mathrm{d} - L_\mathrm{q})\sin\tilde{\theta}_\mathrm{r}\cdot\cos\tilde{\theta}_\mathrm{r} \end{bmatrix} \end{aligned} \tag{4.4}$$

Fig. 4.2 shows the estimated reference frame, the actual rotor reference frame and the relative position error $\tilde{\theta}_\mathrm{r}$

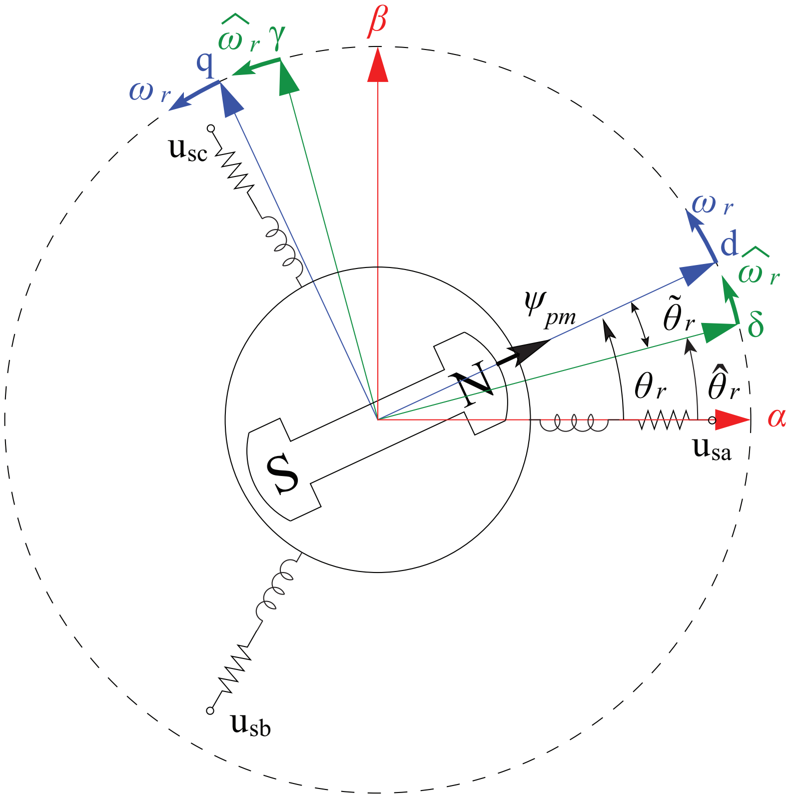

Figure 4.2: Estimated reference frame and rotor reference frame

Beyond the conventional direct axis lying on the rotor's magnetic axis, the estimated reference frame and the corresponding angle error are shown. The angle error shown in the picture affects crucially the performances of every sensorless control method since it causes an imprecise field orientation as it has been discussed in chap. 3.

The imperfect field orientation affects also the electromagnetic torque expressed as function of the estimated axes currents. Due to the position error, the components lying on the rotor reference frame dq axes are merely projection of the estimated currents. Eq. 2.18 becomes Eq. 4.6

$$T_\mathrm{e} = \frac{3}{2}p\left[\psi_\mathrm{pm}(i_\gamma \cos\tilde{\theta}_\mathrm{r} + i_\delta \sin\tilde{\theta}_\mathrm{r}) + (L_\mathrm{d} - L_\mathrm{q})(i_\delta \cos\tilde{\theta}_\mathrm{r} + i_\gamma \sin\tilde{\theta}_\mathrm{r})(i_\delta \sin\tilde{\theta}_\mathrm{r} + i_\gamma \cos\tilde{\theta}_\mathrm{r})\right] \tag{4.5}$$

$$= \frac{3}{2}p\left[\psi_\mathrm{pm}(i_\gamma \cos\tilde{\theta}_\mathrm{r} + i_\delta \sin\tilde{\theta}_\mathrm{r}) + (L_\mathrm{d} - L_\mathrm{q})\left(i_\delta i_\gamma + \frac{i_\delta^2 + i_\gamma^2}{2}\sin 2\tilde{\theta}_\mathrm{r}\right)\right] \tag{4.6}$$

Eq. 4.2 - 4.3, the generic model in the estimated reference frame, allow for a first important consideration. In both the stationary and rotational frame based back-EMF estimators, there is a significant difference of the position error impact on the estimated components of the back-EMF, between machines with low or no saliency (ideally SPMSMs) and machines with higher saliency (IPMSMs). This consideration is intuitively explainable by thinking at the non-salient machines which have regular air gap and whose inductance is approximately invariant with regards to the rotor position. In this case the error in the instantaneous position estimation does not propagate recursively in the back-EMF components estimation since all the machine's parameters are isotropic.

The main difference between the estimators in the stationary reference frame and the ones in the estimated rotating reference frame is that, being the former ones AC filters, they introduce a phase delay in the estimated variables while the latter ones introduce only a negligible delay, since they are DC estimation based on DC signals. This phenomenon is well known for the stationary class of flux estimators and is also called "integral drift" [Eskola, 2006]. Other than this the stationary estimators output an absolute estimation of the rotor position while the rotating reference frame estimators extrapolate information about the rotor position error, so they need to be combined with another estimation. In this thesis only methods based on the rotating reference frame will be considered since the introduced phase delay may affect the performances of the online estimation method presented in the next chapter.

The model in the estimated reference frame is normally considered too complicated in order too be used as estimation law, and many estimation algorithms assume that the estimation error for both speed and position has negligible contribute to the back-EMF estimation even in salient machines. This assumption can result in unstable operation for IPMSMs sensorless algorithms if the estimation of the back-EMF components is not improved with some dependency on the machine's saliency effects [Lee and Ha, 2012].

The back-EMF can not provide itself a reliable speed estimation at low speeds, since the voltage applied to the machine mostly compensates for the voltage drops in stator resistance and inductance at low speeds. In order to enhance performances the injection of high frequency current signals has been proposed in order to improve the estimation at near zero speeds by taking advantage of the machine's anisotropy. In this thesis these methods are not considered as it is desired to overcome the problem only by means of the fundamental frequency operation, so that the methods described can suit applications in which acoustic noise and torque ripples caused by the HF signal injection are undesired.

4.2 Extended Matsui Second Method

In this thesis a method for sensorless position estimation is considered. It is based on the back-emf component estimation with the help of a rotating reference frame model.

The method originally proposed in [Matsui, 1996], and discussed in [Nahid-Mobarakeh et al., 2004] and [Eskola, 2006] is analysed. This method is commonly known as *Second Matsui Method* or *Current Model Matsui Method* and it is well known among the back-EMF based methods in the estimated reference frame. All the effects of saliency are not considered in the model used for the estimation. This assumption is taken for the ease of analysis and since the used experimental system features an SPMSM.

Following analytical and simulation results, the sensorless algorithm is implemented on the provided experimental setup, described in chap. 7, which features an SPMSM.

The original Matsui method presented in [Matsui, 1996], was called "current model estimator". The reason for the name lies in the estimation technique used for the back-EMF components through the estimated reference frame machine model. The back-EMF components are evaluated by tracking the measured currents with an estimation which is based on the integration of the model's equations. The difference between the estimated current and the measured one will give the estimated back-EMF components.

Two fundamental hypotheses make the derivation of the method rather uncomplicated.

- All the machine parameters in the model are initially guessed correct. The voltage references from the current controller are supposed to be exactly the voltages applied to the machine's terminal.
- The inital position error $\hat{\theta}_{\mathrm{r}}$ is considered really small, meaning that it is possible to approximate through First Order Taylor's development the trigonometric functions of the position error and to neglect the effects of saliency which make the model in Eq. 4.2-4.3 complicated.

This hypothesis lead to the following simplified model in the estimated reference frame

$$\frac{di_\delta}{dt} = \frac{1}{L_{\mathrm{d}}}\left(v_\delta - R_{\mathrm{s}}i_\delta + \hat{\omega}_{\mathrm{r}}L_{\mathrm{q}}i_\gamma + \underbrace{\omega_{\mathrm{r}}\psi_{\mathrm{pm}}\sin\tilde{\theta}_{\mathrm{r}}}_{e_\delta}\right) \tag{4.7}$$

$$\frac{di_\gamma}{dt} = \frac{1}{L_{\mathrm{q}}}\left(v_\gamma - R_{\mathrm{s}}i_\gamma - \hat{\omega}_{\mathrm{r}}L_{\mathrm{d}}i_\delta - \underbrace{\omega_{\mathrm{r}}\psi_{\mathrm{pm}}\cos\tilde{\theta}_{\mathrm{r}}}_{e_\gamma}\right) \tag{4.8}$$

By considering the Forward Euler discretization of the state space model of the machine, it is ideally possible to evaluate the value of the next sample of the currents by knowing the derivative and the value of the previous sample (Eq. 4.9-4.10).

$$i_\delta(k+1) = i_\delta(k) + T_{\mathrm{s}}\frac{di_\delta}{dt}(k) \tag{4.9}$$

$$i_\gamma(k+1) = i_\gamma(k) + T_{\mathrm{s}}\frac{di_\gamma}{dt}(k) \tag{4.10}$$

The hypothesis on the small initial position error allows for considering null the back-emf component lying on the δ axis $e_\delta = 0$. This consideration leads to the state space model used for the estimation of the current derivative.

$$\frac{d\hat{i_\delta}}{dt} = \frac{1}{\hat{L_\mathrm{d}}}\left(v_\delta - \hat{R_\mathrm{s}} i_\delta + \hat{\omega_\mathrm{r}}\hat{L_\mathrm{q}} i_\gamma\right) \tag{4.11}$$

$$\frac{d\hat{i_\gamma}}{dt} = \frac{1}{\hat{L_\mathrm{q}}}\left(v_\gamma - \hat{R_\mathrm{s}} i_\gamma - \hat{\omega_\mathrm{r}}\hat{L_\mathrm{d}} i_\delta - \hat{\omega_\mathrm{b}}\hat{\psi_\mathrm{pm}}\cos\tilde{\theta}_\mathrm{r}\right) \tag{4.12}$$

The hat symbol on the parameters indicates that they are the supposed parameters used in the estimator. $\hat{\omega_\mathrm{b}}$ is the estimated speed of the flux in the estimation model. Eq. 4.11-4.12 are discretized and used for calculating the estimated current derivative at the k-th sample. Then the estimated current in the next sample is calculated from the estimated derivative and the measured current for the same sample, as shown in Eq. 4.11-4.12.

$$\hat{i_\delta}(k+1) = i_\delta(k) + T_\mathrm{s}\frac{d\hat{i_\delta}}{dt}(k) \tag{4.13}$$

$$\hat{i_\gamma}(k+1) = i_\gamma(k) + T_\mathrm{s}\frac{d\hat{i_\gamma}}{dt}(k) \tag{4.14}$$

By using the two initial hypotheses on parameters precision and small position error it is possible to approximate the current error as a function of the two back-EMF components in the estimated reference frame. Subtracting Eq. 4.9 and 4.10 from Eq. 4.13 and 4.14 yields Eq. 4.15 and 4.16

$$\tilde{i_\delta}(k+1) = \hat{i_\delta}(k+1) - i_\delta(k+1) = -\frac{T_\mathrm{s}}{L_\mathrm{d}} e_\delta \approx -\frac{T_\mathrm{s}}{L_\mathrm{d}}\psi_\mathrm{pm}\omega_\mathrm{r}\tilde{\theta}_\mathrm{r} \tag{4.15}$$

$$\tilde{i_\gamma}(k+1) = \hat{i_\gamma}(k+1) - i_\gamma(k+1) = \frac{T_\mathrm{s}}{L_\mathrm{q}}(e_\gamma - \hat{\omega_\mathrm{b}}\psi_\mathrm{pm}) \approx \frac{T_\mathrm{s}}{L_\mathrm{q}}\psi_\mathrm{pm}(\omega_\mathrm{r} - \hat{\omega_\mathrm{b}}) \tag{4.16}$$

As mentioned, assuming small position error, the trigonometric functions of the error are approximated with first order Taylor approximation, i.e. $\sin\tilde{\theta}_\mathrm{r} \approx \tilde{\theta}_\mathrm{r}$ and $\cos\tilde{\theta}_\mathrm{r} \approx 1$.
The speed is estimated through Eq. 4.17 and 4.18, using a combination of the information from the γ axis current error and an information about the position error coming from the δ axis error.

$$\hat{\omega_\mathrm{b}}(k+1) = \hat{\omega_\mathrm{b}}(k) + k_\alpha \tilde{i_\gamma}(k+1) \tag{4.17}$$

$$\hat{\omega_\mathrm{r}}(k+1) = \hat{\omega_\mathrm{b}}(k+1) + k_\beta \tilde{i_\delta}(k+1) \tag{4.18}$$

With $k_\alpha = \frac{L_\mathrm{d}}{T_\mathrm{s}}\alpha$ and $k_\beta = \frac{L_\mathrm{q}}{T_\mathrm{s}}\beta$. $\hat{\omega_\mathrm{b}}$ is used as auxiliary speed for the estimation, and is calculated from the γ axis current error, $\hat{\omega_\mathrm{r}}$ is the estimated speed, calculated through the auxiliary speed and the correction of the position error which is in turn calculated from the δ axis current error. The position estimation is calculated by integrating the estimated speed (Eq. 4.19).

$$\hat{\theta}_\mathrm{r}(k+1) = \hat{\theta}_\mathrm{r}(k) + T_\mathrm{s}\,\hat{\omega_\mathrm{r}}(k+1) \tag{4.19}$$

The whole sensorless method is resumed in Fig. 4.3.

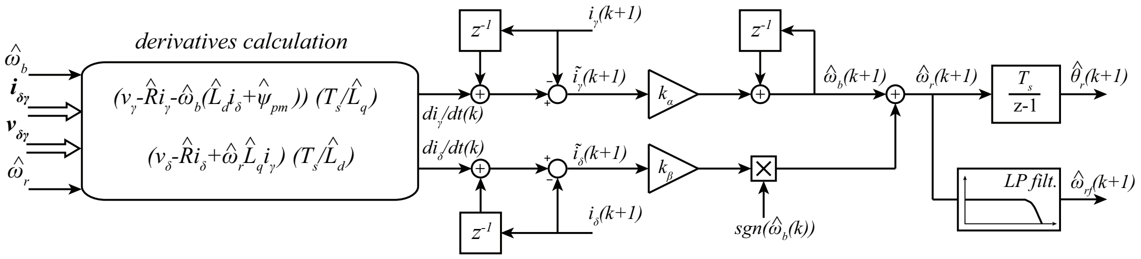

Figure 4.3: Block diagram for the Second Matsui Method [Eskola, 2006]

The diagram shows that the estimated speed is filtered by a digital low pass filter before it is used in the digital speed loop. The digital filter is necessary in any practical application. A first order low pass digital filter is designed in appendix A. The filter cut-off frequency is set to 15 Hz through experiments.

It is possible to notice that the auxiliary estimated speed $\hat{\omega_{\mathrm{b}}}$ is used in Eq. 4.12 instead of the final estimated speed $\hat{\omega_{\mathrm{r}}}$. This is done so that Eq. 4.17 becomes a discrete low-pass filter rather than a discrete integrator. With proper estimator parameters the auxiliary estimated speed rapidly converges to the speed calculated from the estimated back-emf components.

Substituting Eq. 4.16 and 4.15 into Eq. 4.17 and 4.18 respectively yields the following discrete sensorless control law for speed estimation:

$$\hat{\omega_{\mathrm{b}}}(k+1) = (1-\alpha\psi_{\mathrm{pm}})\hat{\omega_{\mathrm{b}}}(k) + \alpha\psi_{\mathrm{pm}}\cos\tilde{\theta}_{\mathrm{r}}\omega_{\mathrm{r}}(k) \tag{4.20}$$

$$\hat{\omega_{\mathrm{r}}}(k+1) = \hat{\omega_{\mathrm{b}}}(k+1) + \beta\hat{e_{\delta}}(k) \tag{4.21}$$

Eq. 4.20 resembles a Discrete Low Pass Filter (cf. appendix A, Eq. A.8), so that the auxiliary speed $\hat{\omega_{\mathrm{b}}}$ converges quickly to the speed estimated on the γ axis, i.e. $\omega_{\mathrm{r}}\cos\tilde{\theta}_{\mathrm{r}}$

4.2.1 Closed-Loop Convergence Conditions

The stability analysis for the whole closed loop system is conducted so that it possible to obtain the convergence criteria for the estimator parameters α and β. The stability analysis is based on the first (also called *indirect*) Lyapunov's method [Slotine et al., 1991].

An important simplification is made in order to derive the convergence conditions. It is supposed that the machine is controlled in a field oriented control scheme with maximum torque per ampere density for a non-salient machine, i.e. $i_{\delta} = 0$. This assumption simplifies Eq. 4.6 making it easier to derive analytical solutions to the differential equation. In addition the Load Torque is considered to be dependent on the shaft's speed and to be null at zero speed (the hypothesis is consistent with the static and viscous friction effects)

The dynamics of the position error are defined in Eq. 4.22

$$\frac{d\,\tilde{\theta}_{\mathrm{r}}}{dt} = \hat{\omega_{\mathrm{r}}} - \omega_{\mathrm{r}} \tag{4.22}$$

With the consideration made on the sensorless estimation algorithm for the auxiliary speed filtering in Eq. 4.20 it is possible to substitute the converged auxiliary speed $\hat{\omega_{\mathrm{b}}} = \omega_{\mathrm{r}}\cos\tilde{\theta}_{\mathrm{r}}$

in Eq. 4.21. The following expression for the estimated speed as function of the position error and the actual speed is yielded.

$$\hat{\omega_{\mathrm{r}}} = \omega_{\mathrm{r}} \cos \tilde{\theta_{\mathrm{r}}} + \beta \psi_{\mathrm{pm}} \omega_{\mathrm{r}} \sin \tilde{\theta_{\mathrm{r}}} \tag{4.23}$$

The expression found for the estimated speed, Eq. 4.23, is combined in Eq. 4.22 in order to yield the closed loop non-linear system with the state vector $x = [\tilde{\theta_{\mathrm{r}}} \quad \omega_{\mathrm{r}}]^T$. The mechanical equation for the PMSM system, Eq. 2.19, is used together with the electromagnetic torque expression with the estimated electrical quantities (Eq. 4.6) in order to study the dynamics of the closed-loop system with the estimated speed and the position error.

$$\begin{cases} \frac{d\tilde{\theta_{\mathrm{r}}}}{dt} & = \omega_{\mathrm{r}} \cos \tilde{\theta_{\mathrm{r}}} + \beta \psi_{\mathrm{pm}} \omega_{\mathrm{r}} \sin \tilde{\theta_{\mathrm{r}}} - \omega_{\mathrm{r}} \\ \frac{J}{p} \frac{d\omega_{\mathrm{r}}}{dt} & = \frac{3}{2} p \ \psi_{\mathrm{pm}} i_{\gamma} \cos \tilde{\theta_{\mathrm{r}}} - T_{\mathrm{L}}(\frac{\omega_{\mathrm{r}}}{p}) \end{cases} \tag{4.24}$$

The principle of the first Lyapunov's method is to find the equilibria of the non-linear system and prove local asymptotic stability of the linearised subsystems. This will prove the local stability of the non-linear system in the proximity of the equilibria. The idea is to make stable the equlibria in which the estimator has the expected behaviour so that it is converging to the actual value of the estimated quantity.

The method relates the stability of the linearized subystems to the local stability of the non-linear system as here listed.

- If all the eigenvalues of the linearized system have the real part strictly negative (i.e. the linearized system is strictly stable), then it is possible to conclude that the corresponding equilibrium is asymptotically stable.
- if at least one eigenvalue of the linearized system has strictly positive real part (i.e. the linearized system is unstable), then the corresponding equilibrium is unstable.
- In case the eigenvalues of the linearized system have negative or null real part (i.e. the linearized system is marginally stable), it is not possible to conclude anything on the behaviour of the nonlinear system in the proximity of the corresponding equilibrium.

The equilibria are yielded by finding the solutions to the non-linear system Eq. 4.24, while imposing the equilibrium condition, i.e. $\frac{dx}{dt} = 0$

$$\begin{cases} 0 & = \omega_{\mathrm{r}}(\cos \tilde{\theta_{\mathrm{r}}} + \beta \psi_{\mathrm{pm}} \sin \tilde{\theta_{\mathrm{r}}} - 1) \\ 0 & = \frac{3}{2} p \ \psi_{\mathrm{pm}} i_{\gamma} \cos \tilde{\theta_{\mathrm{r}}} - T_{\mathrm{L}} \end{cases} \tag{4.25}$$

The first two equilibria are found in Eq. 4.25 by first considering the partial solution $\omega_{\mathrm{r1}} = \omega_{\mathrm{r2}} = 0$. Since the load torque has to be zero at stand still, then the position error has to be $\tilde{\theta_{\mathrm{r1,2}}} = \pm\frac{\pi}{2} + 2k\pi$

$$\begin{cases} 0 & = \omega_{\mathrm{r}} \\ T_{\mathrm{L}}(0) & = 0 = \frac{3}{2} p \ \psi_{\mathrm{pm}} i_{\gamma} \cos \tilde{\theta_{\mathrm{r}}} \end{cases} \tag{4.26}$$

The other two equilibria are found by solving the trigonometric equation in Eq. 4.25, with the half angle tangent substitutions, Eq. 4.27 and 4.28.

$$\sin\tilde{\theta}_{\mathrm{r}} = \frac{2\tan\frac{\tilde{\theta}_{\mathrm{r}}}{2}}{1+\tan^2\frac{\tilde{\theta}_{\mathrm{r}}}{2}} \tag{4.27}$$

$$\cos\tilde{\theta}_{\mathrm{r}} = \frac{1-\tan^2\frac{\tilde{\theta}_{\mathrm{r}}}{2}}{1+\tan^2\frac{\tilde{\theta}_{\mathrm{r}}}{2}} \tag{4.28}$$

$$\cos\tilde{\theta}_{\mathrm{r}} + \beta\psi_{\mathrm{pm}}\sin\tilde{\theta}_{\mathrm{r}} - 1 = 0 \tag{4.29}$$

$$\frac{1-\tan^2\frac{\tilde{\theta}_{\mathrm{r}}}{2} + \beta\psi_{\mathrm{pm}} 2\tan\frac{\tilde{\theta}_{\mathrm{r}}}{2}}{1+\tan^2\frac{\tilde{\theta}_{\mathrm{r}}}{2}} - 1 = 0 \tag{4.30}$$

The remaining two solutions to the equations are easily found.

$$\tan\frac{\tilde{\theta}_{\mathrm{r}}}{2}\left(\beta\ \psi_{\mathrm{pm}} - \tan\frac{\tilde{\theta}_{\mathrm{r}}}{2}\right) = 0 \tag{4.31}$$

$$\tilde{\theta_{\mathrm{r3}}} = 2k\pi \quad , \quad \tilde{\theta_{\mathrm{r4}}} = 2\arctan(\beta\ \psi_{\mathrm{pm}}) + 2k\pi \tag{4.32}$$

$$\omega_{\mathrm{r3}} = f(T_{\mathrm{L}}) = f\left(\frac{3}{2}p\psi_{\mathrm{pm}}i_\gamma\right) = \omega_{\mathrm{r}}^{\circ} \quad , \quad \omega_{\mathrm{r4}} = f\left(\frac{3}{2}p\psi_{\mathrm{pm}}i_\gamma\cos\tilde{\theta_{\mathrm{r4}}}\right) = \omega_{\mathrm{r}}^{+} \tag{4.33}$$

The four equilibria are resumed in Tab. 4.1

$\boldsymbol{x}_{\mathrm{e}}$	$\boldsymbol{\omega}_{\mathrm{re}}$	$\tilde{\boldsymbol{\theta}}_{\mathrm{re}}$
x_{e1}	0	$\frac{\pi}{2} + 2k\pi$
x_{e2}	0	$-\frac{\pi}{2} + 2k\pi$
x_{e3}	$\omega_{\mathrm{r}}^{\circ}$	$2k\pi$
x_{e4}	ω_{r}^{+}	$2\arctan(\beta\ \psi_{\mathrm{pm}}) + 2k\pi$

Table 4.1: Equilibria of the closed loop non-linear system

Obviously the best equilibrium is x_{e3}. Therefore it is desired that the system trajectories converge always to this point.

The stability of the four linearized subsystems corresponding to the 4 equilibria is now studied. The Jacobian of the non-linear system Eq. 4.24 is calculated in Eq. 4.34

$$\frac{\partial f(x)}{\partial x} = \begin{bmatrix} \omega_{\mathrm{re}}(\beta\psi_{\mathrm{pm}}\cos\tilde{\theta_{\mathrm{re}}} - \sin\tilde{\theta_{\mathrm{re}}}) & \cos\tilde{\theta_{\mathrm{re}}} + \beta\psi_{\mathrm{pm}}\sin\tilde{\theta_{\mathrm{re}}} - 1 \\ -\frac{3}{2}\frac{p^2}{J}\psi_{\mathrm{pm}}i_\gamma\sin\tilde{\theta_{\mathrm{re}}} & -\frac{p}{J}\frac{d\,T_{\mathrm{L}}(\omega_{\mathrm{re}})}{d\omega_{\mathrm{r}}} \end{bmatrix} \tag{4.34}$$

The generic linearized subsystem is defined as in Eq. 4.35

$$\frac{dx}{dt} = \left(\frac{\partial f(x)}{\partial x}\right)_{x=x_{\mathrm{e}}}(x - x_{\mathrm{e}}) \tag{4.35}$$

The four linearized subsystems are yielded by substituting the equilibria in Eq. 4.34.

$$\left(\frac{\partial f(x)}{\partial x}\right)_{x=x_{\mathrm{e1}}} = \begin{bmatrix} 0 & \beta\psi_{\mathrm{pm}} - 1 \\ -\frac{3}{2}\frac{p^2}{J}\psi_{\mathrm{pm}}i_\gamma & -\frac{p}{J}T_{\mathrm{L0}} \end{bmatrix} \tag{4.36}$$

$$\left(\frac{\partial f(x)}{\partial x}\right)_{x=x_{e2}} = \begin{bmatrix} 0 & -\beta\psi_{\mathrm{pm}} - 1 \\ \frac{3}{2}\frac{p^2}{J}\psi_{\mathrm{pm}}i_\gamma & -\frac{p}{J}T_{\mathrm{L0}} \end{bmatrix} \tag{4.37}$$

$$\left(\frac{\partial f(x)}{\partial x}\right)_{x=x_{e3}} = \begin{bmatrix} \beta\psi_{\mathrm{pm}}\omega_{\mathrm{r}}^{\circ} & 0 \\ 0 & -\frac{p}{J}\frac{d\,T_{\mathrm{L}}(\omega_{\mathrm{r}}^{\circ})}{d\omega_{\mathrm{r}}} \end{bmatrix} \tag{4.38}$$

$$\left(\frac{\partial f(x)}{\partial x}\right)_{x=x_{e4}} = \begin{bmatrix} -\beta\psi_{\mathrm{pm}}\omega_{\mathrm{r}}^{+} & 0 \\ -\frac{3}{2}\frac{p^2}{J}\psi_{\mathrm{pm}}i_\gamma\sin\theta_{\mathrm{r4}} & -\frac{p}{J}\frac{d\,T_{\mathrm{L}}(\omega_{\mathrm{r}}^{+})}{d\omega_{\mathrm{r}}} \end{bmatrix} \tag{4.39}$$

The estimator parameter β is chosen as in Eq. 4.40.

$$\beta = \frac{-b\ \mathrm{sgn}(\hat{\omega}_{\mathrm{r}})}{\hat{\psi_{\mathrm{pm}}}} \tag{4.40}$$

The stability conditions of the single parameter b are obtained through Routh-Hurwitz criterion for the 4 linearized subsystems in app. B. They are resumed in Fig. 4.4.

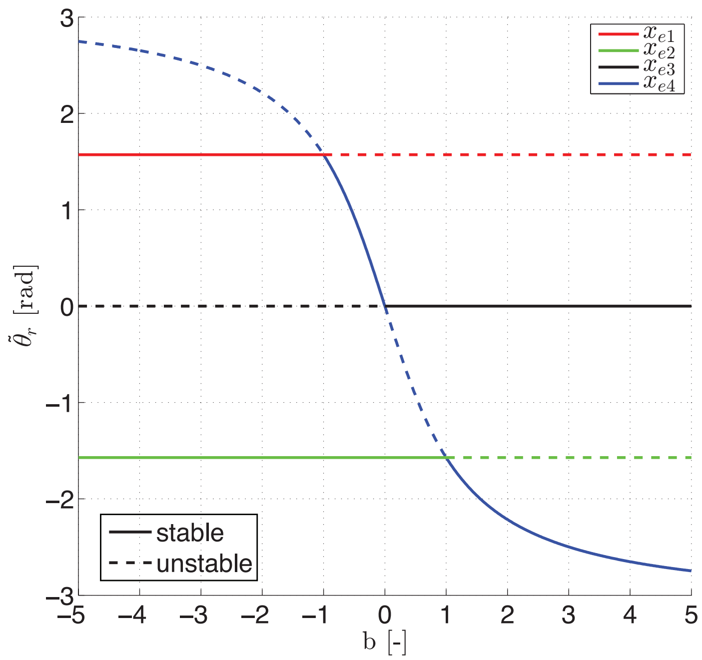

Figure 4.4: Stability of the 4 equilibria, function of the sensorless parameter b, with [Nahid-Mobarakeh et al., 2004]

It is possible to see that, in order to keep the desired equilibrium x_{e3} stable, b has to be positive. Then according to Fig. 4.4 other two possible undesired equilibria can be stable, depending on b being lower or higher than 1. Considerations on the domain of attraction of the desired equilibrium are made for both cases.

The domain of convergence of the estimator is studied analytically through phase-plane analysis [Slotine et al., 1991] for the two aforementioned cases. The system trajectories for different estimator parameters are shown in the phase portraits in Fig. 4.5-4.6. The solutions were calculated numerically and plotted in the state-space together. The circles indicate the initial conditions from which the trajectories start. The red dots indicate the system equilibria previously found. The parameters used in the calculations are the ones of the experimental system described in chap. 7. The operating conditions are such that the actual rotor electrical speed is 100 rad/s.

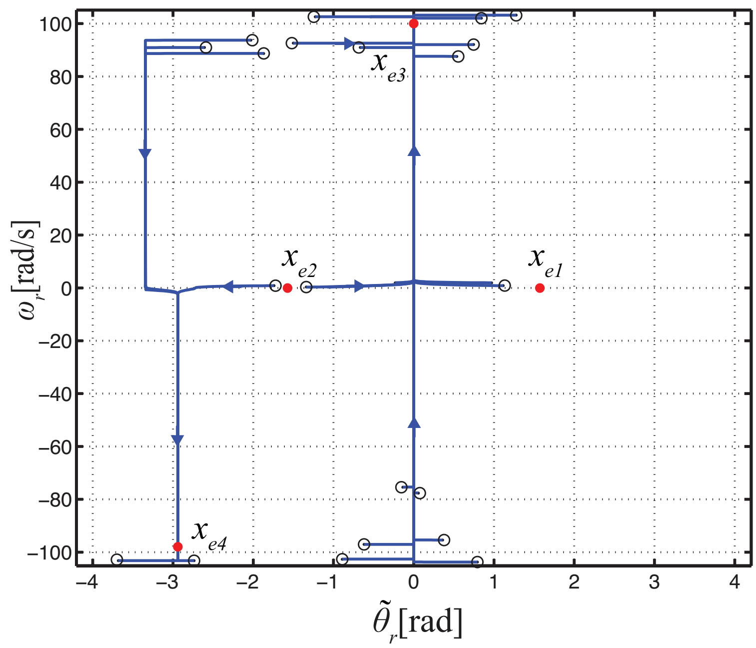

Figure 4.5: Phase portrait of the closed loop non-linear system for b=5

Fig. 4.5 shows that the system converges properly to the desired equilibrium for position errors below a certain threshold($\approx \frac{\pi}{2}$). The domain of attraction of the undesired equilibrium is too large for being accepted.

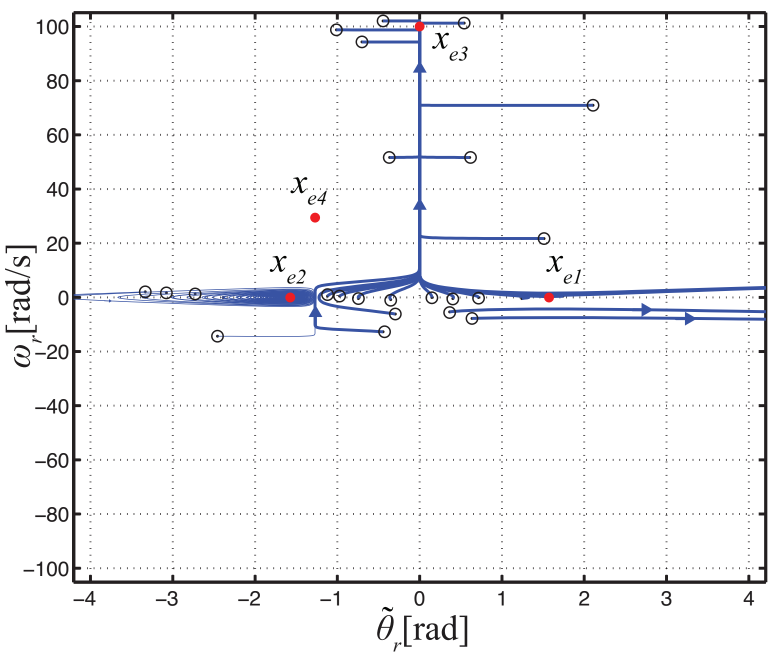

Figure 4.6: Phase portrait of the closed loop non-linear system for b=0.7

Fig. 4.6 shows that the domain of attraction of the desired equilibrium x_{e3} is larger than the previous case with $b > 1$. In this case, initial position errors up to a certain threshold ($\approx \pi$) still allow the system trajectories to converge to the desired equilibrium. Even if the domain of attraction of the desired solution is larger than the previous case, the limited convergence to the desired equilibrium of the estimator, may still be unacceptable in terms of robustness.

4.2.2 Globally converging estimator

The position estimator should globally converge to the desired equilibrium. [Nahid-Mobarakeh et al., 2004] proposes a variable structure observer law for the speed estimator. The idea is to tweak the estimator gain β according to the current state of the system, so that the undesired equilibria are made unstable in what it would normally be their domain of convergence.

It is possible to see from Fig. 4.6 that when the equilibrium $x_{\mathrm{e}2}$ is stable (i.e. $0 < b < 1$), the equilibrium $x_{\mathrm{e}4}$ is a saddle point located in the second quadrant of the bidimensional state space, in a specific limited area. Following Eq. 4.32 and 4.40, $\tilde{\theta_{\mathrm{r}4}} = -2\arctan(b \cdot \mathrm{sgn}(\hat{\omega_{\mathrm{r}}}))$, for $0 < b < 1$ the position error will be $-\frac{\pi}{2} < \tilde{\theta_{\mathrm{r}4}} < 0$.

Similarly, in Fig. 4.5 it is shown that when the equilibrium $x_{\mathrm{e}4}$ is stable (i.e. $b > 1$), it is located in a specific area within the fourth quadrant, since for $b > 1$ the position error will be $\tilde{\theta_{\mathrm{r}4}} < -\frac{\pi}{2}$.

The two areas are highlighted respectively in green and in red in Fig. 4.7, which represents the entire phase plane, divided in different regions according to the sign of the back-EMF components, reported in Eq. 4.41 and 4.42 for convenience.

$$e_\delta = \omega_{\mathrm{r}} \sin \tilde{\theta}_{\mathrm{r}} \tag{4.41}$$

$$e_\gamma = \omega_{\mathrm{r}} \cos \tilde{\theta}_{\mathrm{r}} \tag{4.42}$$

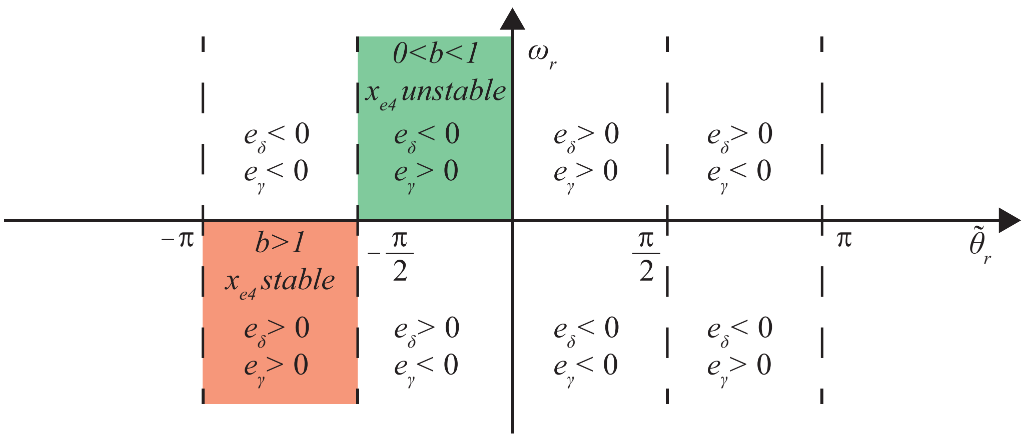

Figure 4.7: The $\tilde{\theta}_{\mathrm{r}}$-$\omega_{\mathrm{r}}$ phase plane divided in areas by which sign the back-EMF components can have

It is possible to approximately know in which quadrant is the state of the system, by evaluating the sign of the estimated back-EMF components calculated in the algorithm. This information makes it possible to tweak the gain of the estimator so that the undesired equilibrium is globally made unstable. This will lead the system to converge globally to the desired equilibrium.

The estimator law changes from Eq. 4.21 to the variable structure estimation law of Eq. 4.43.

$$\hat{\omega_{\mathrm{r}}}(k+1) = \hat{\omega_{\mathrm{b}}}(k+1) + \beta \cdot f(\hat{e_\delta}(k), \hat{e_\gamma}(k)) \cdot \hat{e_\delta}(k) \tag{4.43}$$

Based on the consideration previously made on the system's trajectories in the $\tilde{\theta}_{\mathrm{r}}$-$\omega_{\mathrm{r}}$ phase plane shown in Fig. 4.7, the following conditions are outlined for the variable structure estimation law.

- It must always keep the desired equilibrium x_{e3} stable, so the estimator gain should always be positive.
- It must make the undesired state x_{e4} unstable when the system is in its domain of attraction, so the estimator gain should be changed to a value comprised between 0 and 1 whenever the system is in the red area.
- It must ensure that the system does not converge to the other undesired equilibria x_{e2} which is between the two regions, so the estimator gain should be changed to a value greater than 1, whenever it is inside the green area and thus sufficiently far from the undesired equilibrium x_{e4}.

The conditions are resumed in Eq. 4.44

$$\begin{cases} b \cdot f(\hat{e_\delta}, \hat{e_\gamma}) < 1, & \forall(\tilde{\theta}_{\mathrm{r}}, \omega_{\mathrm{r}}) \in \text{Red area} \\ b \cdot f(\hat{e_\delta}, \hat{e_\gamma}) > 1, & \forall(\tilde{\theta}_{\mathrm{r}}, \omega_{\mathrm{r}}) \in \text{Green area} \end{cases} \tag{4.44}$$

The variable structure estimation law proposed in [Nahid-Mobarakeh et al., 2004] which satisfies the previous conditions is the following:

$$f(\hat{e_\delta}, \hat{e_\gamma}) = 1 - \zeta \cdot \mathrm{sgn}(\hat{e_\delta}), \qquad \text{with } 0 < \zeta < 1 \tag{4.45}$$

The estimation law is dependent only on the estimated δ-axis component and requires in addition just the calculation of its sign.
The globally converging estimation law is resumed in Eq. 4.46

$$\begin{cases} \hat{\omega_{\mathrm{b}}}(k+1) & = (1 - \alpha\psi_{\mathrm{pm}})\hat{\omega_{\mathrm{b}}}(k) + \alpha\psi_{\mathrm{pm}} \cos\tilde{\theta}_{\mathrm{r}}\omega_{\mathrm{r}}(k) \\ \hat{\omega_{\mathrm{r}}}(k+1) & = \hat{\omega_{\mathrm{b}}}(k+1) + \beta(1 - \zeta \cdot \mathrm{sgn}(\hat{e_\delta}(k))) \cdot \hat{e_\delta}(k) \end{cases} \tag{4.46}$$

with

$$\begin{aligned} 0 <& \alpha < \frac{1}{\psi_{\mathrm{pm}}} \\ 0 <& \zeta < 1 \\ \beta =& -\frac{b}{\hat{\psi_{\mathrm{pm}}}} \cdot \mathrm{sgn}(\hat{\omega_{\mathrm{r}}}) \end{aligned} \tag{4.47}$$

The conditions set on the parameters in Eq. 4.47 are obtained from the discussed convergence conditions and from the definition of the variable structure estimation law of Eq. 4.44

The phase-plane analysis of the variable structure estimation laws verifies the global convergence of the algorithm to the desired equilibrium, as it is shown in Fig. 4.8. The chosen parameters satisfy the conditions of Eq. 4.47.

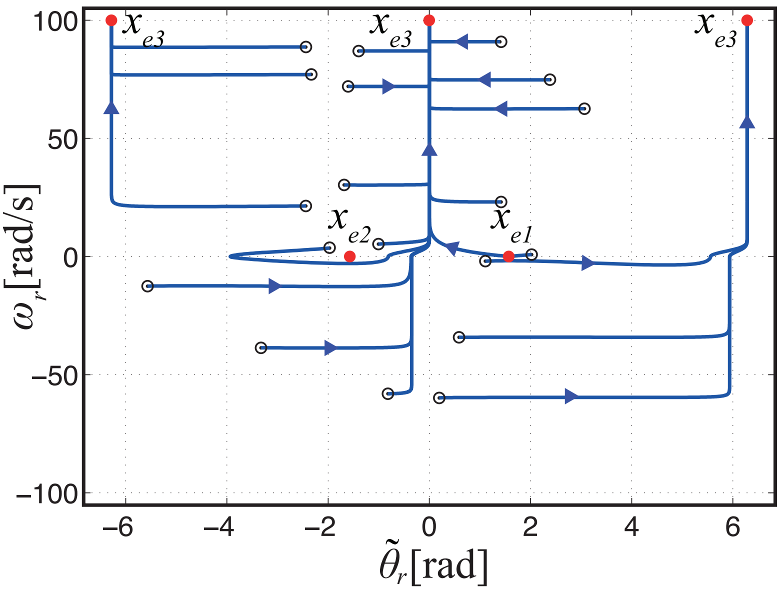

Figure 4.8: Phase portrait of the closed loop non-linear system with the globally converging estimator for $b = 2$ and $\zeta = 0.75$

4.3 Results of simulations

The globally converging algorithm is now evaluated through simulation assuming that there are no parameters uncertainties. Measurement noise is introduced in the currents by adding to each current 1% of the phase current value multiplied by a random generated white noise. The parameters used in all the simulations are the ones from the experimental system described in 7.

The estimator parameter are the ones used also for the numerical analysis.

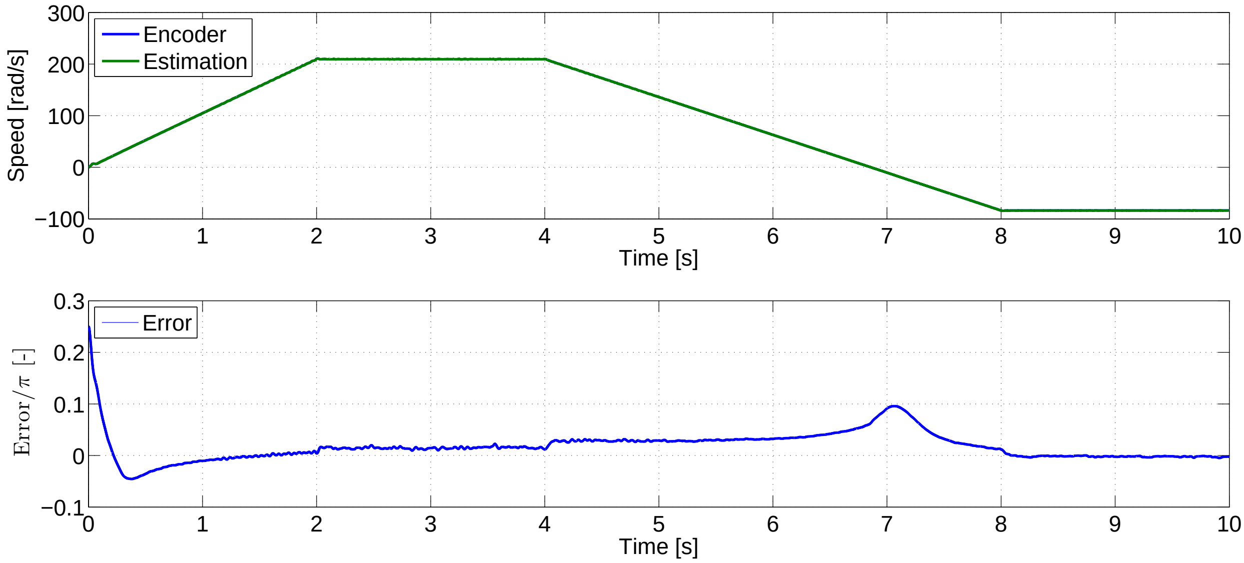

Figure 4.9: Simulation results for a start with $\frac{\pi}{4}$ initial position error at no load condition

The results of the simulation at no load condition is shown in Fig. 4.9. It is possible to notice how the estimator converges to zero position error from the initial condition. The position error is then only slightly influenced by the transients with the maximum perturbation at the moment of speed reversal.

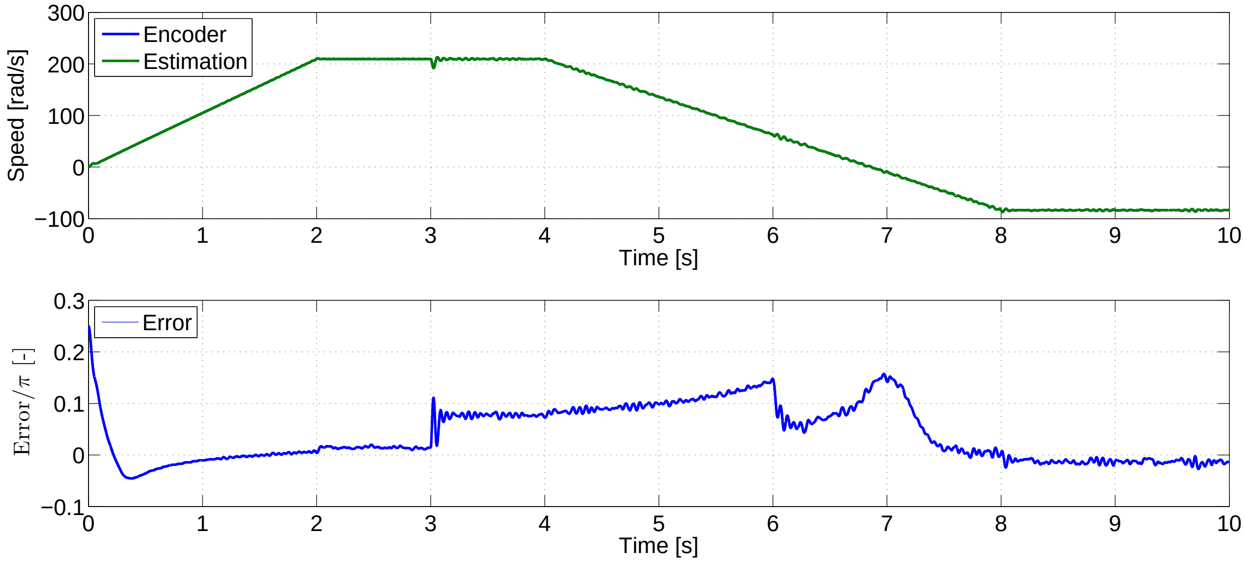

Figure 4.10: Simulation results for a start with $\frac{\pi}{4}$ initial position error and load torque pulsation at 3s

The results with load torque pulsation show a similar behaviour with the obvious influence of the torque pulsation which is reflected on the error. In steady state the estimator is anyway able to converge to the desired equilibrium.

Parameters uncertainties and Online Estimation of stator resistance 5

5.1 Robustness analysis and effects of parameters uncertainties

The robustness of the second Matsui method is discussed analysing the effects of parameters uncertainties on the stability and the solutions of the position estimator described in the previous section.

In the following it will be considered the simplified case of an SPMSM, i.e. $L_\mathrm{d} = L_\mathrm{q} = L_\mathrm{s}$. The effects of parameters uncertainties on the current model estimator for salient machines are analysed in [Nahid-Mobarakeh et al., 2001], using a machine model similar to the one outlined in Eq. 4.2-4.3.

The parameters errors are defined as follows:

$$\tilde{R_\mathrm{s}} = \hat{R_\mathrm{s}} - R_\mathrm{s} \tag{5.1}$$

$$\tilde{L_\mathrm{s}} = \hat{L_\mathrm{s}} - L_\mathrm{s} \tag{5.2}$$

$$\bar{\psi_\mathrm{pm}} = \frac{\hat{\psi_\mathrm{pm}}}{\psi_\mathrm{pm}} \tag{5.3}$$

Assuming that the parameters used in the estimator model are different from the actual ones, the expressions of the current errors in Eq. 4.15 and 4.16 change into Eq. 5.4 and 5.5

$$\frac{L_\mathrm{s}}{T_\mathrm{s}}\tilde{i_\delta} = \omega_\mathrm{r}\psi_\mathrm{pm}\sin\tilde{\theta}_\mathrm{r} + \tilde{L_\mathrm{s}}i_\gamma\hat{\omega_\mathrm{r}} - \tilde{R_\mathrm{s}}i_\delta \tag{5.4}$$

$$\frac{L_\mathrm{s}}{T_\mathrm{s}}\tilde{i_\gamma} = \omega_\mathrm{r}\psi_\mathrm{pm}\cos\tilde{\theta}_\mathrm{r} - \psi_\mathrm{pm}\hat{\omega_\mathrm{b}} - \tilde{L_\mathrm{s}}i_\delta\hat{\omega_\mathrm{r}} - \tilde{R_\mathrm{s}}i_\gamma \tag{5.5}$$

$$\hat{\omega_\mathrm{r}} = \frac{1}{\hat{\psi_\mathrm{pm}}}\frac{L_\mathrm{s}}{T_\mathrm{s}}\tilde{i_\gamma} + \beta\frac{L_\mathrm{s}}{T_\mathrm{s}}\tilde{i_\delta} \tag{5.6}$$

Substituting Eq. 5.4 and 5.5 into 5.6 yields

$$\hat{\omega_{\mathrm{r}}} = \frac{1}{\hat{\psi_{\mathrm{pm}}}} \left(\omega_{\mathrm{r}} \psi_{\mathrm{pm}} \cos \theta_{\mathrm{r}} - \tilde{R_{\mathrm{s}}} i_{\gamma} + \beta \hat{\psi_{\mathrm{pm}}} \omega_{\mathrm{r}} \psi_{\mathrm{pm}} \sin \tilde{\theta_{\mathrm{r}}} \right) + \frac{1}{\hat{\psi_{\mathrm{pm}}}} \hat{\omega_{\mathrm{r}}} \left(\beta \hat{\psi_{\mathrm{pm}}} \tilde{L_{\mathrm{s}}} i_{\gamma} \right) \tag{5.7}$$

Through simple manipulations, an expression for the estimated speed as function of the parameters uncertainties is found

$$\hat{\omega_{\mathrm{r}}} = \frac{\omega_{\mathrm{r}} \left(\cos \tilde{\theta_{\mathrm{r}}} + \beta \hat{\psi_{\mathrm{pm}}} \sin \tilde{\theta_{\mathrm{r}}} \right) - \frac{\tilde{R_{\mathrm{s}}} i_{\gamma}}{\psi_{\mathrm{pm}}}}{\frac{\hat{\psi_{\mathrm{pm}}}}{\psi_{\mathrm{pm}}} - \beta \hat{\psi_{\mathrm{pm}}} \frac{\tilde{L_{\mathrm{s}}} i_{\gamma}}{\psi_{\mathrm{pm}}}} \tag{5.8}$$

Remembering from Eq. 4.32 that $\frac{\tilde{\theta_{\mathrm{r4}}}}{2} = \arctan(\beta \hat{\psi_{\mathrm{pm}}})$ for convenience it is defined that $\arctan(-\beta \hat{\psi_{\mathrm{pm}}}) = \rho$. In addition the following positions are defined for the terms which depend on the parameters uncertainties

$$\frac{\tilde{R_{\mathrm{s}}} i_{\gamma}}{\psi_{\mathrm{pm}}} = h_{\mathrm{R}} \tag{5.9}$$

$$\frac{\tilde{L_{\mathrm{s}}} i_{\gamma}}{\psi_{\mathrm{pm}}} = D_{\mathrm{L}} \tag{5.10}$$

With all the previous considerations, the perturbed expression for the estimated speed is obtained in few steps

$$\begin{aligned} \hat{\omega_{\mathrm{r}}} &= \frac{\omega_{\mathrm{r}} \left(\cos \tilde{\theta_{\mathrm{r}}} - \frac{\sin \rho}{\cos \rho} \sin \tilde{\theta_{\mathrm{r}}} \right) - h_{\mathrm{R}}}{\bar{\psi_{\mathrm{pm}}} + D_{\mathrm{L}} \frac{\sin \rho}{\cos \rho}} \\ &= \frac{\omega_{\mathrm{r}} \left(\cos \rho \cos \tilde{\theta_{\mathrm{r}}} - \sin \rho \sin \tilde{\theta_{\mathrm{r}}} \right) - h_{\mathrm{R}} \cos \rho}{\bar{\psi_{\mathrm{pm}}} \cos \rho + D_{\mathrm{L}} \sin \rho} \\ &= \frac{\omega_{\mathrm{r}} \cos \left(\tilde{\theta_{\mathrm{r}}} + \rho \right) - h_{\mathrm{R}} \cos \rho}{\bar{\psi_{\mathrm{pm}}} \cos \rho + D_{\mathrm{L}} \sin \rho} \end{aligned} \tag{5.11}$$

The expression for the estimated speed is substituted in the system of Eq. 4.24, in order to evaluate the effects of parameters uncertainties on the closed loop system

$$\begin{cases} \frac{d\tilde{\theta_{\mathrm{r}}}}{dt} &= \frac{\omega_{\mathrm{r}} \left(\cos(\tilde{\theta_{\mathrm{r}}} + \rho) - \bar{\psi_{\mathrm{pm}}} \cos \rho - D_{\mathrm{L}} \sin \rho \right) - h_{\mathrm{R}} \cos \rho}{\bar{\psi_{\mathrm{pm}}} \cos \rho + D_{\mathrm{L}} \sin \rho} \\ \frac{J}{p} \frac{d\omega_{\mathrm{r}}}{dt} &= \frac{3}{2} p \, \psi_{\mathrm{pm}} i_{\gamma} \cos \tilde{\theta_{\mathrm{r}}} - T_{\mathrm{L}}\left(\frac{\omega_{\mathrm{r}}}{p} \right) \end{cases} \tag{5.12}$$

5.1.1 Uncertainty on the inductance

There is often an uncertainty on the inductance parameter, mainly due to the non-linear phenomenon of magnetic saturation and the non-perfect isotropy of any practical machine. In this case only the uncertainty on the inductance is considered, so $\tilde{R_{\mathrm{s}}} = 0$ and $\bar{\psi_{\mathrm{pm}}} = 1$. Eq. 5.12 becomes

$$\frac{d\tilde{\theta_{\mathrm{r}}}}{dt} = \frac{\omega_{\mathrm{r}} \left(\cos(\tilde{\theta_{\mathrm{r}}} + \rho) - \cos \rho - D_{\mathrm{L}} \sin \rho \right)}{\cos \rho + D_{\mathrm{L}} \sin \rho} \tag{5.13}$$

The presence of the uncertainties terms will move the system equilibrium previously found for the ideal case. $\tilde{\theta}_{\mathrm{r}} = 0$ will not be any more a solution for the equilibrium equation 5.13, so also the desired equlibrium will present a position error.

The simulation results of the estimator with a +50% Inductance uncertainty are shown in Fig. 5.5.

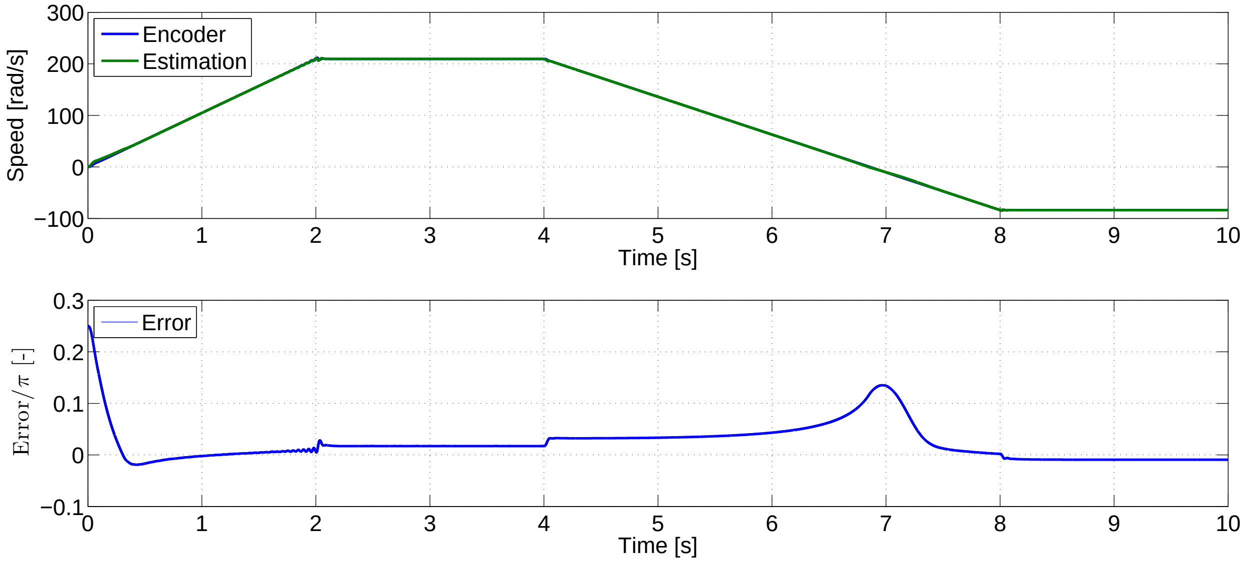

Figure 5.1: Simulation results for a start with $\frac{\pi}{4}$ initial position error and uncertainty on the inductance parameter of $\tilde{L}_{\mathrm{s}} = 0.5\ L_{\mathrm{s}}$

As it is possible to see from the plot of position error, the desired equilibrium presents now a deviation from the ideal case with zero position error. Indeed also in steady state the position error is slightly different from zero.

5.1.2 Uncertainty on rotor permanent magnet flux linkage

In this case only the uncertainty due to the rotor permanent magnet flux linkage parameter is considered, thus $\bar{\psi}_{\mathrm{pm}} \neq 1$ and $\tilde{R}_{\mathrm{s}} = 0, \tilde{L}_{\mathrm{s}} = 0$ The following expression for the error dynamics follows from Eq. 5.12:

$$\frac{d\tilde{\theta}_{\mathrm{r}}}{dt} = \frac{\omega_{\mathrm{r}}(\cos(\tilde{\theta}_{\mathrm{r}} + \rho) - \bar{\psi}_{\mathrm{pm}} \cos \rho)}{\bar{\psi}_{\mathrm{pm}} \cos \rho} \tag{5.14}$$

As in the previous case the term $\bar{\psi}_{\mathrm{pm}}$ will cause a shift between the ideal desired equilibrium and the practical one due to the uncertainty. It is possible to notice that, differently from the other parameters uncertainties, the one due to the permanent magnet flux does not depend on the torque producing current. A similar consideration was made also in [Eskola, 2006].

The simulation results of the estimator with a +10% Inductance uncertainty are shown in Fig. 5.2.

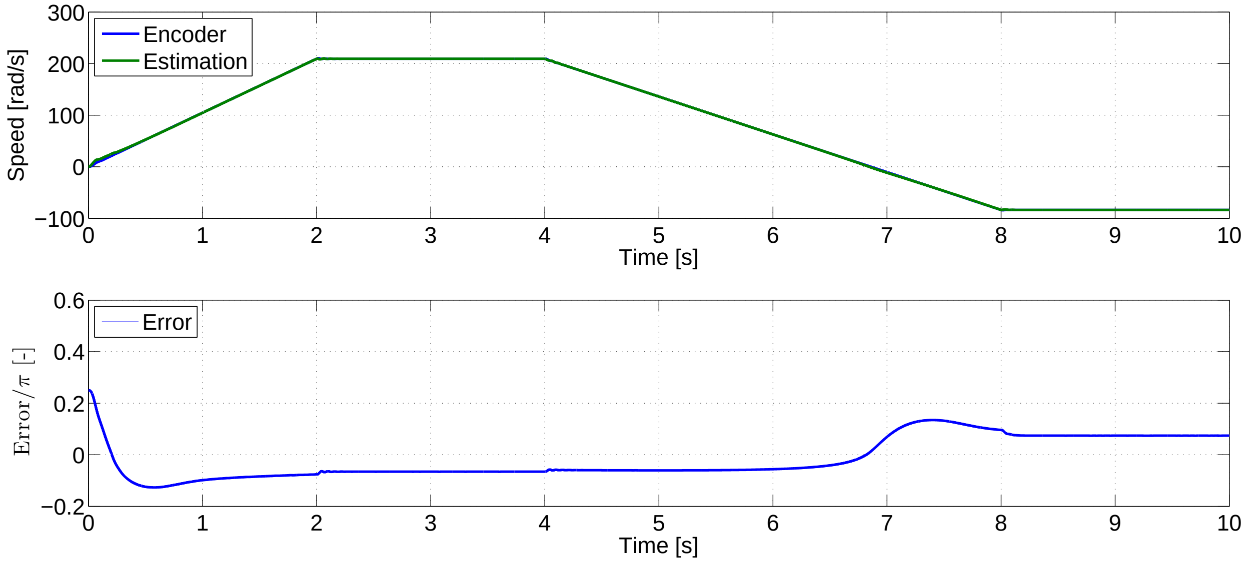

Figure 5.2: Simulation results for a start with $\frac{\pi}{4}$ initial position error and uncertainty on the permanent magnet flux parameter of $\tilde{\bar{\psi}}_{\mathrm{pm}} = 1.1$

The plot shows that the uncertainty due to the permanent magnet flux is more significant during steady state with regards to the the transients and to the inductance case. Only 10% error can cause an error of 0.1π. The relative low sensitivity during transient, especially during the speed reversal, confirms the analytical consideration of the uncertainty not being dependent on the torque producing current.

5.1.3 Uncertainty on Stator resistance

In this case only the uncertainty due to the rotor permanent magnet flux linkage parameter is considered, thus $\tilde{R}_{\mathrm{s}} \neq 0$ and $\bar{\psi}_{\mathrm{pm}} = 1, \tilde{L}_{\mathrm{s}} = 0$ The following expression for the error dynamics follows from Eq. 5.12:

$$\begin{cases} \frac{d\tilde{\theta}_{\mathrm{r}}}{dt} &= \frac{\omega_{\mathrm{r}}(\cos(\tilde{\theta}_{\mathrm{r}}+\rho)-\cos\rho)-h_{\mathrm{R}}\cos\rho}{\cos\rho} \\ \frac{J}{p}\frac{d\omega_{\mathrm{r}}}{dt} &= \frac{3}{2}p\,\psi_{\mathrm{pm}} i_{\gamma}\cos\tilde{\theta}_{\mathrm{r}} - T_{\mathrm{L}}(\frac{\omega_{\mathrm{r}}}{p}) \end{cases} \tag{5.15}$$

In this case both the equations of the closed-loop non-linear system are reported. The Resistance mismatch will still cause a shift from the desired ideal equilibrium, even dependent on the load current, but differently from the other cases, the presence of the uncertainty due to the stator resistance, the term h_{R}, may cause an interesting non-linear phenomenon. In the previous cases the dynamics of the error were purely function of a combination of trigonometric functions. More specifically they allow for a solution, meaning that the system will eventually end in an equilibrium.
In this case instead, the additional term h_{R} may be always larger in absolute value than the other term. This will keep the derivative of the position error of the same sign, thus discarding any possibility of an equilibrium. Considering the mechanical equation of the closed loop system in Eq. 5.13, it is possible to understand that also the speed will be oscillating. The trajectory of the system will then be a limit cycle on the phase plane, making the system only marginally stable with undesired oscillations.

The simulation results of the estimator with a +200% Stator Resistance uncertainty are shown in Fig. 5.2.

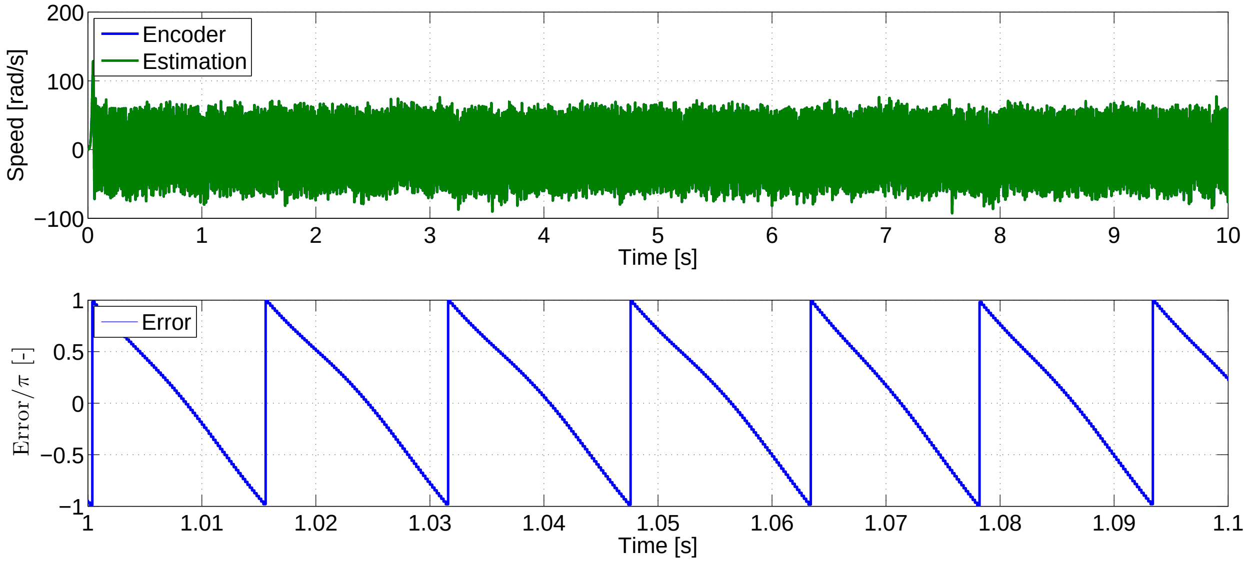

Figure 5.3: Simulation results for a start with $\frac{\pi}{4}$ initial position error and uncertainty on the stator resistance parameter of $\tilde{R}_s = 200\% R_s$

It is possible to notice the expected behaviour with the speed oscillating around zero and the detail of the error showing the continue progression in the same direction.

[Nahid-Mobarakeh et al., 2001] analyses more in detail this particular phenomenon, finding also a condition on the uncertainty for avoiding it to happen. The whole point of this analysis is to find the importance of reducing the error of the stator resistance which could be fatal to the sensorless control algorithm.

5.2 Online estimation of stator resistance

The principle of Model Reference Adaptive control is depicted in Fig. 5.4. The idea is to run in real time a simulation of the controlled process and adapt one or more parameters in order to reduce and bring to zero the error between the measured quantity and the estimated one. Also the Second Matsui method, described in the previous chapter, can be considered an MRAS approach to the estimation of the back-EMF components.

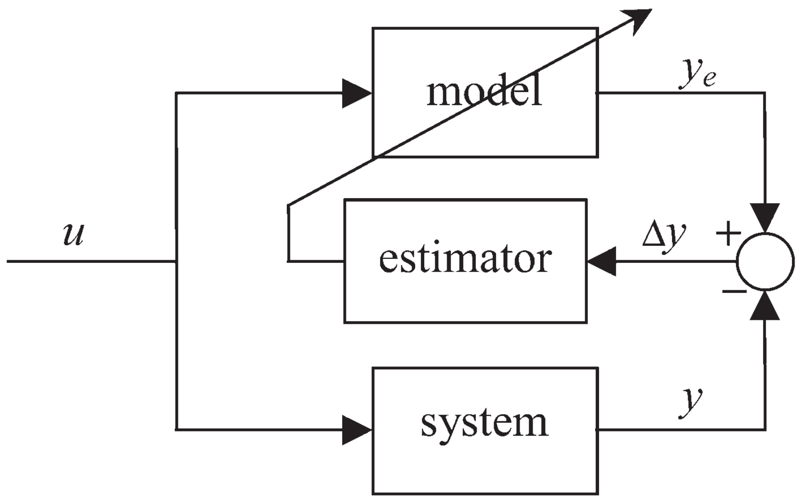

Figure 5.4: Block diagram of the principle of MRAS [Nahid-Mobarakeh et al., 2004]

The idea of augmenting with an additional state an observer in order to estimate an additional parameter belongs to many advanced control technique such as Kalman Filter. As mentioned in chap. 1, the derivation of stability criteria for these kinds of augmented non-linear observer might be quite complicated. MRAS can be an easier approach.

In the same reference of the globally converging estimator, [Nahid-Mobarakeh et al., 2004], a simpler MRAS estimation technique for the stator resistance is outlined. The current on the γ-axis is estimated through a real-time calculation of the γ-axis equation as reported in Eq. 5.16, while the value of the estimated resistance is adjusted as in Eq. 5.17 through a static gain and the current estimation error.

$$L\frac{d}{dt}\hat{i_{\gamma\mathrm{R}}} = -\hat{R_{\mathrm{se}}}\hat{i_{\gamma\mathrm{R}}} - L\hat{\omega}_{\mathrm{r}} i_\delta - \hat{\psi_{\mathrm{pm}}} + v_\gamma \tag{5.16}$$

$$\frac{d}{dt}\tilde{R_{\mathrm{se}}} = -\eta(\hat{i_{\gamma\mathrm{R}}} - i_\gamma) \tag{5.17}$$

Referring to Fig. 5.4, Eq. 5.16 is the model, while Eq. 5.17 is the estimator.

The stability and convergence condition for the closed loop system augmented with the state $\tilde{R_{\mathrm{se}}}$ is found to be as in Eq. 5.18 [Nahid-Mobarakeh et al., 2004]. With this conditions the state $\tilde{R_{\mathrm{se}}} = 0$ is a stable equilibrium.

$$\begin{aligned} b &> 0 \\ \eta \cdot i_\gamma &< 0 \end{aligned} \tag{5.18}$$

The performances of the system augmented with the resistance estimator are evaluated through simulation.

The machine's stator resistance is stepped up at the istant $t = 12$ in the machine model by 25% of its value.

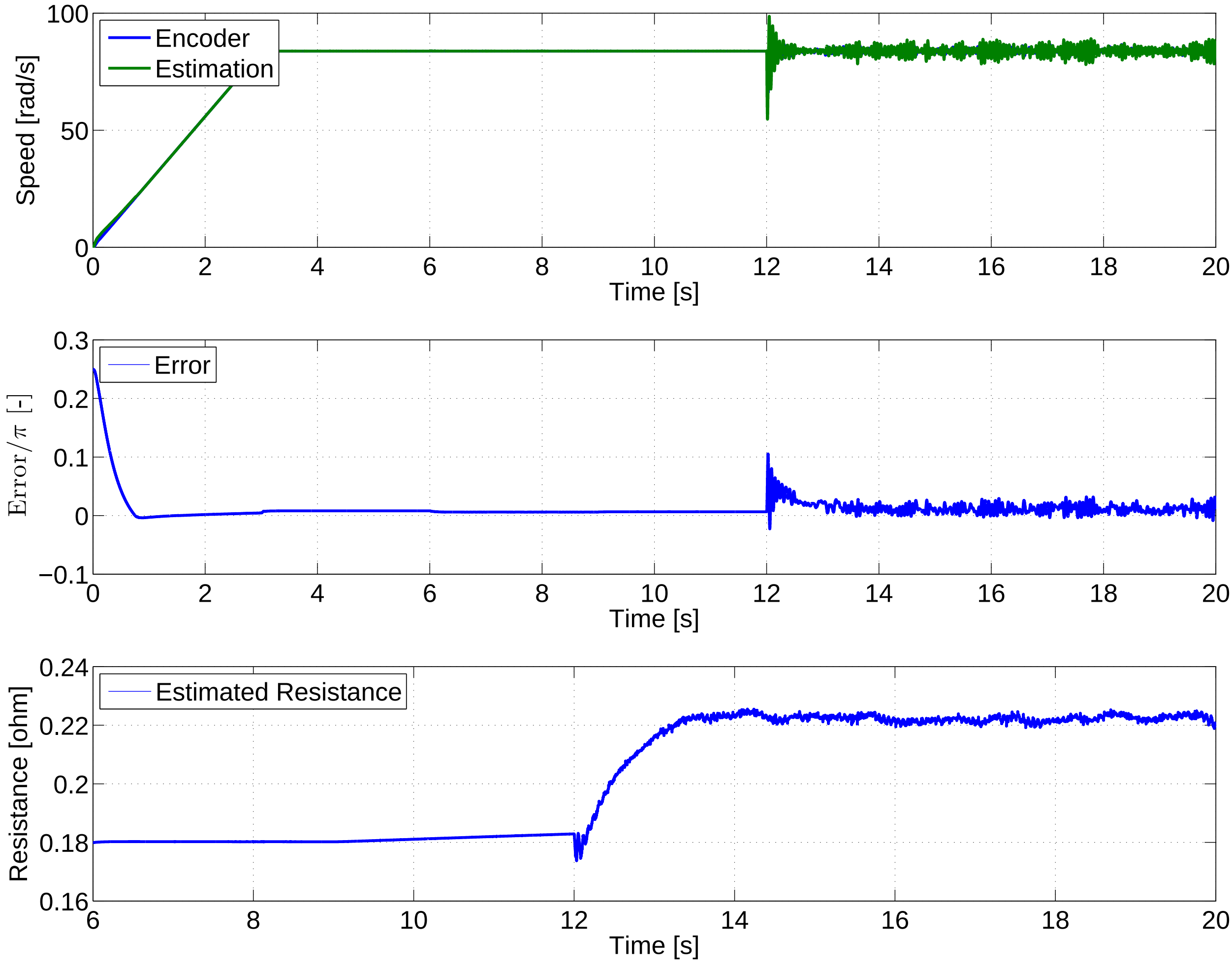

Figure 5.5: Simulation results for a sudden step up in stator Resistance equal to $25\%R_s$

The estimator is able to track the changes in the resistance and to bring the error to 0.

6 Voltage Compensation for Inverter non-linearities

6.1 Losses characterisation

As mentioned in chap. 2, the switching devices of the voltage source inverter present a commutation delay every time the gate signal is commuted. This delay is known with the name of *dead time*, during which both the two devices on the same leg are disconnected from the voltage source. If the two devices on the same leg are conducting at the same time, the DC voltage source will be shorted, generating a large current flowing through the converter and the load. This kind of fault is known with the name of *shoot through fault*. An ideal converter with ideal devices would use two perfectly complementary signals to control the gates of the two switching devices on the same leg. Considering a practical converter with practical switch devices, the switches will commute after a certain amount of time due to the transients of the switching devices. Here comes the need for a time delay which has to be significantly larger than these on/off transitions times, in order to keep a reasonable safety margin.

From this consideration it can be intuitively inferred that the voltage drop in the inverter is mostly due to the dead time rather than to the commutation time. The voltage drop will now be analysed through quantitative considerations starting from the topology of the single leg of the converter, reported in Fig. 6.1. Once the voltage drops are defined, a method for compensating them will be outlined.

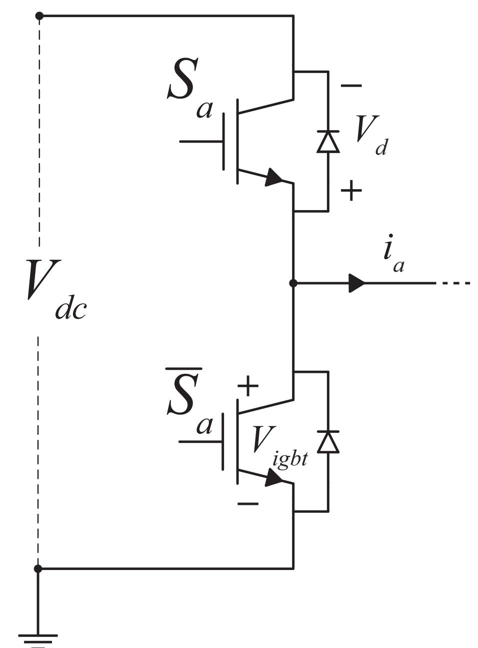

Figure 6.1: Topology of one leg of the Voltage Source Inverter

In the figure V_{igbt} is the forward voltage of the inverter's IGBTs, while V_{d} is the one relative to the free-wheeling diode. In the following v_{aN} will refer to the voltage on the leg a of the converter referred to the negative of the DC-Link. According to the sign of the current in the phase-load connection and the signal which controls the switch, the converter leg topology may translate into 4 different conduction paths which will determine the voltage output on the leg terminal, as shown in Fig. 6.2.

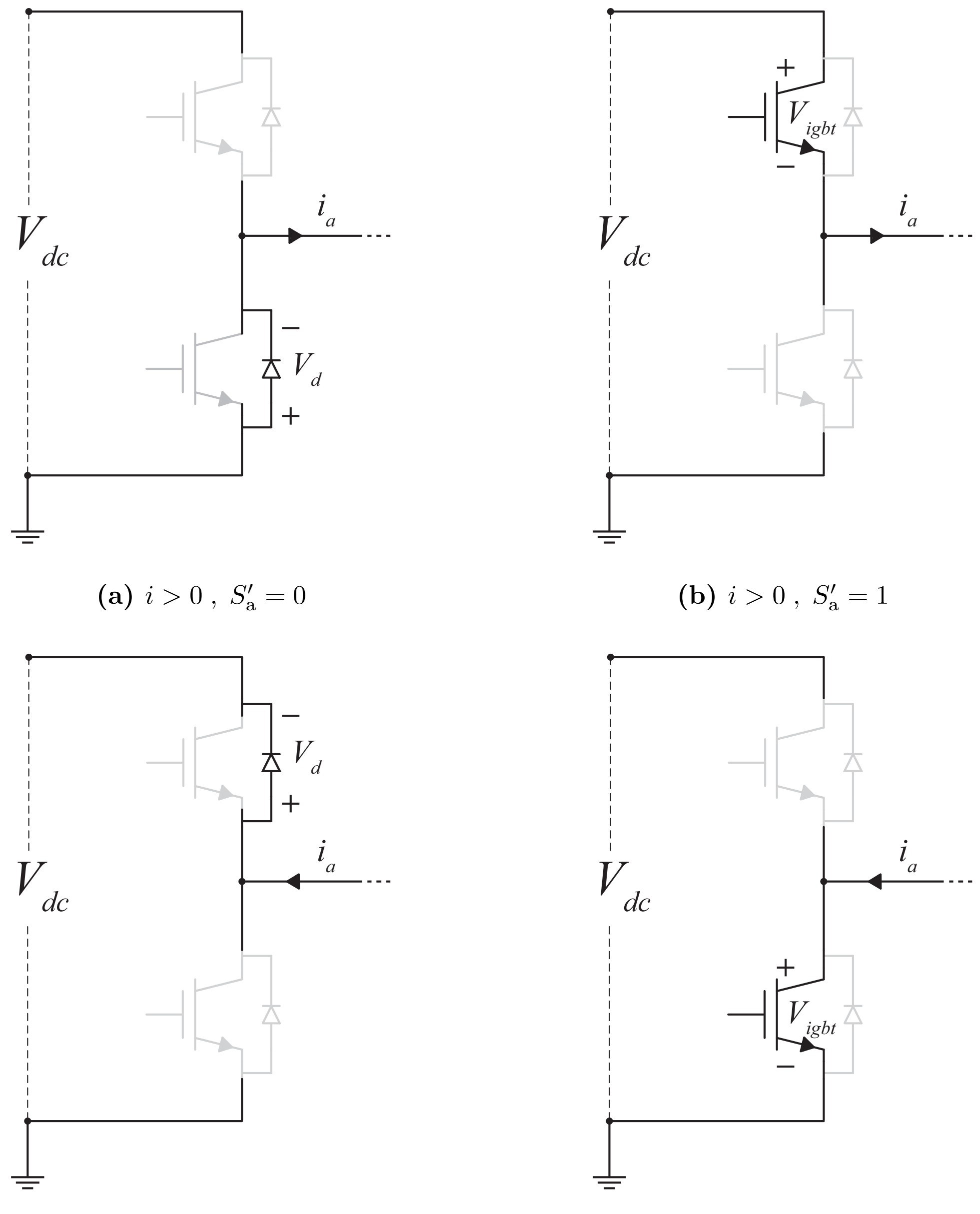

(a) $i > 0\ ,\ S'_{\mathrm{a}} = 0$ **(b)** $i > 0\ ,\ S'_{\mathrm{a}} = 1$

(c) $i < 0\ ,\ \bar{S}'_{\mathrm{a}} = 0$ **(d)** $i < 0\ ,\ \bar{S}'_{\mathrm{a}} = 1$

Figure 6.2: Conduction paths of the single leg of the Voltage Source Inverter according to the sign of the current and the gate signals

Fig. 6.2a and 6.2b show the paths which are conducting during dead time. When both the gate signals are negative during dead time, the lower or the upper free-wheeling diode is conducting, according to the current being respectively positive or negative. It must be noted that the active diodes keep conducting also after the gate signals of the parallel switch go high, so in these cases the forward voltage seen on the leg will be the one of the diodes.

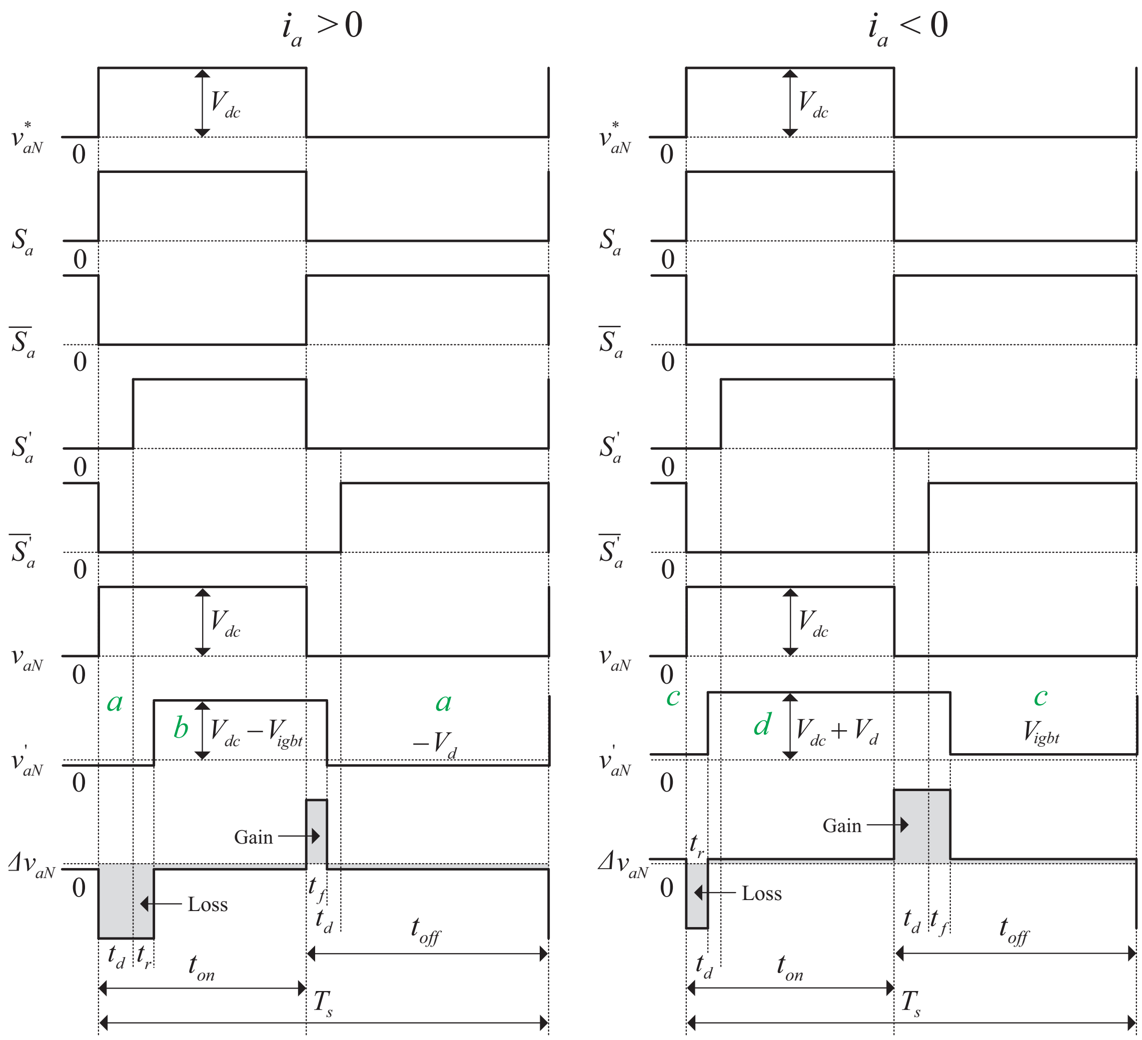

Figure 6.3: Voltage losses for a practical switching device [Krishnan, 2010]

The transitions between the conducting paths and the voltage drops are represented for one switching period in Fig. 6.3. The representation includes the dead time t_d and the turn on/off transient times (rise time t_r and fall time t_f).

The difference between the desired voltage to be output on the leg and the actual one obtained after the drops is also represented in the figure. The integral of the voltage drops against the switching time is the actual average voltage loss which is not delivered as intended through the modulation. The average voltage loss is calculated considering the area of the rectangles of the voltage difference between ideal and practical output.

$$\Delta v_\mathrm{aN} = \begin{cases} \frac{t_\mathrm{f} - t_\mathrm{d} - t_\mathrm{r}}{T_\mathrm{s}} (V_\mathrm{dc} - V_\mathrm{igbt} + V_\mathrm{d}) + \frac{-t_\mathrm{off}}{T_\mathrm{s}} V_\mathrm{d} + \frac{t_\mathrm{off} - T_\mathrm{s}}{T_\mathrm{s}} V_\mathrm{igbt} & i_\mathrm{a} > 0 \\ \frac{t_\mathrm{f} + t_\mathrm{d} - t_\mathrm{r}}{T_\mathrm{s}} (V_\mathrm{dc} - V_\mathrm{igbt} + V_\mathrm{d}) + \frac{T_\mathrm{s} - t_\mathrm{off}}{T_\mathrm{s}} V_\mathrm{d} + \frac{t_\mathrm{off}}{T_\mathrm{s}} V_\mathrm{igbt} & i_\mathrm{a} < 0 \end{cases} \tag{6.1}$$

From Eq. 6.1 it is possible to evaluate the contribute of each parameter to the average voltage loss. The first term depends exclusively on the physical characteristics of the devices, while the other two terms depend also on the operational conditions, namely the duty cycle. For lower duty cycles the weight of the losses related to the output voltage is higher than for greater duty cycles. This means that for higher output voltages the average voltage loss in the switching period is not as significant as for lower output voltages.

The parameters which depend on the physical characteristics of the devices are not constant and vary with temperature and load current. This means that a precise compensation for all the losses is not possible due to the complexity of modelling the physical characteristics. In practice the voltage drop due to the dead time is significantly more consistent than the one due to the on/off transition times. The requirement of using a dead time which is significantly larger that the transition times for safety reasons allows for the assumption of neglecting the voltage drops due to the transition times.

6.2 Compensation Strategy

With the average voltage losses defined for both positive and negative currents as in Eq. 6.1, it is possible to determine a compensation strategy.

The adopted compensation method is used in several examples in the literature for motor drives, and also for sensorless applications as in [Inoue et al., 2009]

The idea is to compensate in each leg the reference voltages fed to the modulation algorithm, for the losses identified in Eq. 6.1 according to the sign of the phase current. This is done by adding an additional term to the reference as expressed in Eq. 6.2

$$\begin{bmatrix} v_{\mathrm{aN}}{}^{*} \\ v_{\mathrm{bN}}{}^{*} \\ v_{\mathrm{cN}}{}^{*} \end{bmatrix} = \begin{bmatrix} v_{\mathrm{aN}} \\ v_{\mathrm{bN}} \\ v_{\mathrm{cN}} \end{bmatrix} - \Delta v_{\mathrm{jN}} \begin{bmatrix} f(i_{\mathrm{a}}) \\ f(i_{\mathrm{b}}) \\ f(i_{\mathrm{c}}) \end{bmatrix} \tag{6.2}$$

The correction term Δv_{jn} is obtained on the basis of the considerations made on the average losses. The voltage drop due to devices transients is neglected and the forward voltage drop is evaluated for an average 0.5 duty cycle.

$$\Delta v_{\mathrm{jn}} = \begin{cases} \frac{-t_{\mathrm{d}}}{T_{\mathrm{s}}}(V_{\mathrm{dc}} - V_{\mathrm{igbt}} + V_{\mathrm{d}}) - \frac{V_{\mathrm{igbt}}+V_{\mathrm{d}}}{2} & i_{\mathrm{j}} > 0 \\ \frac{+t_{\mathrm{d}}}{T_{\mathrm{s}}}(V_{\mathrm{dc}} - V_{\mathrm{igbt}} + V_{\mathrm{d}}) + \frac{V_{\mathrm{igbt}}+V_{\mathrm{d}}}{2} & i_{\mathrm{j}} < 0 \end{cases} \tag{6.3}$$

There are now two possibilities for what concerns the transition between positive and negative currents. One approach would be to keep the discontinuity of the definition, using a sign function for selecting the correction term. The preferred approach is instead to use a smoother function in the proximity of 0, so that the correction factor can be closer to the actual losses at a lower current (load), especially in light of the choice of approximating the losses to the theoretical case of average duty cycle. The two approaches are represented in Fig. 6.4 and Eq. 6.4-6.5

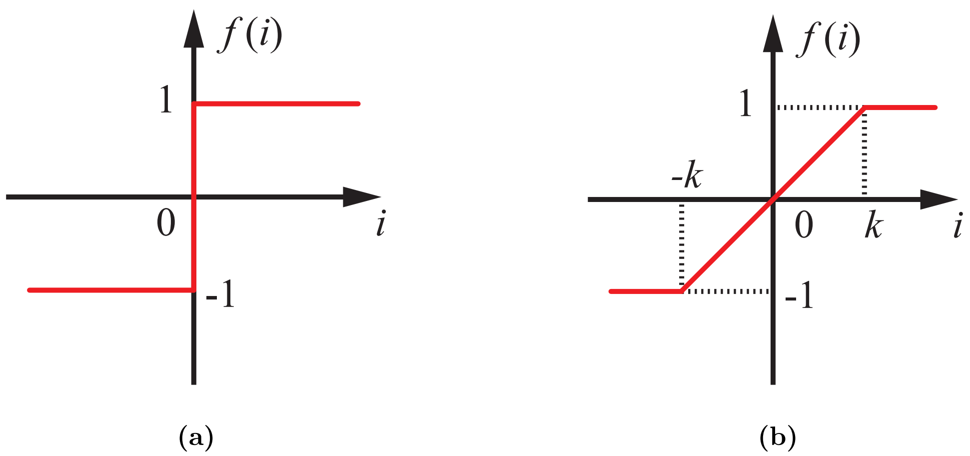

Figure 6.4: Diagram of the two possible $f(i)$ [Inoue et al., 2009]

$$\text{Approach a:} \quad f(i) = \operatorname{sgn}(i) \tag{6.4}$$

$$\text{Approach b:} \quad f(i) = \begin{cases} \frac{1}{k} \cdot i & i < |k| \\ \operatorname{sgn}(i) & i \geq |k| \end{cases} \tag{6.5}$$

The parameter k is arbitrarily chosen equal to $0.5A$.

7 Experimental Results

In this chapter an experimental evaluation of the sensorless control algorithm is performed. The position and the speed are measured additionally through an encoder so that the results can be compared with the ones obtained with the sensorless control algorithm. First the experimental system on which the experiments were performed is described, then the algorithm is tested through few simple tests.

7.1 Experimental system

The experimental system used in this thesis is one of the available set-ups of the Flexible Drive System Laboratory of the Energy Technology Department at Aalborg University. It features a dSPACE DS1103 microcontroller system, configured to control at the same time a PMSM and an IM drive system. In this configuration the PMSM and the IM are mounted on the same shaft and the latter is used to act as a mechanical load for the PMSM.

The set-up is shown in Fig. 7.1 , while its schematic diagram is shown in Fig. 7.2. The technical spcecifications are shown in Tab. 7.1.

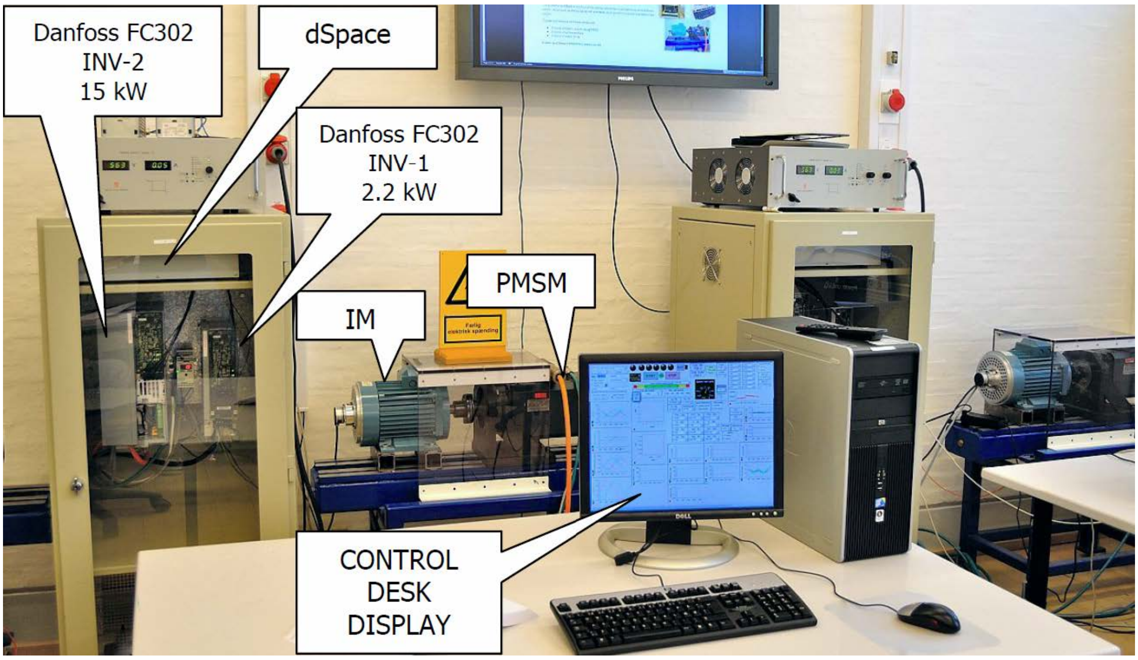

Figure 7.1: The experimental set-up used in this thesis [AAU E.T. Department, 2014]

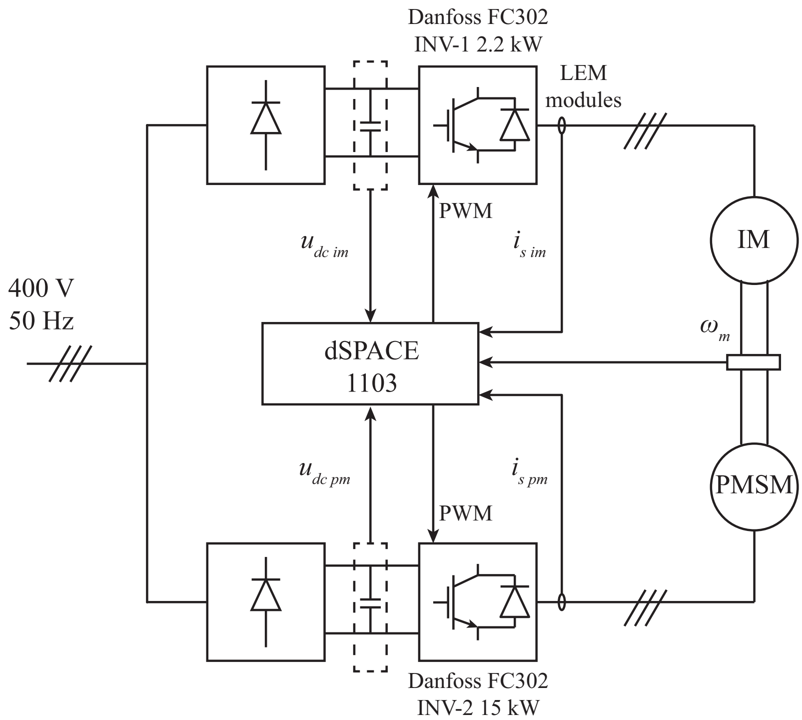

Figure 7.2: Schematic diagram of the experimental set-up

Siemens PMSM ROTEC 1FT6084-8SH7		
Rated speed	n	4500 rpm
Number of pole pairs	p	4
Rated torque	M_{n}	20 Nm
Rated power	P_{n}	24.5 A
Torque constant	K_{T}	1.01 Nm/A
Winding Resistance	R_{s}	0.19 Ω
Field Inductance	L_{s}	2.2 mH
Magnetic Flux	ψ_{pm}	0.123 Wb
Danfoss FC302 VSI 15 kW		
Rated input voltage	V_{in}	$380 - 500$ V
Rated output voltage	V_{out}	$0 - 500$ V
Rated input current	I_{in}	29 A
Rated output current	I_{out}	32 A
Dead Time	t_{d}	2.5 μs
Switching Frequency	f_{s}	5 kHz
Output voltage frequency	f_{out}	$0 - 1000$ Hz
Mechanical system		
Drive shaft Inertia	J_{m}	0.0146 kg $\cdot$ m^2
Viscous Damping	f_{v}	0.00167 Ns/m
dSPACE 1103		
Sampling and Update frequency	f_{s}	5 kHz

Table 7.1: Technical specifications of the experimental system

As it is possible to see in Fig. 7.2, the AC machines are supplied through two Danfoss 2-levels FC302 Voltage Source Inverters. Both two inverters are controlled by the same dSPACE 1103 unit. dSPACE 1103 is a mixed RISC/DSP digital microcontroller, capable of running real-time control application thanks to its powerful floating point processor, able to handle at the same time all the I/O communications. The dSPACE system includes a code-generation tool able to program the unit from Matlab/Simulink models, and the Control Desk environment which allows the real-time supervision of the experiments through virtual instruments and scopes. The set-up features an SPMSM which is consistent with the simplification assumptions made in the derivation of the sensorless control algorithm. The parameters for the set-up were partially obtained experimentally and partially obtained from previous publications based on the same set-up as [Basar et al., 2014].

The parameters used in the experiments are listed in Tab. 7.2.

Field Oriented Control		
Current Proportional Gain	K_p	1.79 [-]
Current Integral Gain	K_i	147.7 [-]
Speed Proportional Gain	$K_{\mathrm{p}\omega}$	1.41 [-]
Speed Integral Gain	$K_{\mathrm{i}\omega}$	46.1 [-]
D-axis current reference	${i_\mathrm{d}}^*$	2 A
Variable Structure Estimator		
Auxiliary speed filter gain	α	7.3 [-]
Estimated speed correction gain	b	2 [-]
Variable structure estimator gain	ζ	0.75 [-]

Table 7.2: Settings of the parameters used in the experiments

It must be noted that during the experiments the current reference for the d-axis is set to a value different than 0. Even though this is not the current command which gives the most torque per current density for a SPMSM, it is common to see in practical applications of sensorless control methods an injection of current in the d-axis, up to 10-15% of rated current. Experiments have shown that this expedient reduces considerably ripples in speed and position estimation. [Calligaro and Petrella, 2012] proposes an analysis of the phenomenon concluding that the injection of a current in the d-axis can produce a damping effect on the estimation noise.

7.2 No load test

In this test, the sensorless algorithm is tested at no load, the machine is started from stand still and accelerated through incrementing speed step commands. Once the machine has reached through several steps the speed of 600 rpm, the test continues decelerating the machine until it performs a speed reversal and runs at negative speeds. The parameters for the controller and the estimator are the ones discussed in the previous chapters.

7.2.1 Start and incremental speed steps

In the graphs in Fig. 7.3, it can be seen how the machine is starting from stand still until it reaches 600 rpm through several steps of different amplitude. A good response in both steady and dynamic states is noticeable. The i_d current follows the reference given, while, on the other hand i_q differs from zero during mechanical transients. When there are changes in speed due to inertia, peaks in the i_q values appear. The graph of the Torque is shown in order to verify that there is no load.

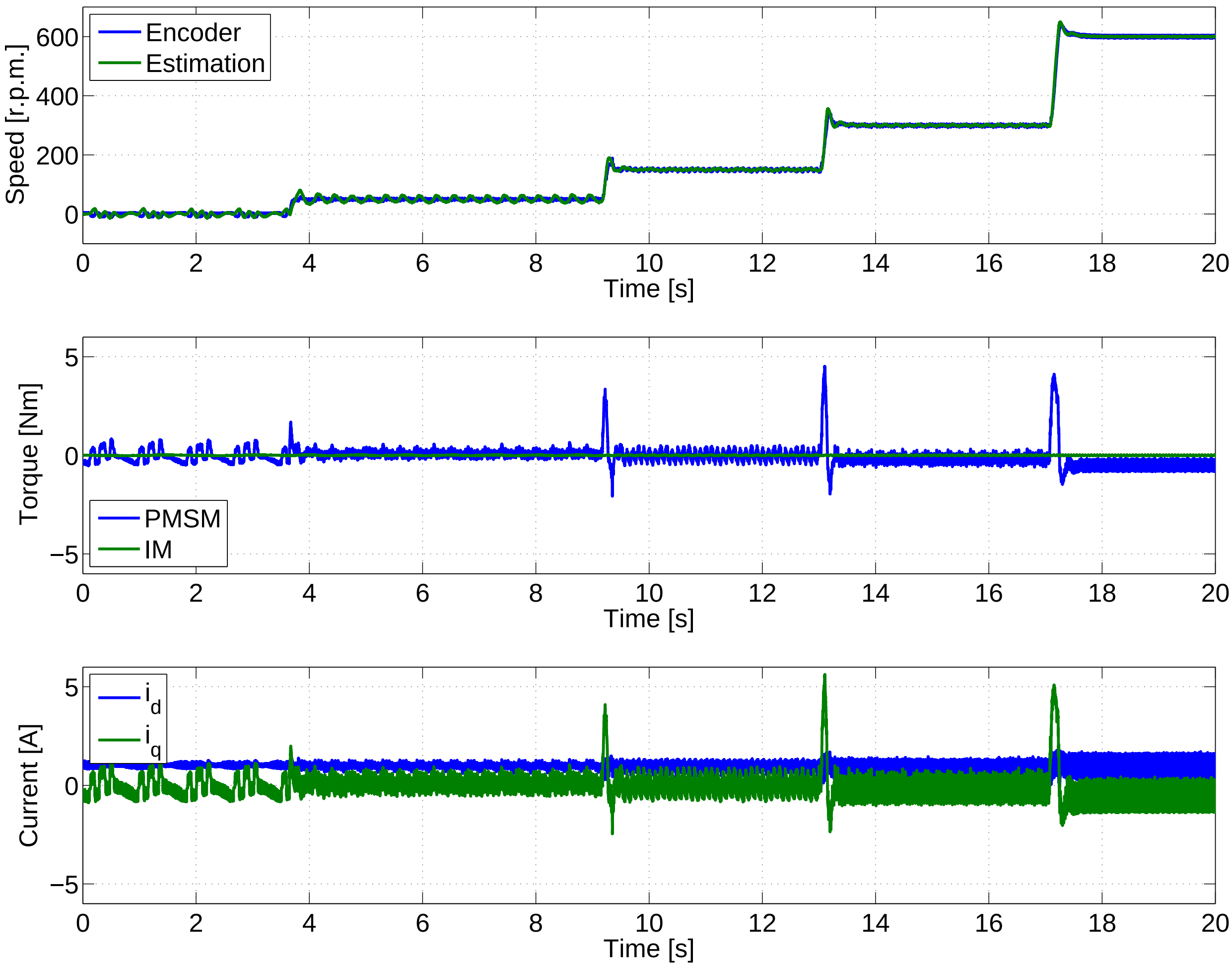

Figure 7.3: Experimental results for no load start and incrementing speed test

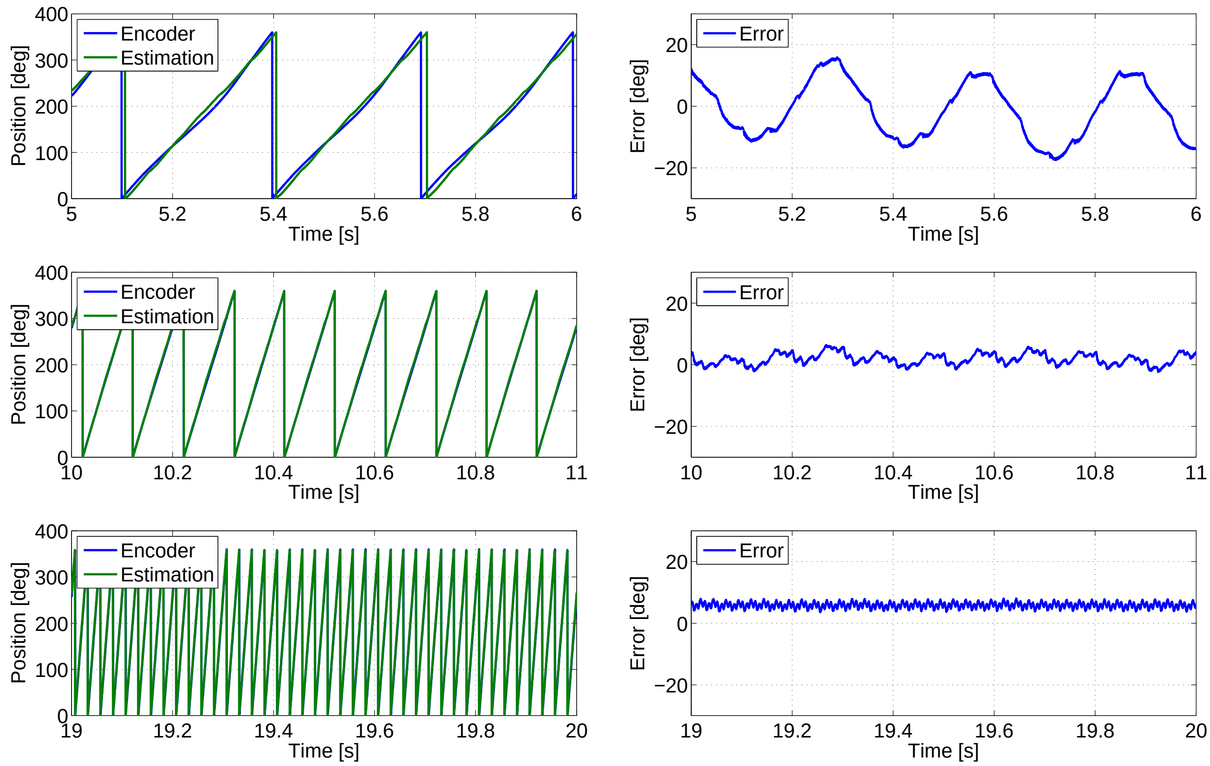

Figure 7.4: Position estimation and measurement comparison with relative error for several increasing speeds

In the graphs in Fig. 7.4, it can be seen how the position error oscillates less as the speed increases and how the steady state error remains constant with a value, based on the previously made considerations on parameters uncertainties.

7.2.2 Decresing Speed and Speed reversal

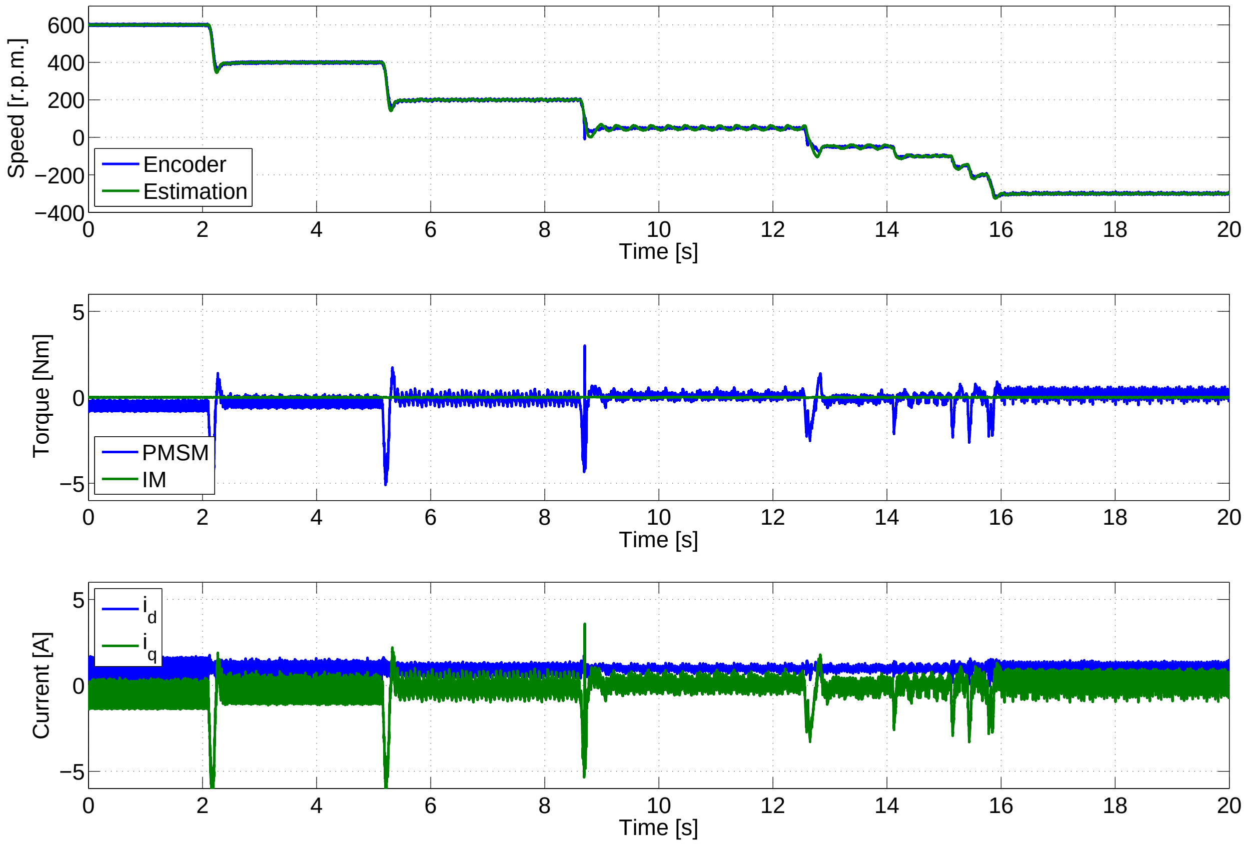

Figure 7.5: Experimental results for no load decrementing steps and speed reversal test

In the graphs in Fig. 7.5, it can be seen how the machine is decelerated from the starting speed of 600 rpm through several steps of different amplitude. As in the previous test, a good response in both steady and dynamic states is noticeable. The i_{d} current follows the reference given, while, on the other hand i_{q} differs from zero during mechanical transients. When there are changes in speed due to inertia, peaks in the i_{q} values appear.

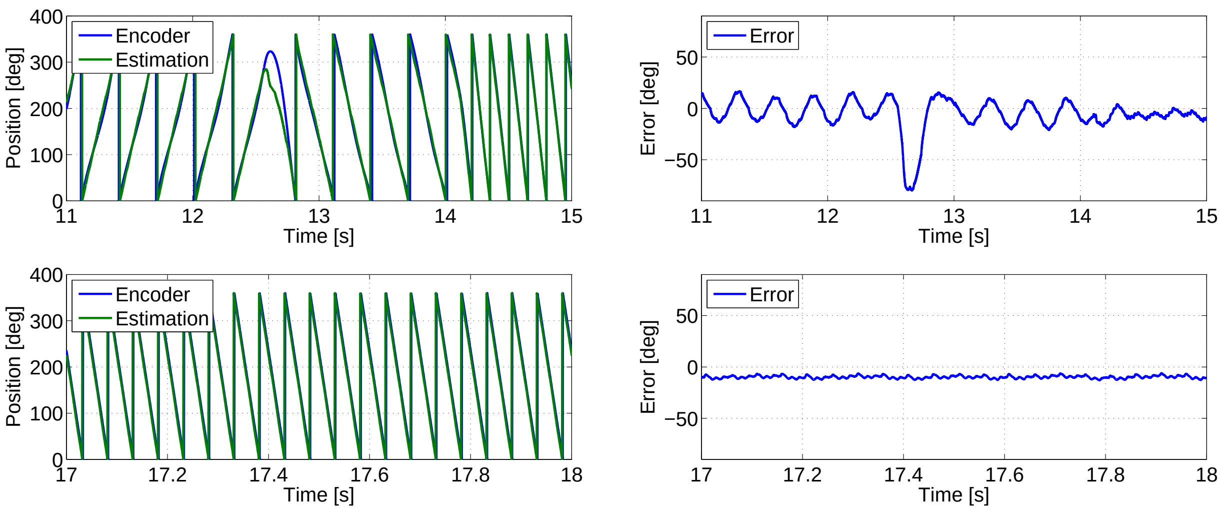

Figure 7.6: Position estimation and measurement comparison with relative error during speed reversal and for negative speed

In the graphs in Fig. 7.6, it can be seen how the position error diverges during the speed reversal but the globally stable algorithm is able to track the change and bring the error back to fluctuate around 0. As in the previous case the steady state error is a constant value depending on parameters inaccuracies.

7.3 Test with load

In these tests, the sensorless algorithm is tested with some load. In the first test the machine is run at the constant speed of 800 rpm while the load torque is brought to half the rated one through steps of $2Nm$. In the second test the machine is stepped in the mid speed range from 400 rpm up to 1200 rpm, and then back to 400 rpm while half rated torque load is applied. The tests show the performances during transients and steady state of the algorithm in terms of position error. Unfortunately since it was not possible to implement successfully the online estimation strategy for the parameters, it is not possible to prove experimentally that a correction of parameters uncertainties would affect positively the position error

7.3.1 Test with constant speed

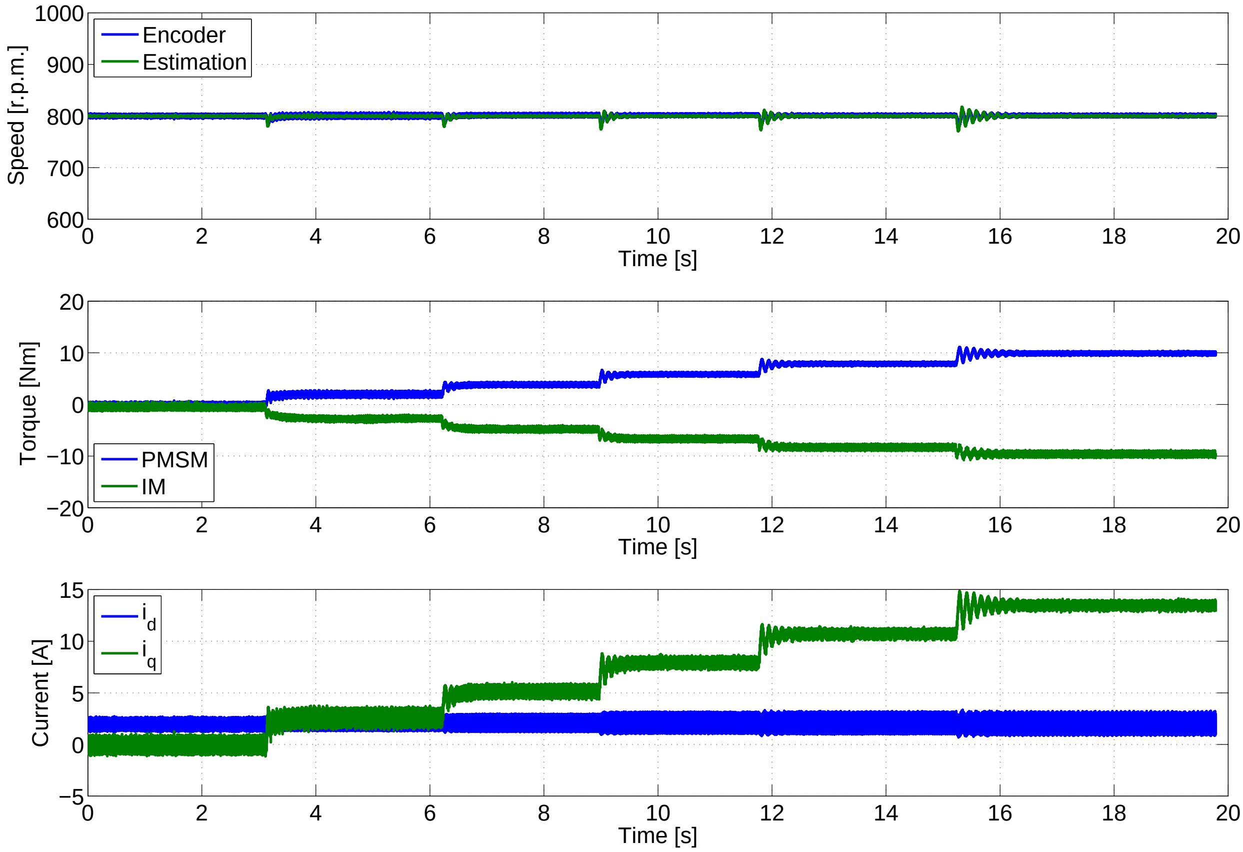

Figure 7.7: Experimental results for constant speed test with stepping load

The graphs in Fig. 7.7 show that the speed control is able to compensate for the torque step disturbance. From the diagram of angle comparison and position error in Fig. 7.8 it is possible to see that as the load increases, also the position error increases. As it was shown in chap. 5, the parameters uncertainties affect the position error also through the torque generating current.

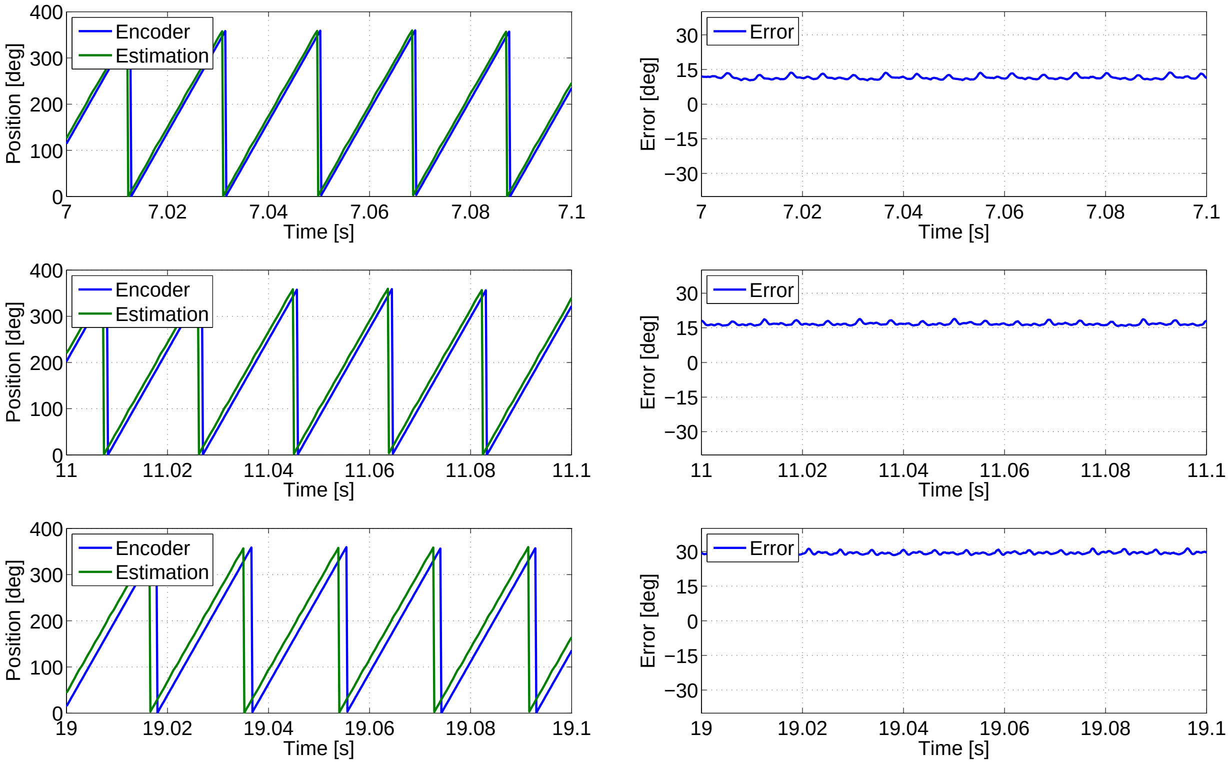

Figure 7.8: Position estimation and measurement comparison with relative error during constant load test

7.3.2 Test with constant load torque

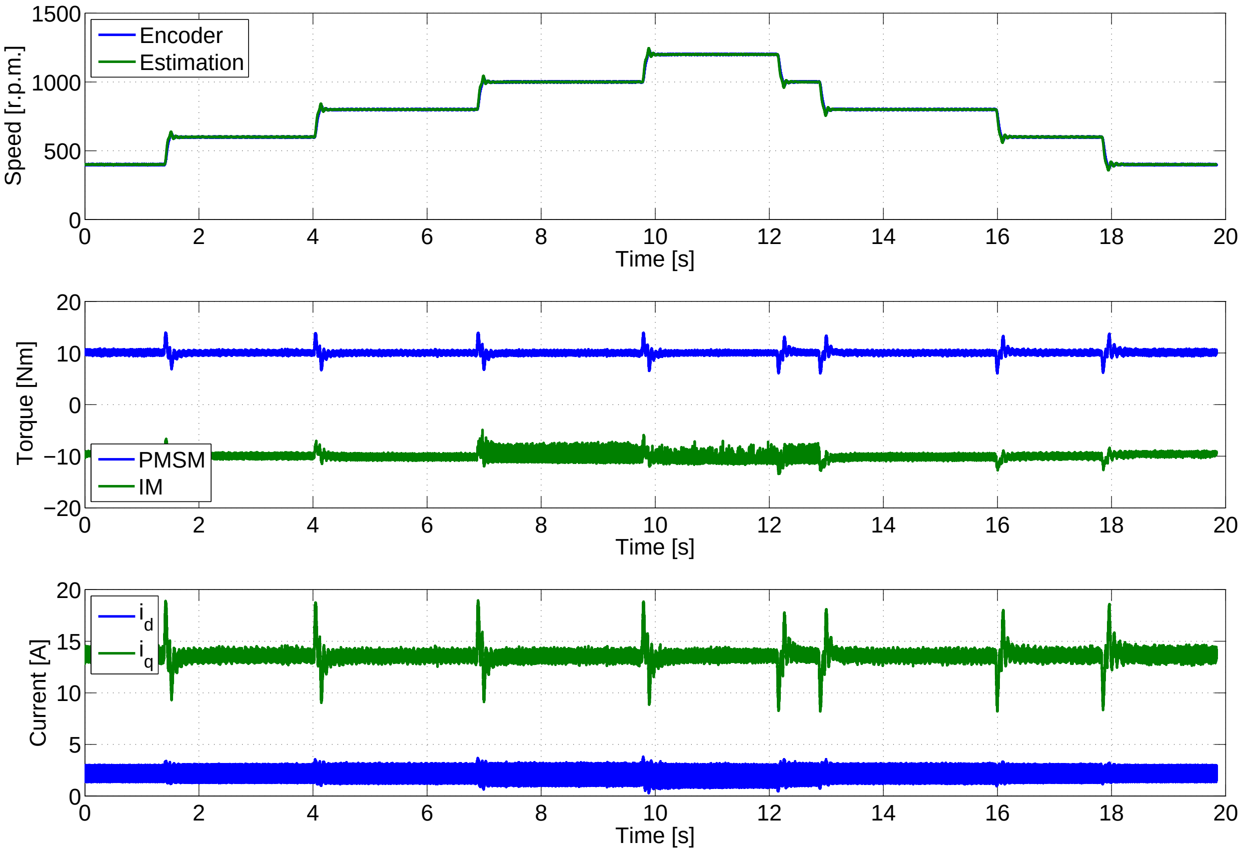

Figure 7.9: Experimental results for constant load test

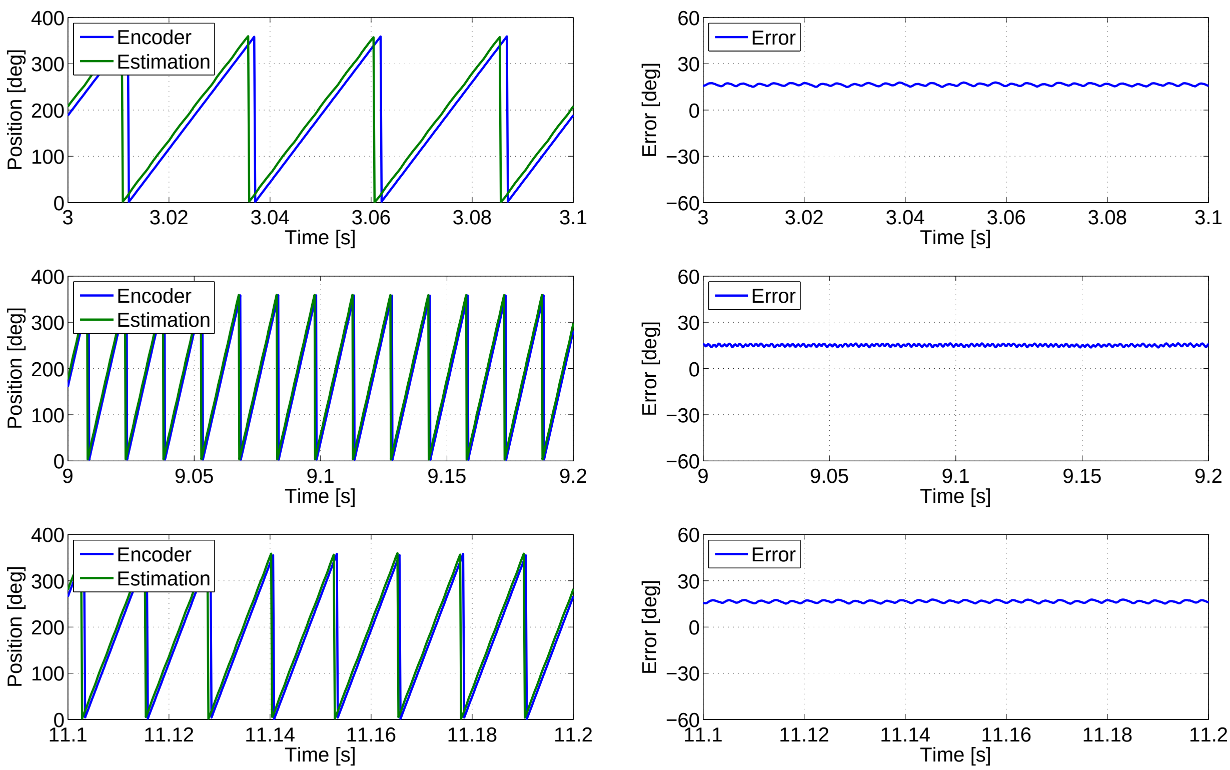

Figure 7.10: Position estimation and measurement comparison with relative error during constant load test

The last tests confirms what seen in the previous ones. The speed control is able to follow the speed reference, compensating for the constant load torque disturbance. The steady state position error is constant throughout the whole test since it depends mainly on the load current which remains constant.

Conclusion & Future Work 8

8.1 Conclusion

The thesis starts with a description of the concept of sensorless control for AC machines and its applications. The discussion is restricted to Permanent Magnet Synchronous Machines (PMSMs) and continues with a classification of the different classes of sensorless control methods with a brief overview of each class's proprieties. Through a literature review the most common issues with each class are outlined together with proposed solutions. It is decided to study the effects of parameter uncertainties and the possibilities of using an online parameter estimation tool for the methods which use model based observation of back-EMF components for estimating rotor position.

After its definition the problem is tackled from a theoretical point of view. First the generic models for each component of a PMSM drive system are derived and outlined. The model of the PMSM in the rotor and in the stationary two-phase is derived through Park and Clarke transformations from the stationary three phase model. The Space Vector Modulation (SVM) strategy is outlined and chosen for controlling the Voltage Source Inverter (VSI) of the PMSM drive system.

The principle of Field Oriented Control for PMSM is then described together with practical and graphical representation of the concept of field orientation. The Field oriented control scheme used in this thesis is given and the design procedure is entirely carried out for the system used in the experiments. First the current control loops are designed, followed by the speed control loop. It is decided to carry out the control design for both control lops directly in discrete for a successive straightforward implementation. The design is done through root locus analysis in the z plane. The control loops include an anti wind-up protection in order to reduce oscillations in case of saturation of the control variables.

The principle of rotor position estimation from back-EMF components is outlined. The fundamental distinction from methods based on the stationary $\alpha\beta$ model and the ones based on a rotating reference frame model is given. It is chosen to study the methods based on rotating reference frame model. Therefore the model of a PMSM in a rotating estimated reference frame, the $\delta\gamma$ reference frame, is derived from the $\alpha\beta$ model through Park transformation, by expressing the rotor position angle as function of the position error. The effects of machine saliency on the complexity of the model are stressed. The second Matsui method is then introduced and described. Its closed loop convergence is studied analytically and numerically through the indirect Lyapunov method, so that stability criteria can be derived for the estimator parameters. Four equilibria are found and the convergences/stability of these are studied through phase plane analysis. The extension to the method proposed by Nahid-Mobarakeh, a variable structure estimation law which makes it globally convergent, is introduced. The performances of the sensorless control algorithm are first evaluated through simulations which confirm the analytical results.

The effects of parameter uncertainties are analysed and a Model Reference Adaptive System (MRAS) online estimation tool for the stator resistance is introduced and evaluated through simulations.

In order to improve the experimental performances, a strategy for compensating the voltage drops in the VSI due to the dead time and devices' forward voltages is introduced and implemented on the experimental platform. Finally the performances of the sensorless control method are evaluated experimentally on a SPMSM drive system. The experimental results confirm the analytical and numerical results for what concerns the convergence criteria and effects of parameters uncertainties resulting in a position error in steady state. It is showed that the position error increases as the machine is pulling more load, this can be explained with the effects of parameters uncertainties which depend on the torque current. Unfortunately it was not possible to fully implement the online estimation tool which was the strategy intended to reduce the error.

8.2 Future Works

Troubleshooting the practical implementation of the online estimation tool should be the first step for any further work on the project. It is important in order to evaluate if the online estimation strategy is valid for practical application. In addition other strategies for reducing the position error during operation with load should be considered. Solutions using a Phase Locked Loop (PLL) are possible improvement for the used sensorless method as proposed in [Eskola, 2006], together with solution which do not use static gains for the estimator but dynamic ones for improving the transient response. In this sense the relationships between the estimator performances and the bandwidth of the speed controller should be studied.

Appendices

Digital Filter design A

As pointed out in chap. 4, in any practical application a Low Pass digital filter for the estimated speed feedback is necessary in order to reduce the effects of system's noise on the speed controller.

The Low Pass filter is obtained through the discretization of a generic first order continuous low pass filter. The filter transfer function is discretized through backward Euler approximation of the differential operator.

The continuous Low Pass filter transfer function is given in Eq. A.1

$$H(s) = \frac{y(s)}{u(s)} = \frac{1}{\tau s + 1} \tag{A.1}$$

τ is the filter time constant. The differential equation is yielded from the transfer function

$$y(s)\tau s + y(s) = u(s) \tag{A.2}$$

The Laplace operator s is considered as a differential operator, which is approximated through the backward Euler method as shown in Eq. A.3.

$$s = \frac{z-1}{T_{\mathrm{s}} z} \tag{A.3}$$

T_{s} is the discrete sampling time which is related to the filter cut-off frequency by $\tau = \frac{1}{2\pi f_{-3db}}$. This yields the expression for the filter in the z-domain and in the discrete form in time domain.

$$y(z)\tau\frac{z-1}{T_{\mathrm{s}} z} + y(z) = u(z) \tag{A.4}$$

$$y(z)\tau z - y(z)\tau + y(z)T_{\mathrm{s}} z = u(z)T_{\mathrm{s}} z \tag{A.5}$$

$$y(z)z = y(z)\frac{\tau}{\tau + T_{\mathrm{s}}} + u(z)z\frac{T_{\mathrm{s}}}{\tau + T_{\mathrm{s}}} \tag{A.6}$$

$$\Downarrow \quad \mathcal{Z}^{-1}$$

$$y(k+1) = y(k)\frac{\tau}{\tau + T_{\mathrm{s}}} + u(k+1)\frac{T_{\mathrm{s}}}{\tau + T_{\mathrm{s}}} \tag{A.7}$$

Eq. A.7 is normally written as in Eq. A.8 so that the bandwidth of the digital filter is normalized to the sampling time.

$$y(k+1) = y(k)(1-a) + u(k+1)a \tag{A.8}$$

$$a = \frac{T_\mathrm{s}}{\tau + T_\mathrm{s}} \tag{A.9}$$

The filter cutoff frequency is chosen to be 15 Hz which corresponds to a time constant of about 10 ms.

Stability Analysis for Second Matsui method speed estimator B

The stability of the 4 linear subsystems (Eq. 4.36-4.39) is analysed.

$x_{\mathbf{e1}}$ subsystem

The characteristic polynomial of the state matrix is calculated.

$$\det\left(\lambda I - \left(\frac{\partial f(x)}{\partial x}\right)_{x=x_{\mathrm{e1}}}\right) = \lambda\left(\lambda + \frac{p}{J}T_{\mathrm{L0}}\right) + \frac{3}{2}\frac{p^2}{J}\psi_{\mathrm{pm}} i_\gamma(\beta\psi_{\mathrm{pm}} - 1) \tag{B.1}$$

The Routh-Hurwitz criterion for stability demands that all the coefficients are positive. Therefore $i_\gamma(\beta\psi_{\mathrm{pm}} - 1) > 0$. With the hypothesis of a positive load torque (i.e. $i_\gamma > 0$) and using the chosen estimator gain β as in Eq. 4.40, then the following stability condition applies.

$$(b\ \mathrm{sgn}(\hat{\omega_{\mathrm{r}}}) + 1) < 0 \tag{B.2}$$

$x_{\mathbf{e2}}$ subsystem

The characteristic polynomial of the state matrix is calculated.

$$\det\left(\lambda I - \left(\frac{\partial f(x)}{\partial x}\right)_{x=x_{\mathrm{e2}}}\right) = \lambda\left(\lambda + \frac{p}{J}T_{\mathrm{L0}}\right) + \frac{3}{2}\frac{p^2}{J}\psi_{\mathrm{pm}} i_\gamma(\beta\psi_{\mathrm{pm}} + 1) \tag{B.3}$$

The Routh-Hurwitz criterion for stability demands that all the coefficients are positive. Therefore $i_\gamma(\beta\psi_{\mathrm{pm}} + 1) > 0$. With the hypothesis of a positive load torque (i.e. $i_\gamma > 0$) and using the chosen estimator gain β as in Eq. 4.40, then the following stability condition applies.

$$(b\ \mathrm{sgn}(\hat{\omega_{\mathrm{r}}}) - 1) < 0 \tag{B.4}$$

$x_{\mathbf{e3}}$ subsystem

The characteristic polynomial of the state matrix is calculated.

$$\det\left(\lambda I - \left(\frac{\partial f(x)}{\partial x}\right)_{x=x_{\mathrm{e3}}}\right) = (\lambda - \beta\psi_{\mathrm{pm}}\omega_{\mathrm{r}}^\circ)\left(\lambda + \frac{p}{J}\frac{dT_{\mathrm{L}}(\omega_{\mathrm{r}}^\circ)}{d\omega_{\mathrm{r}}}\right) \tag{B.5}$$

$$= \lambda^2 + \lambda \left(\frac{p}{J} \frac{dT_{\mathrm{L}}(\omega_{\mathrm{r}}^{\circ})}{d\omega_{\mathrm{r}}} + b|\omega_{\mathrm{r}}^{\circ}| \right) + b|\omega_{\mathrm{r}}^{\circ}| \frac{p}{J} \frac{dT_{\mathrm{L}}(\omega_{\mathrm{r}}^{\circ})}{d\omega_{\mathrm{r}}} \tag{B.6}$$

The Routh-Hurwitz criterion for stability demands that all the coefficients are positive. With the hypothesis of a positive load torque derivative with respect to speed and using the chosen estimator gain β as in Eq. 4.40, then the following stability condition applies.

$$b > 0 \tag{B.7}$$

x_{e4} subsystem

The characteristic polynomial of the state matrix is calculated.

$$\det \left(\lambda I - \left(\frac{\partial f(x)}{\partial x} \right)_{x = x_{\mathrm{e4}}} \right) = \left(\lambda + \beta \psi_{\mathrm{pm}} \omega_{\mathrm{r}}^{+} \right) \left(\lambda + \frac{p}{J} \frac{dT_{\mathrm{L}}(\omega_{\mathrm{r}}^{+})}{d\omega_{\mathrm{r}}} \right) \tag{B.8}$$

$$= \lambda^2 + \lambda \left(\frac{p}{J} \frac{dT_{\mathrm{L}}(\omega_{\mathrm{r}}^{+})}{d\omega_{\mathrm{r}}} - b\, \omega_{\mathrm{r}}^{+} \cdot \mathrm{sgn}(\omega_{\mathrm{r}}^{+} \cos \tilde{\theta_{\mathrm{e4}}}) \right) - b\, \omega_{\mathrm{r}}^{+} \cdot \mathrm{sgn}(\omega_{\mathrm{r}}^{+} \cos \tilde{\theta_{\mathrm{e4}}}) \frac{p}{J} \frac{dT_{\mathrm{L}}(\omega_{\mathrm{r}}^{+})}{d\omega_{\mathrm{r}}} \tag{B.9}$$

$$= \lambda^2 + \lambda \left(\frac{p}{J} \frac{dT_{\mathrm{L}}(\omega_{\mathrm{r}}^{+})}{d\omega_{\mathrm{r}}} - b\, |\omega_{\mathrm{r}}^{+}| \cdot \mathrm{sgn}(\cos \tilde{\theta_{\mathrm{e4}}}) \right) - b\, |\omega_{\mathrm{r}}^{+}| \cdot \mathrm{sgn}(\cos \tilde{\theta_{\mathrm{e4}}}) \frac{p}{J} \frac{dT_{\mathrm{L}}(\omega_{\mathrm{r}}^{+})}{d\omega_{\mathrm{r}}} \tag{B.10}$$

The Routh-Hurwitz criterion for stability demands that all the coefficients are positive. With the hypothesis of a positive load torque derivative with respect to speed and using the chosen estimator gain β as in Eq. 4.40, then the following stability condition applies.

$$b \cdot \mathrm{sgn}(\cos 2 \arctan(-b)) < 0 \tag{B.11}$$

The sign of $b \cdot \mathrm{sgn}(\cos 2 \arctan(-b))$ is plotted for different values of b in Fig. B.1

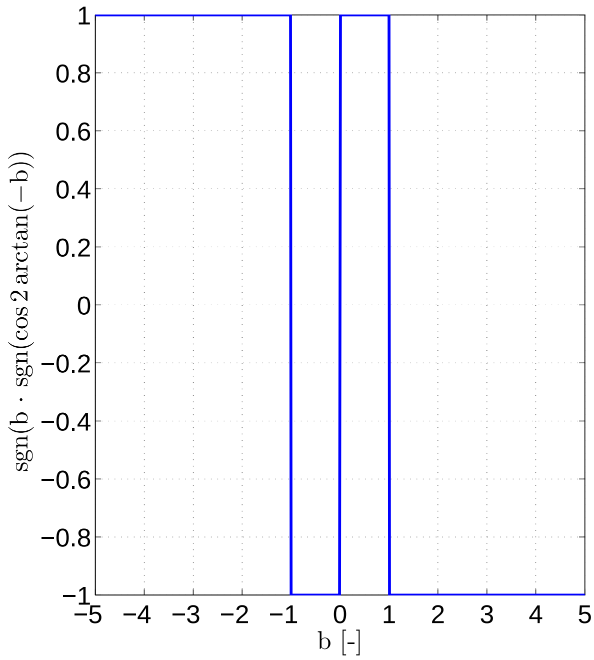

Figure B.1: Sign of $b \cdot \mathrm{sgn}(\cos 2 \arctan(-b))$

Fig. B.1 shows that the stability condition in Eq. B.11 is equivalent to the condition stated in Eq. B.12

$$-1 < b < 0 \vee b > 1 \tag{B.12}$$

Bibliography

AAU E.T. Department, 2014. AAU E.T. Department. *Flexible Drive Systems Laboratory*. `http://www.et.aau.dk/digitalAssets/83/83309_flexible_drive_systems_lab_aau.pdf`, 2014. Accessed 02-01-2016.

Abjadi, Soltani, Pahlavaninizhad, and Askari, 2005. N.R. Abjadi, J. Soltani, M. Pahlavaninizhad, and J. Askari. *A nonlinear adaptive controller for speed sensorless PMSM taking the iron loss resistance into account*. 1, 188–193 Vol. 1, 2005. doi: 10.1109/ICEMS.2005.202510.

Basar, Bech, Andersen, and Andersen, 2014. M.S. Basar, M.M. Bech, T.O. Andersen, and P.S. Andersen. *Self-commissioning of permanent magnet synchronous machine drives using hybrid approach*. pages 1–5, 2014. doi: 10.1049/cp.2014.0308.

Calligaro and Petrella, 2012. Sandro Calligaro and Robert Petrella. *Accuracy and robustness improvement in sensorless PMSM drives at low-speed by direct-axis current injection*. pages 1–5, 2012.

Eskola, 2006. Matti Eskola. *Speed and Position Sensorless Control of Permanent Magnet Synchronous Motor in Matrix Converter and Voltage Source Converter Applications*. 2006.

Glumineau and Leon Morales, 2015. A. Glumineau and J. de Leon Morales. *Sensorless AC Electric Motor Control: Robust Advanced Design Techniques and Applications*. Advances in Industrial Control. Springer International Publishing, 2015. ISBN 9783319145860.

Guangzhen, Feng, Yongxing, Xuhui, and Wei, 2013. Zhang Guangzhen, Zhao Feng, Wang Yongxing, Wen Xuhui, and Cong Wei. *Analysis and optimization of current regulator time delay in Permanent Magnet Synchronous Motor drive system*. pages 2286–2290, 2013. doi: 10.1109/ICEMS.2013.6713235.

Hinkkanen, Tuovinen, Harnefors, and Luomi, 2012. M. Hinkkanen, T. Tuovinen, Lennart Harnefors, and J. Luomi. *A Combined Position and Stator-Resistance Observer for Salient PMSM Drives: Design and Stability Analysis*. Power Electronics, IEEE Transactions on, 27(2), 601–609, 2012. ISSN 0885-8993. doi: 10.1109/TPEL.2011.2118232.

Inoue, Yamada, Morimoto, and Sanada, 2009. Y. Inoue, K. Yamada, S. Morimoto, and M. Sanada. *Effectiveness of Voltage Error Compensation and Parameter Identification for Model-Based Sensorless Control of IPMSM*. IEEE Transactions on Industry Applications, 45(1), 213–221, 2009. ISSN 0093-9994. doi: 10.1109/TIA.2008.2009617.

Jansen and Lorenz, 1994. P.L. Jansen and R.D. Lorenz. *A physically insightful approach to the design and accuracy assessment of flux observers for field oriented induction machine drives*. Industry Applications, IEEE Transactions on, 30(1), 101–110, 1994. ISSN 0093-9994. doi: 10.1109/28.273627.

Krause, Wasynczuk, Sudhoff, and Pekarek, **2013**. P.C. Krause, O. Wasynczuk, S.D. Sudhoff, and S. Pekarek. *Analysis of Electric Machinery and Drive Systems.* IEEE Press Series on Power Engineering. Wiley, 2013. ISBN 9781118524329.

Krishnan, **2010**. Ramu Krishnan. *Permanent Magnet Synchronous and Brushless DC Motor Drives.* 2010. ISBN 0-8247-5384-4.

Lee and Ha, **2012**. Kwang-Woon Lee and Jung-Ik Ha. *Evaluation of back-EMF estimators for sensorless control of permanent magnet synchronous motors.* Journal of Power Electronics, 12(4), 604–614, 2012.

Matsui, **1996**. N. Matsui. *Sensorless PM brushless DC motor drives.* Industrial Electronics, IEEE Transactions on, 43(2), 300–308, 1996. ISSN 0278-0046. doi: 10.1109/41.491354.

Morimoto, Kawamoto, Sanada, and Takeda, **2002**. S. Morimoto, K. Kawamoto, M. Sanada, and Y. Takeda. *Sensorless control strategy for salient-pole PMSM based on extended EMF in rotating reference frame.* Industry Applications, IEEE Transactions on, 38(4), 1054–1061, 2002. ISSN 0093-9994. doi: 10.1109/TIA.2002.800777.

Nahid-Mobarakeh, Meibody-Tabar, and Sargos, **2004**. B. Nahid-Mobarakeh, F. Meibody-Tabar, and F.-M. Sargos. *Mechanical sensorless control of PMSM with online estimation of stator resistance.* Industry Applications, IEEE Transactions on, 40(2), 457–471, 2004. ISSN 0093-9994. doi: 10.1109/TIA.2004.824490.

Nahid-Mobarakeh, Meibody-Tabar, and Sargos, **2001**. B.N. Nahid-Mobarakeh, F. Meibody-Tabar, and F.M. Sargos. *Robustness study of a model-based technique for mechanical sensorless PMSM.* 2, 811–816 vol.2, 2001. ISSN 0275-9306. doi: 10.1109/PESC.2001.954219.

Sen, Namuduri, and Nandam, **1996**. P.C. Sen, C.S. Namuduri, and Pradeep K. Nandam. *Evolution of control techniques for industrial drives.* 2, 1996.

Slotine, Li, et al., **1991**. Jean-Jacques E Slotine, Weiping Li, et al. *Applied nonlinear control*, volume 199. Prentice-hall Englewood Cliffs, NJ, 1991.

Underwood, **2006**. Samuel Underwood. *Online Parameter Estimation and Adaptive Control of Permanent Magnet Synchronous Machines.* 2006.

Underwood and Husain, **2010**. Samuel J Underwood and Iqbal Husain. *Online parameter estimation and adaptive control of permanent-magnet synchronous machines.* Industrial Electronics, IEEE Transactions on, 57(7), 2435–2443, 2010.

University of Newcastle, **2014**. University of Newcastle. *Case study: Sensorless control of high efficiency drives for consumer appliances.* http://impact.ref.ac.uk/casestudies2/refservice.svc/GetCaseStudyPDF/21782, 2014. Accessed 19-11-2015.

Vas, **1998**. Peter Vas. *Sensorless vector and direct torque control.* Monographs in electrical and electronic engineering. Oxford Univ. Press, Oxford, 1998.

Wilamowski and Irwin, **2011**. B.M. Wilamowski and J.D. Irwin. *Power Electronics and Motor Drives.* Electrical engineering handbook series. CRC Press, 2011. ISBN 9781439802861.

Zakladu, 2005. Kierownik Zakladu. *Integral Anti-Windup for PI Controllers.* http://www.isep.pw.edu.pl/ZakladNapedu/lab-ane/anti-windup.pdf, 2005. Accessed 25-11-2015.